

University of Alberta

**Development of a Novel Lateral Force-sensing Microindentation
Technique for Determination of the Interfacial Bond Strength**

by

Hong Zhang



A thesis submitted to the Faculty of Graduate Studies and Research in partial
fulfillment of the requirements for the degree of Doctor of Philosophy

in

Materials Engineering

Department of Chemical and Materials Engineering

Edmonton, Alberta
Fall 2004



Library and
Archives Canada

Bibliothèque et
Archives Canada

Published Heritage
Branch

Direction du
Patrimoine de l'édition

395 Wellington Street
Ottawa ON K1A 0N4
Canada

395, rue Wellington
Ottawa ON K1A 0N4
Canada

Your file *Votre référence*
ISBN: 0-612-96045-5
Our file *Notre référence*
ISBN: 0-612-96045-5

The author has granted a non-exclusive license allowing the Library and Archives Canada to reproduce, loan, distribute or sell copies of this thesis in microform, paper or electronic formats.

L'auteur a accordé une licence non exclusive permettant à la Bibliothèque et Archives Canada de reproduire, prêter, distribuer ou vendre des copies de cette thèse sous la forme de microfiche/film, de reproduction sur papier ou sur format électronique.

The author retains ownership of the copyright in this thesis. Neither the thesis nor substantial extracts from it may be printed or otherwise reproduced without the author's permission.

L'auteur conserve la propriété du droit d'auteur qui protège cette thèse. Ni la thèse ni des extraits substantiels de celle-ci ne doivent être imprimés ou autrement reproduits sans son autorisation.

In compliance with the Canadian Privacy Act some supporting forms may have been removed from this thesis.

Conformément à la loi canadienne sur la protection de la vie privée, quelques formulaires secondaires ont été enlevés de cette thèse.

While these forms may be included in the document page count, their removal does not represent any loss of content from the thesis.

Bien que ces formulaires aient inclus dans la pagination, il n'y aura aucun contenu manquant.

Canada

Acknowledgements

I wish to express my deepest gratitude to my supervisor, Dr. Dongyang Li, for his valuable guidance, encouragement and patience throughout the course of this work.

I also would like to acknowledge the financial support provided by ASRA (Alberta Science and Research Associate) and NSERC (National Science and Engineering Council of Canada).

Table of Contents

Chapter 1 Introduction and literature review

1.1. General	2
1.2. Types of interfacial bond and failure mechanisms.....	4
1.2.1 Definition of the interfacial bond.....	4
1.2.2 Types of interfacial bond.....	5
1.2.3 Failure mechanisms of interfacial bonding.....	8
1.3 Methods used to determine interfacial bond strength for coatings and thin films.....	9
1.3.1 Methods for determining the interfacial bond strength based on global failure.....	9
1.3.1 Methods to determine the interfacial bond strength based on local failure.....	16
1.4. Methods used to determine the interfacial bond strength for composites.....	20
1.4.1 Techniques used for bulk laminar composites.....	21
1.4.2. Technique used for fiber-matrix interfaces.....	25
1.5 Microindentation test.....	30
1.6 Statement of problems and objective of the research.....	35

Chapter 2 Development of a novel lateral force-sensing microindentation technique

2.1. Experimental procedure.....	38
----------------------------------	----

2.2 Examination of currently existing microindentation methods.....	40
2.3 The lateral force-sensing indentation method.....	43
2.4 Further justification by computer modeling.....	49
2.5 Interfacial stress analysis and determination of the interfacial bond strength.....	55
2.5.1 Finite element analysis.....	55
2.5.2 Interface failure criterion and interfacial bond strength.....	57
2.6. Comparison with a tension test.....	62
2.7 Conclusions.....	64

Chapter 3 A finite element study of interfacial failure mechanism and parametric influence on the lateral force-sensing indentation method

3.1 Construction of the simulation model.....	67
3.1.1 Finite element modeling.....	67
3.1.2 Interfacial failure criterion.....	69
3.1.3 Interfacial crack growth.....	70
3.1.4 Verification of the finite element model.....	71
3.2 Results and discussion.....	73
3.2.1 Deformation geometry and stress distribution for homogeneous materials.....	73
3.2.2 Deformation near an interface under indentation condition.....	78
3.2.3 Stress distribution at interface.....	81
3.2.4 Interfacial debonding.....	85

3.2.4.1 Interfacial debonding mechanism.....	85
3.2.4.2 The sensitivity of lateral force response to interfacial debonding.....	88
3.2 Conclusions.....	92

Chapter 4 Optimization of the indentation condition for determination of interfacial bond strength: A FEM study

4.1 Statement of the problem and the FEM model.....	96
4.1.1 Factors that affect the interfacial stress.....	96
4.1.2 FEM model.....	97
4.2 Results and discussion.....	102
4.2.1 Influences of material properties on the interfacial singularity.....	102
4.2.2 Influences of indentation parameters on interfacial debonding.....	105
4.3 Conclusions.....	111

Chapter 5 Application of the lateral force-sensing microindentation method for evaluation of the bond strength of thermal-sprayed coatings –A case study

5.1 Experimental procedure.....	113
5.1.1 Preparation of the coated samples.....	113
5.1.2 Microindentation test.....	115
5.2 Results and discussion.....	116
5.2.1 Microstructures of coatings.....	116

5.2.2 Determination of the interfacial bond strength.....	120
5.3 Comparison of results obtained using different methods	125
5.4 Conclusions.....	127
Chapter 6 Summary and future work	
6.1 Summary of the research results.....	129
6.2 Possible future studies.....	131
Publications.....	133
References.....	134

List of Tables

Table 1-1 Geometric parameters related to failure events under the critical loads.....	18
Table 3-1 Mechanical properties of materials.....	67
Table 4-1 Material properties.....	98
Table 4-2 Load and geometry parameters used for interfacial stress analysis.....	99
Table 5-1 Summary of plasma spray parameters.....	114
Table 5-2 Mechanical characteristics of involved materials.....	123
Table 5-3 Interfacial bond strength determined using the lateral-force Indentation method.....	125
Table 5-4 Pull-off test results.....	126

List of Figures

Fig. 1-1 Spallation of coatings/films from substrate.....	3
Fig. 1-2 Interfacial debonding in the composites.....	3
Fig. 1-3 Characteristics of a fiber/matrix interface in a composite material.....	4
Fig.1-4 Interfacial bonds.....	7
Fig. 1-5 Mechanisms responsible for interface failure.....	8
Fig. 1-6 Schematic representation of pull-off test.....	10
Fig. 1-7 Schematic representation of the four-point bending test.....	11
Fig. 1-8 Schematic illustration of a peel test.....	12
Fig. 1-9 Schematic illustration of ultracentrifugal arrangement for adhesion measurement.....	14
Fig. 1-10 Schematic representation of the cavitation test.....	16
Fig. 1-11 Schematic illustration of the scratch test.....	17
Fig. 1-12 Schematic illustration of different failure events occurring during scratching.....	17
Fig. 1-13 Schematic illustration of the impact test.....	19
Fig. 1-14 Schematic illustration of the laser spallation experiment.....	20
Fig. 1-15 Three-point short beam bending test for evaluation of interfacial strength for laminate composites.....	22
Fig. 1-16 The set-up of iosipescu shear test.....	23
Fig. 1-17 Schematic illustration of the $[\pm 45]_s$ tensile test.....	24
Fig. 1-18 Geometry of specimens for the single fiber compressive test.....	26
Fig. 1-19 Schematic illustration of the single-fiber fragmentation process.....	27

Fig. 1-20 Various fiber pull-out tests.....	29
Fig. 1-21 A typical stress versus displacement curve involving interfacial debonding.....	29
Fig. 1-22 Schematic cross-sections and force-displacement curves of various film/substrate interfaces.....	31
Fig. 1-23 Determination of interfacial debonding using the interfacial indentation test.....	32
Fig. 1-24 Interfacial debonding induced by Vickers indentation.....	33
Fig. 1-25 The push-out indentation test for evaluation of interfacial bond for fiber-reinforced composites.	34
Fig. 1-26 Evaluation of the interfacial bonding for a NiAl-matrix composite.....	35
Fig. 2-1 Schematic diagram of the indentation measurement.....	39
Fig. 2-2 Interfacial debonding caused by microindentation.....	41
Fig. 2-3 Typical loading and unloading curves of microindentation with interfacial cracking.....	42
Fig.2- 4 Acoustic emission response for indentation test near an interface.....	43
Fig. 2-5 Acoustic emission response for Indentation at interface.....	44
Fig. 2-6 Load-time and lateral force F_x -time curves of an Al_2O_3/Al alloy bond.....	45
Fig. 2-7 Debonding at an Al_2O_3/Al alloy interface caused by indentation.....	45
Fig. 2-8 Normal load-time and lateral force-time curve of $Al_2O_3/Steel$ 4045 bonds..	47
Fig. 2-9 Schematic illustration of an interfacial debonding process and corresponding changes in lateral force.....	48
Fig. 2-10 A system, used for modeling study (MSDM), is discretized and mapped onto discrete lattices.....	49

Fig. 2-11 Schematic illustration of a stress-strain curve.....	51
Fig. 2-12 Simulation of indentation near an interface and corresponding lateral displacement of the indenter as a function of time for a weak bond.....	53
Fig. 2-13 Simulation of indentation near an interface and corresponding lateral displacement of the indenter as a function of time for a medium bond.....	54
Fig. 2-14 Simulation of indentation near an interface and corresponding lateral displacement of the indenter as a function of time for a strong bond.....	55
Fig. 2-15 A system for indentation modeling using FEM.....	57
Fig. 2-16 Normal and shear stress distributions at an Al ₂ O ₃ /Al alloy interface under an indentation load.....	59
Fig. 2-17 A flow chart of the computational procedure used to determine the normal and shear strengths of an interface.....	61
Fig. 2-18 Schematic of a tension test for determination of the bond strength of an Al ₂ O ₃ / Al alloy interface.....	62
Fig.2-19 Comparison of experimental results of the tension test with a predicted bond strength obtained based on the force-sensing indentation test.....	63
Fig. 3-1 An illustrated stress~strain curve of an elastic-plastic material.....	68
Fig. 3-2 Illustration of (a) a system and (b) corresponding mesh for the FEM simulation.....	69
Fig. 3-3 A flow chart for modeling interfacial failure.....	71
Fig. 3-4 Comparison between numerical results of the FEM model and corresponding analytical solution.....	72
Fig. 3-5 Deformation geometries of different materials under an indenter tip.....	74

Fig. 3-6 Stress distribution caused by indentation in Cu material.....	76
Fig. 3-7 Stress distribution caused by indentation in the Al alloy.....	77
Fig. 3-8 Deformation of Cu near a Cu-Ceramic interface at different indentation positions.....	79
Fig. 3-9 Deformation of Al alloy near a Ceramic-Al alloy interface at different indentation positions.....	80
Fig. 3-10 Stress distributions at interface for Cu- Ceramic bond.....	82
Fig. 3-11 Stress distributions at interface for Al alloy-Ceramic bond.....	84
Fig. 3-12 Interfacial debonding processes.....	86
Fig. 3-13 Stress distribution along the interface for ceramic/Cu bond.....	88
Fig. 3-14 Effects of interface bond strength on the lateral force response to indentation.	89
Fig. 3-15 Effects of indentation position on the lateral force response to indentation.....	91
Fig. 4-1 The bilinear elastic-plastic behavior of materials used in the FEM analysis.....	98
Fig. 4-2 Tensile test.....	100
Fig. 4-3 Indentation test.....	101
Fig. 4-4 Interfacial stresses with respect to l/H for different interfacial bonds under applied tensile stress.....	104
Fig. 4-5 The influence of indenter geometry and indentation.....	107
Fig. 4-6 The influence of indenter geometry and indentation position.....	109
Fig. 4-7 The influence of indenter geometry and indentation.....	110
Fig. 5-1 Schematic illustration of the indentation test.....	115
Fig. 5-2 Cross-sectional SEM image of ceramic/metal interfacial regions in Al_2O_3/TiO_2 coatings on steel substrate.....	117

Fig. 5-3 A SEM image of the interface between a fully-melted (FM) region
and the steel substrate in the commercial coating Metco 130.....118

Fig. 5-4 A SEM images of two interfaces in the nanostructured coating.....119

Fig. 5-5 Schematic illustration of coating's microstructures.....119

Fig. 5-6 Typical changes in the normal load and lateral force change vs. time.....120

Fig. 5-7 Cracking at interface caused by indentation.....121

Fig. 5-8 The critical loads vs. indentation distance from interface for the coatings.....122

Chapter 1

Introduction and literature review

1.1. General

Interfaces exist in many engineering materials, such as coatings/films, composites and multiphase alloys. In order to improve surface properties of mechanical components, coatings/films are often used to improve surface performance, while reinforced fibers or second phases in composites are used to meet special requirements for bulk materials' mechanical properties. These materials are widely used in many industries, including mining, manufacturing, oil and gas, electronic and aerospace, etc.

The performance of coatings/films and composites in mechanical applications largely depends on their interfacial bond strength, due to the fact that interfaces are usually weaker than bulk phases and may result in failure of the entire system, even though the coatings/films or reinforced phases are sufficiently strong. As an example, Fig. 1-1 shows spallation of coatings from the substrate due to their weak interfacial bonds, which make the coatings useless. In composites, cracks may propagate along interface between the reinforced phase and the matrix, which causes the failure of stress transfer between the matrix and the reinforced phase (Fig. 1-2), thus resulting in a decrease in the material strength. In many cases, the interfacial bond is a limiting factor for effective application of protective coatings/films and composite materials.

Since the strength of an interfacial bond is of particular importance to coatings/films and composites, there is a demand for the development of effective techniques for quantitative assessment of interfacial bond strength. Considerable efforts have been made to develop methods for testing and characterizing various interfacial bonds. The main

methods currently used for evaluation of the interfacial bond strength are briefly reviewed in the following section.

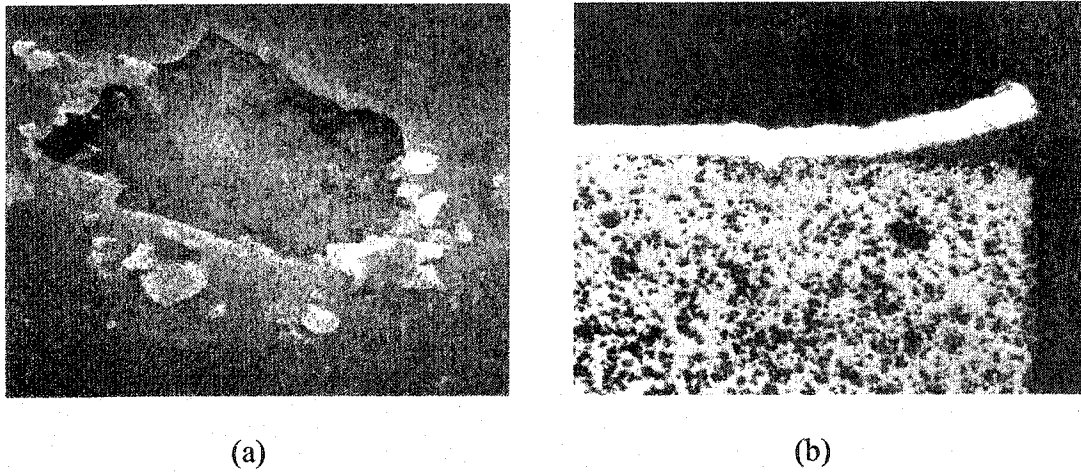


Fig. 1-1 Spallation of coatings/films from substrate ($\times 400$): (a) Ti film deposited on an Al_2O_3 substrate by physical vapor deposition [Ref.1], (b) A metal coating on a PZT ceramic [Ref. 2].

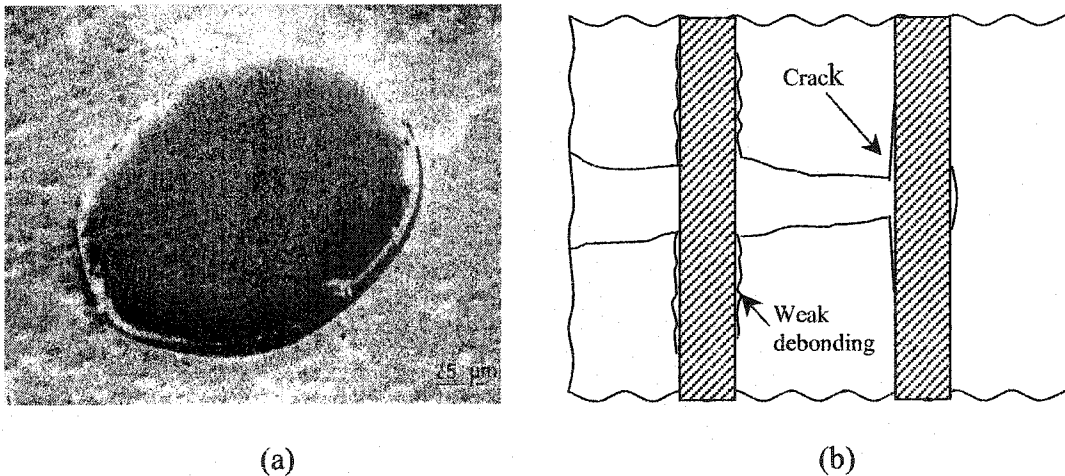


Fig. 1-2 Interfacial debonding in composites.(a) A fiber-reinforced composite [Ref. 3] and (b) schematic illustration of crack growth.

1.2. Types of interfacial bond and failure mechanisms

The interfacial bond strength is dependent on the bond type, which may involve mechanical, chemical and physical interactions. Consequently, the mechanisms responsible for interfacial failure of different types of interfacial bond could be different.

1.2.1. Definition of the interfacial bond

The term “interfacial bond” can be simply defined as the sticking together of two similar or dissimilar materials. However, the interfacial bond is rather complex, affected by many factors, including the fabrication condition, mechanical and chemical properties of the two phases that form the interface, the structures and compositions of the two phases, and the interfacial stress state. In addition, an interfacial bond may also be influenced by possible adsorbed materials, interfacial diffusion, and defects at the interface (See Fig. 1-3) [4].

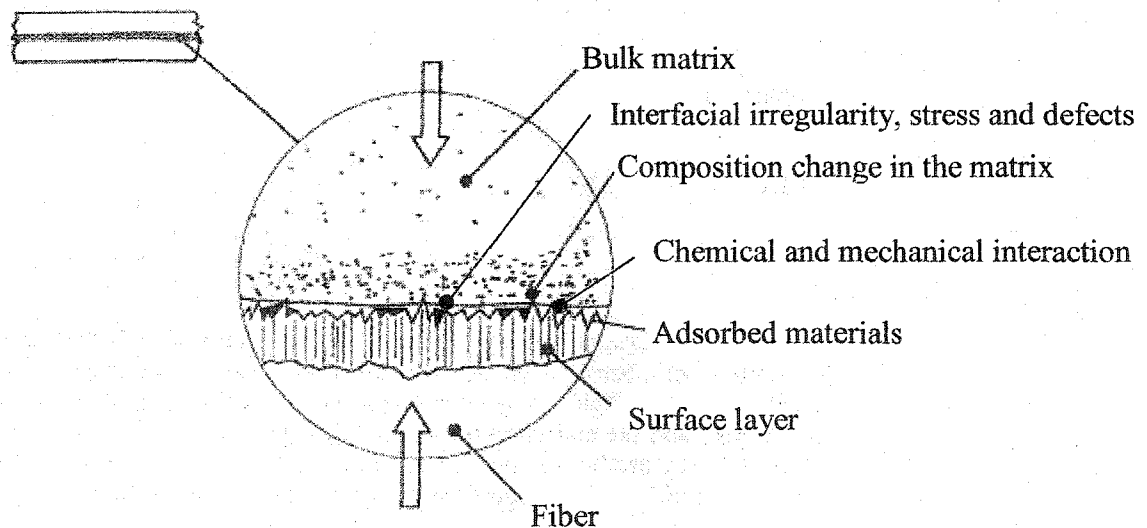


Fig. 1-3 Characteristics of a fiber/matrix interface in a composite material.

1.2.2. Types of interfacial bond

Interfacial bonds may form in different ways, depending on chemical compositions and structures of two adjacent phases, atomic arrangement, surface morphology and the diffusivity of elements in each phase. The interfacial bond may be formed to by electron interaction, chemical reaction and mechanical interlocking, etc. as shown in Fig. 1-4 [5~7]. The following factors may play roles in forming an interfacial bond:

---Interdiffusion

A bond between two surfaces may be formed by the interdiffusion of molecules or atoms across the interface as illustrated in Fig. 1-4(a). In this case, there must exist a thermodynamic equilibrium between the two constituents. The bond strength will depend on the amount of molecular entanglement, the number of molecules involved and the strength of the bond between the molecules. The formed interface region has a substantial thickness, and its chemical, physical and mechanical properties are different from those of the two adjacent phases.

---Electrostatic attraction

The difference in electrical charge between constituents at the interface may contribute to the attractive force between the two adjacent phases as in the case of acid-base interaction and ionic bonding (Fig. 1-4(b)). The strength of the interface depends on the charge density. This kind of attraction, however, can not make a major contribution to the final bond strength of the interface.

---Chemical bonding

The chemical bond is a main source for interfacial bonds. A bond is formed between two chemically compatible materials. The formation of the bond may result from usual thermally activated chemical reactions (Fig. 1-4 (c)).

----Interfacial reaction

In this case, reaction occurs to form new compounds in the interface region, especially those materials manufactured by a molten metal infiltration process. Reaction involves transfer of atoms from adjacent phases and reaction at the interface. Such compounds formed in the interface region are generally harmful to the overall mechanical behavior of the materials (Fig. 1-4(d)).

---Mechanical bond

Mechanical interlocking may also play a role when the interface is rough. The strength of this type of interface is unlikely to be high in tension unless there are a large number of re-entrant angles on the material surface, but the strength in shear could be high, depending on the degree of interfacial roughness. In addition, there may exist some internal stresses arising from the different shrinkage and thermal expansion coefficients of the materials that form the interface during material processing (Fig.1-4(e)).

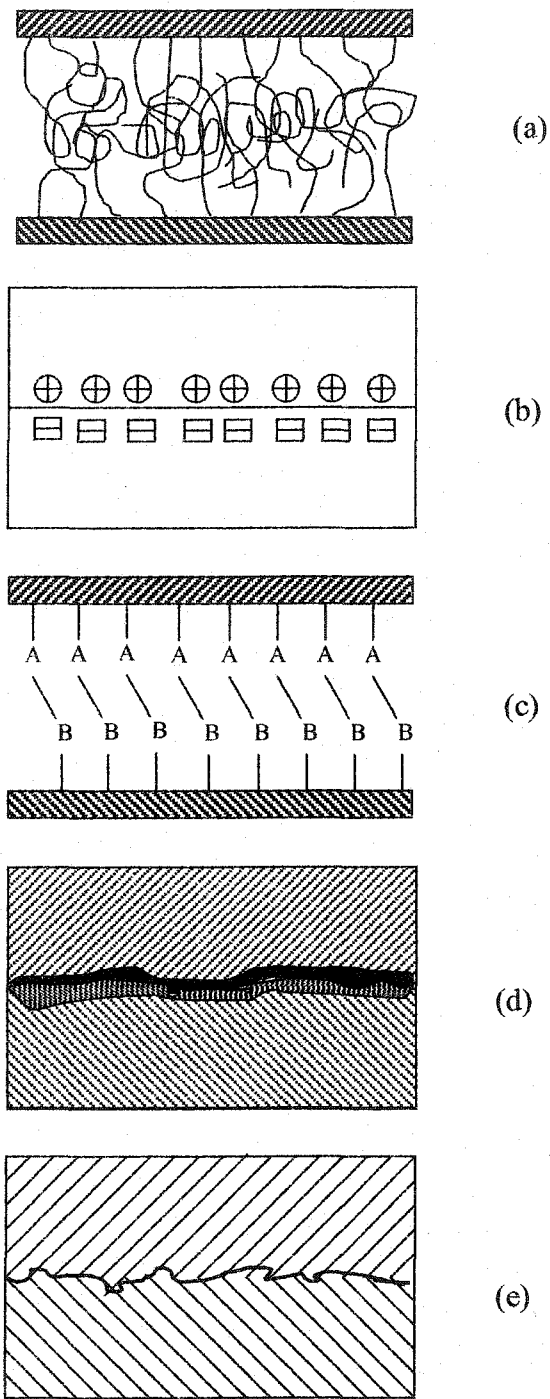


Fig.1-4 Interfacial bonds. (a) Bond formed by molecular entanglement following interdiffusion; (b) Bond formed by electrostatic attraction; (c) Bond formed by chemical reaction; (d) Chemical bond following forming of a new compound; (e) Bond formed by mechanical interlocking.

1.2.3. Failure mechanisms of interfacial bonding

When the stress applied to an interface is sufficiently large, it can cause interfacial debonding. There are several basic mechanisms responsible for interfacial debonding, depending on material properties and interfacial bond type [8]. In some cases, interfacial debonding could occur by plastic void coalescence or brittle debonding at the interface in accordance with ductile fracture and brittle fracture mechanisms, respectively (Fig. 1-5) [9]. When interphases or reaction products exist at the interface, debonding often occurs within phases. Both brittle and ductile debonding mechanisms may be responsible for debonding at the interface plane [10,11]. The brittle debonding mechanism is usually responsible for interfacial failure when the bond plane contains either contaminants or segregated particles.

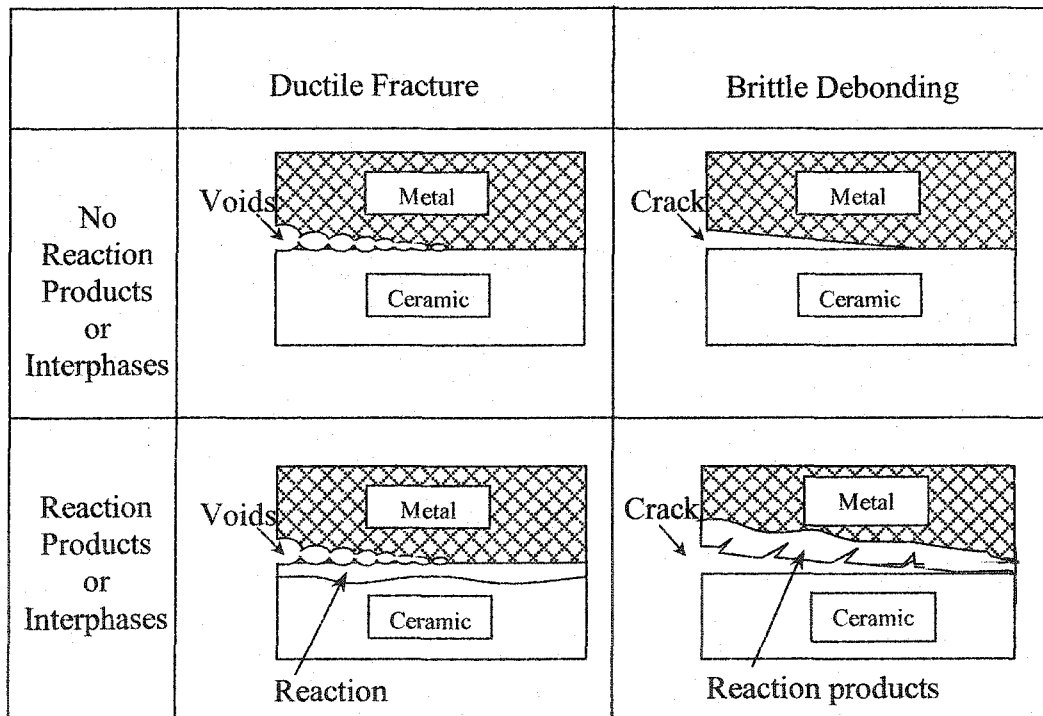


Fig. 1-5 Mechanisms responsible for interface failure.

1.3 Methods used to determine interfacial bond strength for coatings and thin films

The methods often used to determine the interfacial bond strength for coatings or thin films fall into two groups. One group includes the pull-off test, the bending test, the peel test and the cavitation test, which are based on global interfacial failure. The other group includes scratch test and impact test, which are based on local interfacial failure. Details of these methods are provided in the following sections.

1.3.1 Methods for determining the interfacial bond strength based on global failure

Pull-off test

In the pull-off test (tensile test)[12~15], a stud is glued directly to a coated sample, which is mounted in a self-aligning loading device as shown in Fig. 1-6. A tensile load is applied to the sample. The calculated bond strength represents the ultimate force divided by the contact area.

The pull-off test is a widely used method, which is simple and easy to operate. However, this method encounters the following difficulties: (a) it is difficult to apply pure tensile stress to a sample; a complex mixture of tensile and shear stresses may exist, which renders the interpretation of test results difficult, (b) the tensile tests are limited by the strengths of available adhesives or solders that bond the sample to the sample holder, (c) there is always the possibility that the stress is introduced during setting of the adhesive, or non-uniform stress distributions or stress concentrations exist over the contact area

during the pulling process. All of these factors affect the measurement of the interfacial bond strength.

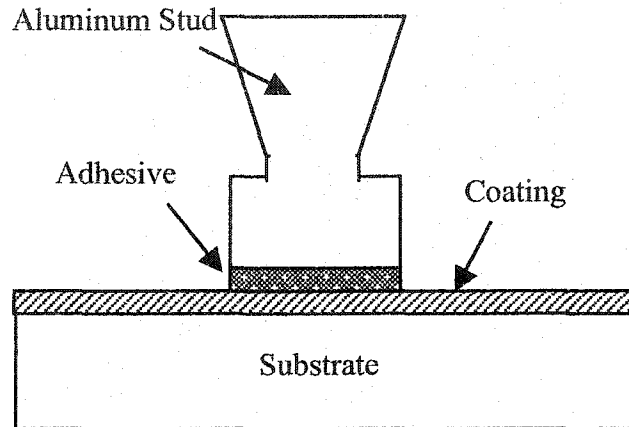
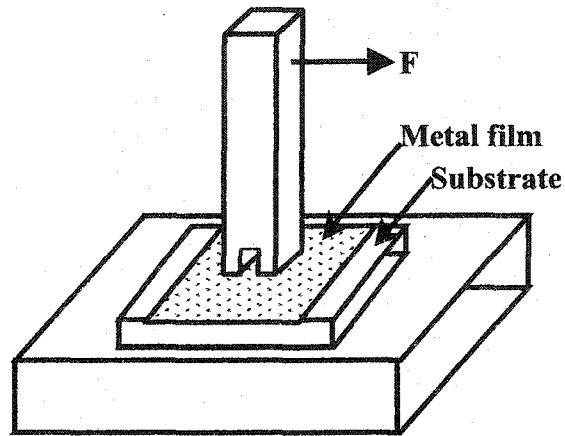


Fig. 1-6 Schematic representation of the pull-off test.

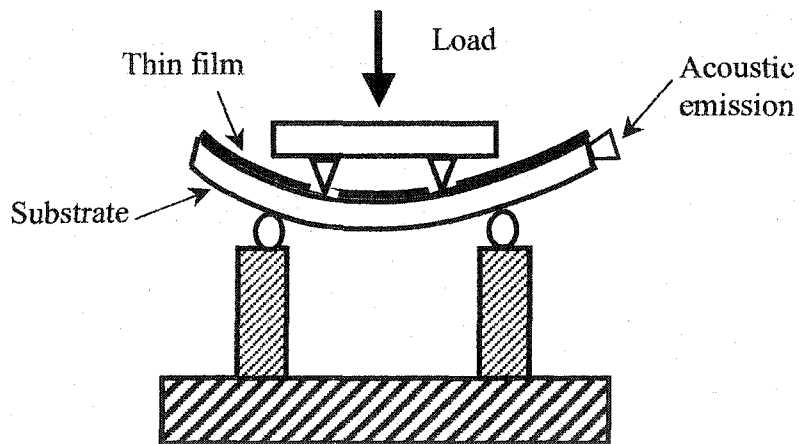
Bending test

There are two different ways to perform the bending test. One is to apply a load in a horizontal direction to a rod glued to a film (Fig. 1-7 (a)) and the moment of the force required to peel the film from the substrate is a measure of the interfacial bond strength [16~19]. This method has advantages over the direct pull-off method [20] because (a) this arrangement offers less substrate distortion since there would be no resultant overall force normal to the plane of the substrate and (b) this apparatus does not require such critical alignment as in the case of normal pull. The other way [21,22] is schematically shown in Fig. 1-7(b). A sample is fixed in the jig in such a way that the coating or film is loaded in compressive stress. The end of the sample is connected to an acoustic emission transducer to detect fracture during the bending test. The area in the vicinity of the loading stamps is not coated to avoid acoustic signals of fracture under the stamps, which

may mislead the measurement. The bending test is suitable for ductile coatings or films like polymers because the applied stress could generate cracks in hard and brittle coatings or films so that acoustic signals may not only represent the failure of an interface.



(a)



(b)

Fig. 1-7 Schematic representation of the four-point bending test.

Peel test

The peel test (peeling) applies a load to a coating or film to peel it off from the substrate, and the stripping strength can thus be determined as illustrated in Fig. 1-8 [23~26]. The film can be peeled off from the substrate in two ways: (a) by directly pulling the film, and (b) by applying a backing material to the film and then pulling the backing material, together with the film. The actual peel test is performed by peeling a film at a specified angle, e.g. 90° , the most common angle for peel test.

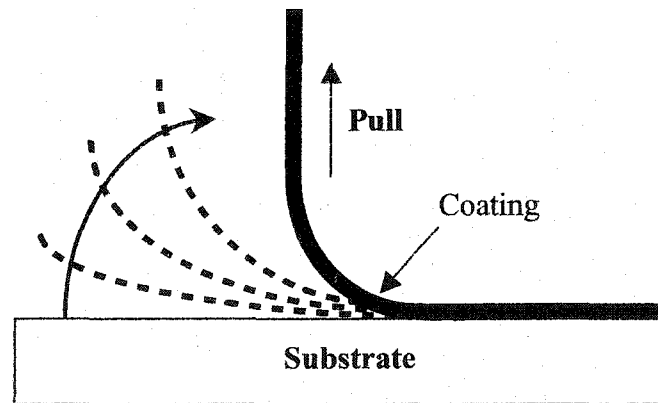


Fig. 1-8 Schematic illustration of a peel test.

This method is virtually impossible to specify the area involved at any instant, so that the pulling force has little significance. Results of peel test are usually expressed as energy or work done per unit area. Therefore, the results from peeling experiment are not directly comparable to the results obtained using other techniques that evaluate adhesion in terms of force per unit area. Furthermore, in order to make any useful measurement, the film

must be completely removed from the substrate, which limits the applicability of this technique to those interfaces which exhibit relatively weak adhesion. In addition, this method can be only used for flexible coatings.

Ultracentrifugal test

In the ultracentrifugal technique, adhesion is determined by measuring the force necessary to detach a film normal to the surface. As the name suggests, the specimen is in the form of a rotor, which is spun at extremely high speeds to provide the requisite centrifugal force as shown schematically in Figure 1-9. At a critical speed of rotation, the coating can no longer withstand the centrifugal stress and is detached [27~30]. In the ultracentrifugal system, the forces on the coating are given by:

$$T = \frac{Ar}{t} = \frac{4\pi^2 n^2 r^2 d}{g} \left(1 + \frac{t}{r} + \frac{t^2}{3r^2}\right) \quad (1.1)$$

where T is the hoop stress

A -- the adhesion in g/cm²

r -- the radius of the rotor in cm

n -- the number of revolutions per second

d -- the density of the coating in g/cm³

t -- the thickness of the coating in cm

g -- the acceleration due to gravity.

The adhesion strength can be determined based on the sample's dimensions and density as well as the rotation speed. However, this method can only deal with poorly adherent films. In addition, the values of adhesion obtained using this technique are lower than

those obtained using other methods. This could be explained if the film exhibits creep leading to a peeling phenomenon, where the load to start detaching the film could be far less than the normal force to tear it off [30]. Comments on this technique could be summarized [20]: (i) no adhesive or solder is required; (ii) the choice of the rotor material is important, as the measured adhesion values are dictated by the rotor material; (iii) for polymeric coatings, the viscoelastic behavior plays an important role; (iv) for very thin films, it may be difficult to obtain a requisite centrifugal force as the total force is the product of mass and acceleration; if mass is small, acceleration must be increased and this is limited by the rotor material, (v) if temperature of the rotor rises above the glass transition temperature of a polymeric film, the situation becomes quite complicated.

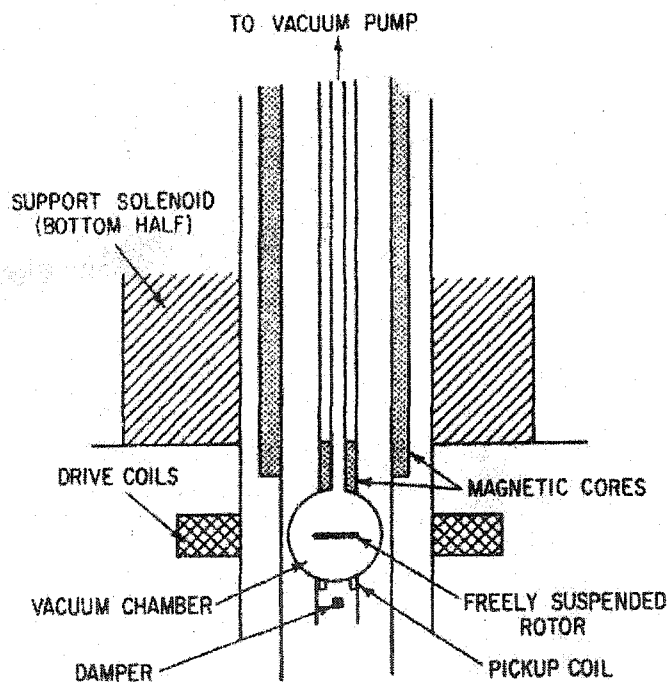


Fig. 1-9 Schematic illustration of ultracentrifugal arrangement for adhesion measurement [Ref. 20].

Cavitation test

The cavitation test is performed in a water tank in which the sample surface is exposed to high-power ultrasound as shown in Fig. 1-10 [31~34]. An ultrasonic transducer is placed above the sample. The high-power ultrasound generates blisters on the surface of the sample. After reaching a critical size, the blisters collapse, accompanied by the formation of a microscopic water jet that hits the surface with high pressure, generating a mechanical pulse. Since blisters are forming and collapsing continuously, a surface is under repeated impact at high frequency. As a result, a coating or film could be destroyed or detached from the substrate. The ratio of the damaged area to the total area is used to evaluate the interfacial adhesion.

This technique is usually used to evaluate relatively thick ($\geq 25\mu\text{m}$) paint films. Application of this method to thin films is rarely reported. Since the work required to detach metallic coatings is considerably larger than that for polymeric coatings, only less adherent metallic films may be amenable to this test. Obviously, values of adhesion strength determined using this method are influenced by the thickness and mechanical properties of the film [35-36].

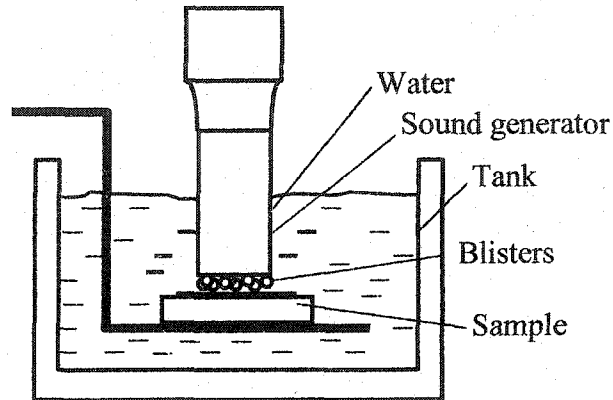


Fig. 1-10 Schematic representation of the cavitation test.

1.3.2 Methods to determine interfacial bond strength based on local failure

Scratch test

The scratch test is performed usually using a Rockwell-shaped diamond indenter to scratch a coated sample surface under a normal load [37~40]. Fig. 1-11 schematically illustrates the morphology of a scratch groove. Critical load for film detachment could be determined based on the crack pattern around the scratch as shown in Fig. 1-12 and geometric parameters listed in Table 1-1 [41]. The critical load may also be obtained from the Weibull statistical distribution of acoustic emission signals in a series of 20 scratch tests [41].

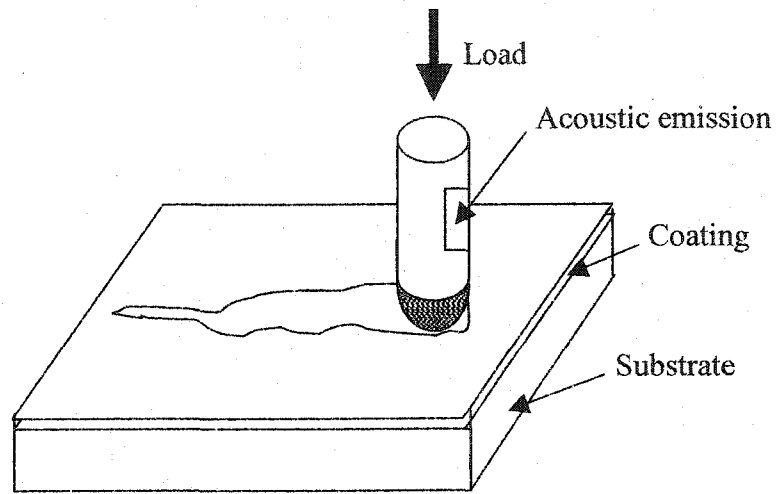


Fig. 1-11 Schematic illustration of the scratch test.

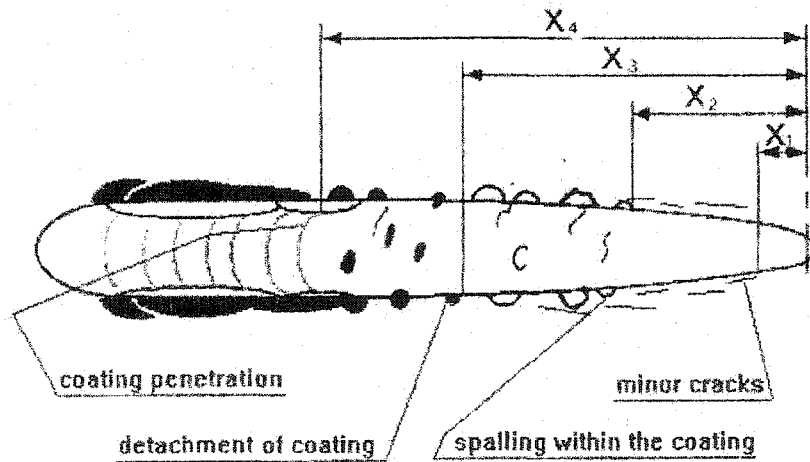


Fig. 1-12 Schematic illustration of different failure events occurring during scratching [Ref. 41].

Table 1-1 Geometric parameters related to failure events under the critical loads [Ref 41].

Distance from start	Description of failure event	Critical load
X_1	Longitudinal coating cracks at the scratch track edge	L_{c1}
X_2	Chipping at the scratch track edges, substrate not exposed	L_{c2}
X_3	Chipping at the scratch track edges, substrate exposed	L_{c2}
X_4	Ploughing of the indenter through the coating	L_{c3}

Studies [42] have demonstrated that the scratch test and resultant crack patterns are very complex and vary with the film material. This implies that it is difficult to obtain absolute values of adhesion using a general theoretical model. Comments on this method are summarized below:

- (1) The scratch pattern depends on elastic and plastic deformation of both the film and substrate, which is affected by their mechanical properties, primarily by their hardness.
- (2) There is no preferential failure at the film/substrate interface. Failure may occur in the film or in the substrate rather than at the interface.
- (3) Film detachment often occurs under lighter loads than required for track clearance. This depends on film tearing, film pile-up in front of the stylus, dust, imperfections, etc.

From the above comments, one may draw a conclusion that it is difficult to quantitatively evaluate the bond strength of an interface using the scratch method, since the critical load is not solely related to the interfacial bond strength.

Impact test

The impact test allows the determination of the local fatigue strength, which is related to the interfacial bond of a film/substrate interface [43~46]. A schematic illustration of the test apparatus is shown in Fig.1-13. A sample is cyclically loaded by a ball of cemented carbide, which is repetitively pushed on the sample surface. The surface damage of the sample is examined under an optical microscope. What is to be determined is the critical number of load cycles, N_c , at which the surface shows no further damage. This method only gives a qualitative estimation of the interface bond and is not often used in practice.

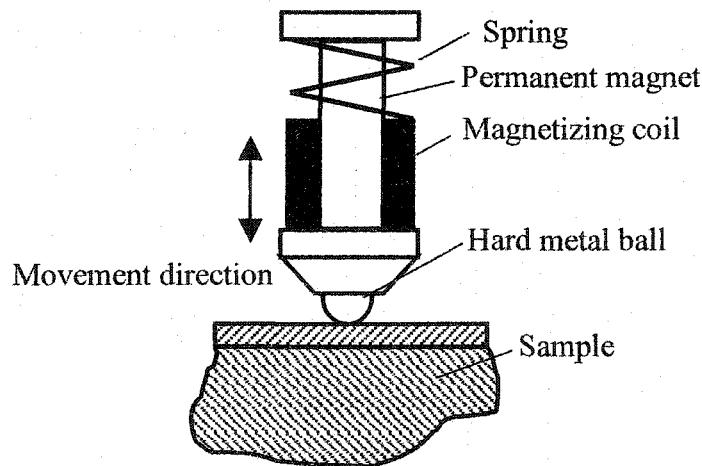


Fig. 1-13 Schematic illustration of the impact test.

Laser spallation test

The interfacial bond of a film could be evaluated using this technique. During the test, a laser pulse of high energy with a certain wave length is used to generate a pressure pulse,

which goes through the substrate towards the coated sample surface as shown in Fig. 1-14 [47-50]. The pressure wave then pries off the coating. The critical stress amplitude for the removal of the coating can be determined by computational simulation of the process. However, this method involves many parameters, such as the thickness of adsorptive layer, shape of the stress pulse, film properties and thickness. Therefore, this technique is not often used due to its complexity in practical application.

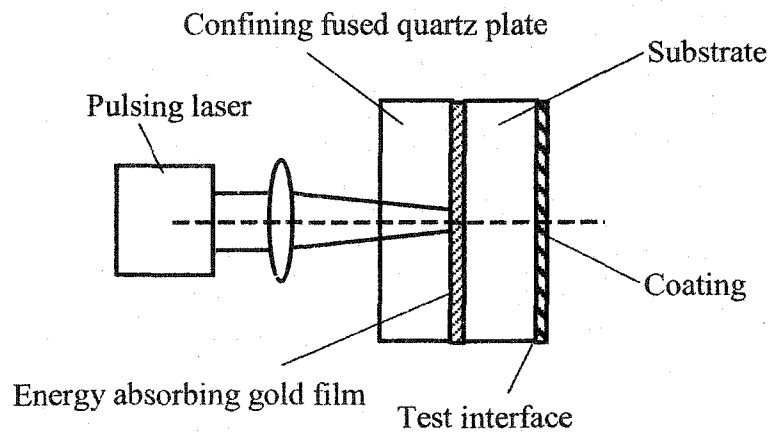


Fig. 1-14 Schematic illustration of the laser spallation experiment.

1.4. Methods used to determine the interfacial bond strength for composites.

The experimental methods used to characterize fiber/matrix interface are classified into two categories based on the scale of test: one employs bulk laminate composite to measure average interface properties on the macro level; the other involves evaluation of

interfacial properties of a single fiber embedded in a matrix block. These methods are described briefly in the following sections.

1.4.1 Techniques used for bulk laminar composites

Short beam shear test

The short beam shear test is designed to bend a beam of a unidirectional laminate composite as illustrated in Fig. 1-15 [51~54]. The generated interlaminar shear stress is parabolic within each layer, but a discontinuity in slope occurs at the ply interfaces. As a result, the maximum value of the shear stress does not necessarily occur at the center of the beam. The maximum shear stress can be determined using a classic short beam shear relationship [42]

$$\tau_{\max} = 0.75 \frac{P_{\max}}{bt} \quad (1.2)$$

where τ_{\max} is the maximum shear stress, which is related to the maximum applied load P_{\max} , and specimen width (b) and thickness (t). τ_{\max} is a measure of the interfacial bond strength.

This method is one of the most popular methods to determine the interlaminar bond strength of polymer-matrix and metal-matrix composites, since the test is easy to perform and samples are easy to make. However, the problem is the stress concentration and non-linear plastic deformation at the contact area of loading. The high stress concentration at the contact areas may cause premature local failure in the contact areas before interlaminar failure occurs. As a result, the failure signal may not always come from interfacial debonding [55].

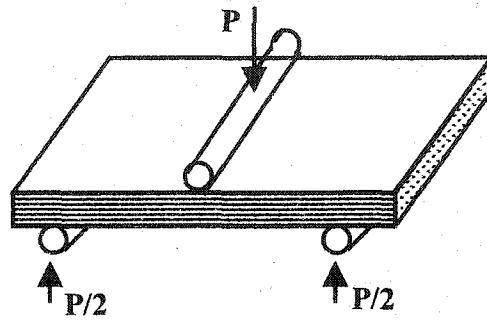


Fig. 1-15 Three-point short beam bending test for evaluation of interfacial strength for laminate composites.

Iosipescu shear test

The Iosipescu shear test [56-59] uses a double-edge-notched specimen that is subjected to two counteracting moments produced by force couples as shown in Fig. 1-16. A state of pure shear is achieved within the test section of the iosipescu shear test specimen and the interfacial shear strength can be determined. The shearing force acting at the centre of the cross-section is equal to the applied force measured from the loading device.

The shear stress τ is obtained by dividing the applied force P by the net cross-sectional area at the notches.

$$\tau = \frac{P}{br} \tag{1.3}$$

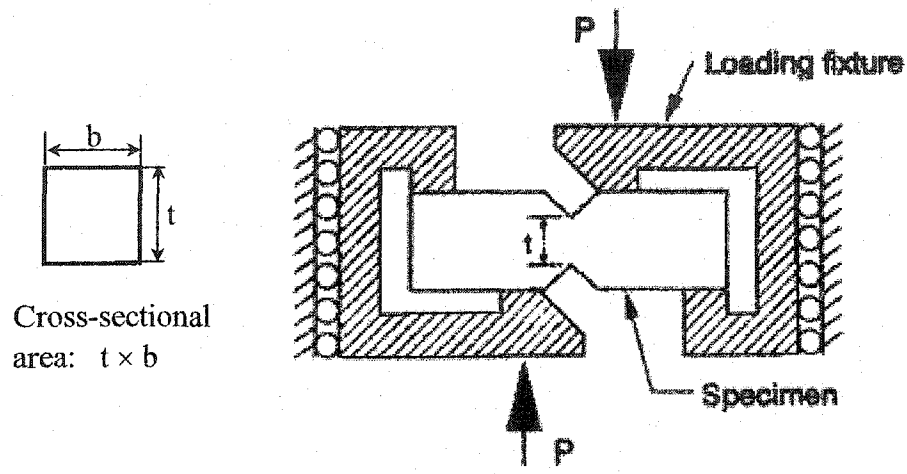


Fig. 1-16 The set-up of iosipescu shear test.

The main advantage of this test is that there is a large interfacial area under uniform shear stress, compared to the other shear tests. This method allows measuring both the in-plane shear strength and shear modulus in the direction parallel to the fiber with high accuracy and reproducibility. However, the pure shear is easily distorted by various factors, such as loading nose, twist and the bending moment arising from misalignment.

$[\pm 45]_s$ tensile test

In the $[\pm 45]_s$ tensile test [60-63], shown in Fig. 1-17, a uniaxial tensile stress is applied to a $(\pm 45^\circ)$ laminate composite sample and the normal strains in longitudinal and transverse directions, ϵ_x and ϵ_y are calculated based on the longitudinal load, P_x , or stress σ_x over the cross-sectional area ($b \times t$) of the specimen. Here, b is the width and t is the thickness of the specimen.

$$\tau_{12} = \frac{P_x}{2bt} = \frac{\sigma_x}{2} \quad (1.4)$$

$$\gamma_{12} = \varepsilon_x - \varepsilon_y \quad (1.5)$$

Therefore, the unidirectional translaminar shear strength can be calculated based on the maximum load and the in-plane shear modulus of elasticity.

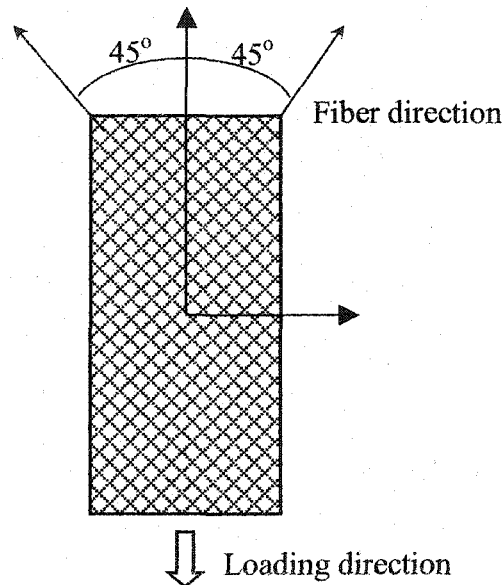


Fig. 1-17 Schematic illustration of the $[\pm 45]_s$ tensile test.

This technique is easy to apply using a conventional uniaxial tensile machine. However, such a test can not provide complete information on the interfacial bond strength, since the interfacial failure in the laminate composite does not result only from a shear stress, but is also affected by the normal stress on the interface.

1.4.2. Technique used for fiber-matrix interfaces

Single fiber compression test

For the single fiber compression test, two typical specimens with different geometries are used: one has a uniform tetragonal cross-section (Fig. 1-18(a)), the other has a curved neck in the middle (Fig.1-18(b) [64~67]. The fiber-matrix interface fails in different ways for these two types of specimen during the test. When a compressive load is applied to the specimen having a uniform cross-section along the fiber direction, owing to the difference in elastic property between the fiber and the matrix, shear stress is generated near the fiber ends. Further loading eventually results in interfacial cracking due to the interfacial shear stress concentration. However, the specimen having a curved neck under longitudinal compression has interfacial debonding in the transverse direction due to transverse expansion of the matrix when its Poisson ratio is greater than that of the fiber. The interfacial bond strength, therefore, could be determined in shear for the first type of specimen and in tension for the second type of specimens, respectively.

For the specimen having a uniform cross-section, the interfacial shear strength is determined by [68]:

$$\tau_b = 2.5\sigma_N \quad (1.6)$$

For the specimen having a uniform cross-section, the interfacial tensile strength is given by [68]:

$$\sigma_b = \frac{\sigma_N(v_m - v_f)}{(1 - v_m) + \alpha(1 - v_f - 2v_f^2)} \quad (1.7)$$

where σ_N is a critical compressive stress corresponding to interfacial debond. $\alpha = E_m/E_f$ is the ratio of Young's Modulus ratio of the matrix to that of the fiber; ν_m and ν_f are Poisson ratios of the fiber and matrix, respectively. The constant α in equation (1.6) is taken from an empirically shear stress concentration factor.

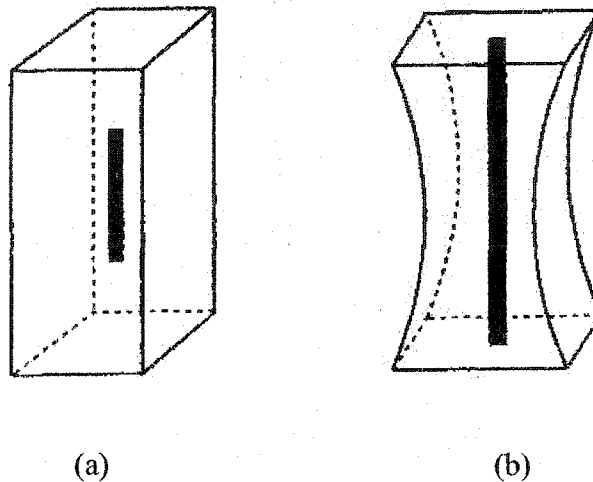


Fig. 1-18 Geometry of specimens for the single fiber compressive test. (a) a specimen having uniform cross-section and (b) a specimen with a curved neck.

The single fiber compression test is one of the earliest methods developed to measure the bond strength of glass fiber in a transparent polymer matrix. However, this method is not as popular as other methods because the matrix has to be transparent in order to observe interfacial debonding.

Fiber fragmentation test

The mechanism for the fiber fragmentation test [69~72] is illustrated by Fig.1-19. In such a test, a specimen containing a fiber is subjected to a uniaxial tensile stress, which

breaks the embedded fiber into smaller segments when the stress exceeds the tensile strength of the fiber. The load is continuously increased until lengths of all broken fiber are too short to allow further fiber breakage. The average fiber fragment lengths is referred as the “critical transfer length (L_c), which is the minimum fiber length that allows effective stress transfer across the fiber/matrix interface.

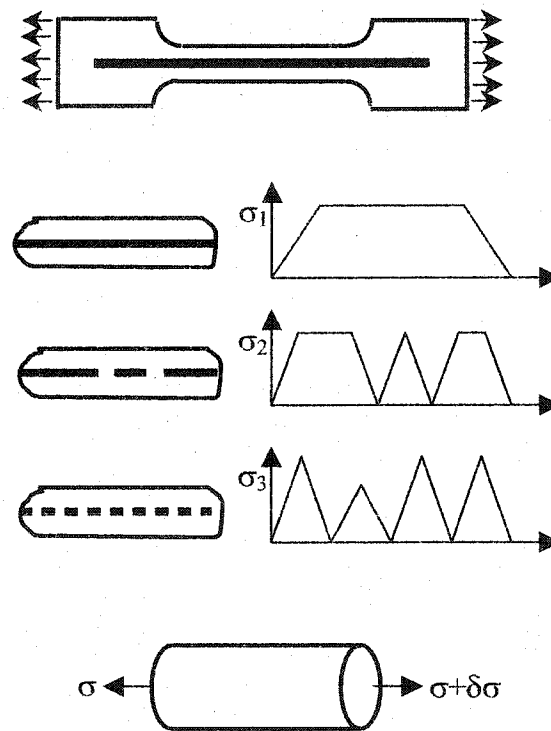


Fig. 1-19 Schematic illustration of the single-fiber fragmentation process.

The average shear strength at the interface, τ_a , can be approximately estimated from a simple force balance equation [73]

$$\tau_a = \chi \frac{\sigma_{TS}}{L_c} \quad (1.8)$$

where σ_{75} is the fiber's tensile strength at critical transfer length and a , the fiber radius. χ is a non-dimensional correction factor, which varies between 0.669 and 0.973 in order to take into account the statistical distribution of tensile strength and fragment length of the fiber.

The fiber fragmentation test is at present one of the most popular methods to evaluate the interface properties of fiber-matrix composites. This method is, however, limited due the fact it is difficult to measure the length of fiber fragments. Unless the matrix is transparent, one has to dissolve the matrix in order to measure the length of fiber fragments. In addition, the interfacial tensile strength cannot be measured using this method.

Fiber pull-out test

During the pull-out test, a fiber or filament embedded in a matrix block is pulled out, as shown in Fig.1-20(a), (b) and (c). A tensile force is applied to the free end of the fiber and eventually pull it out from the matrix as the force is steadily increased [74~77]. Load and displacement are monitored during the pulling process. The initial stress for interfacial debonding, σ_0 , and the maximum debonding stress at instability, σ_d^* can be determined from the load ~displacement curve as illustrated in Fig. 1-21. This technique can be modified for convenient application in practice, as shown in Fig. 1-20(d) [78].

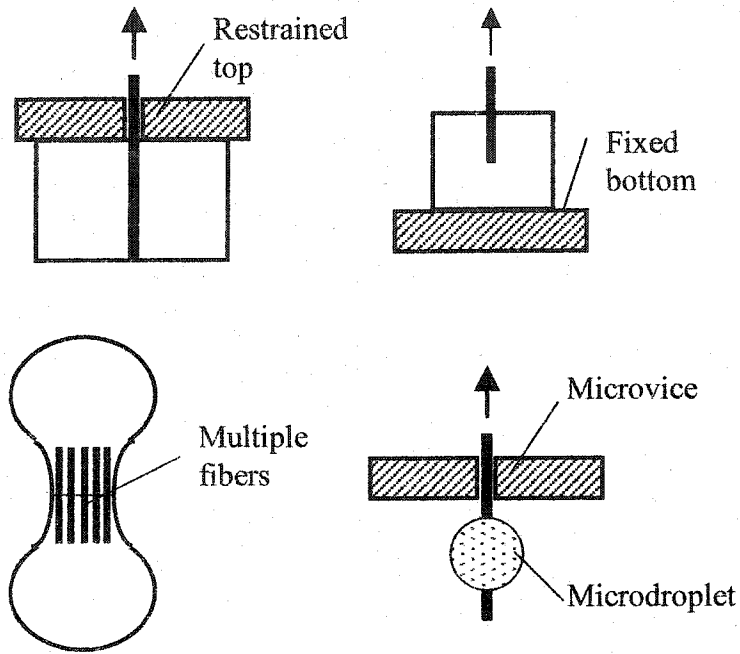


Fig. 1-20 Various fiber pull-out tests.

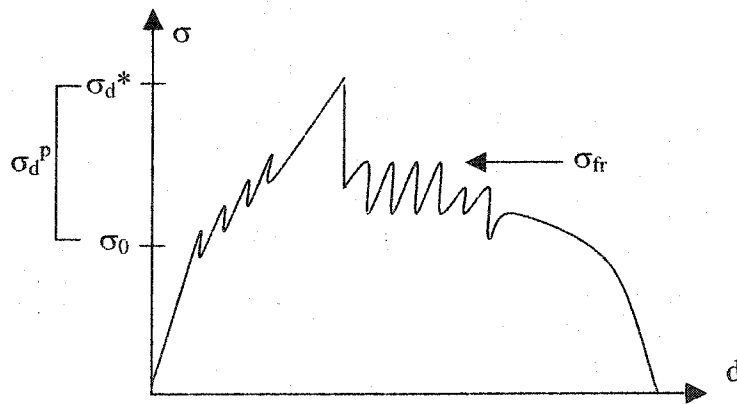


Fig. 1-21 A typical stress versus displacement curve involving interfacial debonding.

The interfacial bond strength, τ_b , can be determined using an equation [76]

$$\tau_b = \frac{d\sigma_d^*}{4L} \quad (1.9)$$

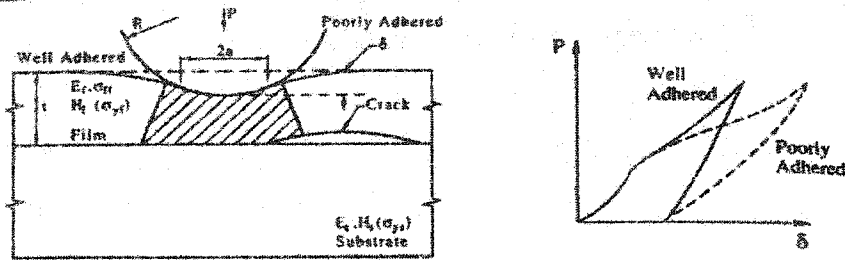
where L is the embedded fiber length and d is the fiber diameter.

The fiber pull-out test has been widely used not only for polymer matrix composites but also for some ceramic matrix and cement matrix composites. However, this test method has some limitations, e.g., there is a maximum embedded fiber length, permitted for pull-out without being broken. This length is usually very short, which causes experimental difficulties and large data scattering, especially for composites with strong interfacial bonds and small fiber diameters. An alternative pull-out method, so-called microbond technique [59], has been developed to facilitate the pull-out test (see Fig. 1-21(d)).

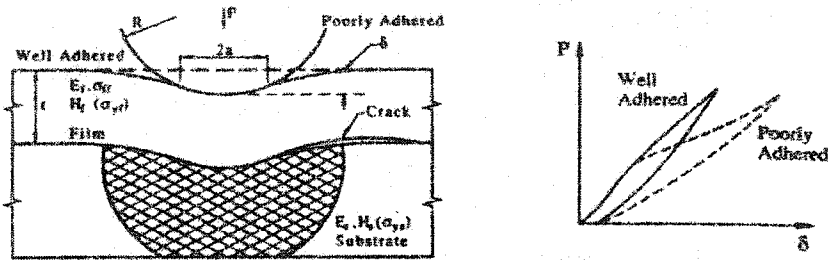
Although the pull-out test is a simple method to evaluate the interfacial bond for fiber-reinforced composites, this technique does not provide information on tensile strength and therefore the interface cannot be completely evaluated.

1.5 Microindentation test

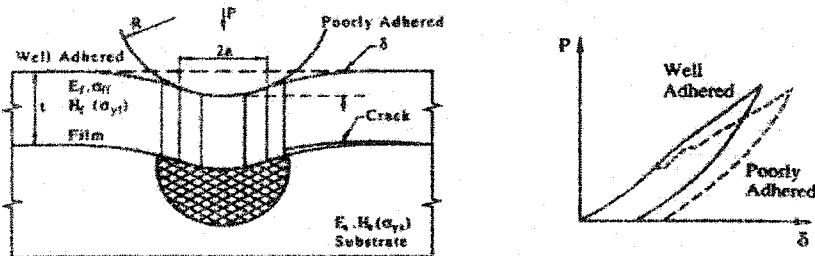
Along with the development of microindentation technique for mechanical testing, this technique has also been used for evaluation of interfacial bond for both coatings and composites on micro-level. Indentation may be performed at the surface of a coated sample [79,80]. The force-displacement curves of various film/substrate combinations have been investigated in detail in Ref [79], as shown in Fig. 1-22.



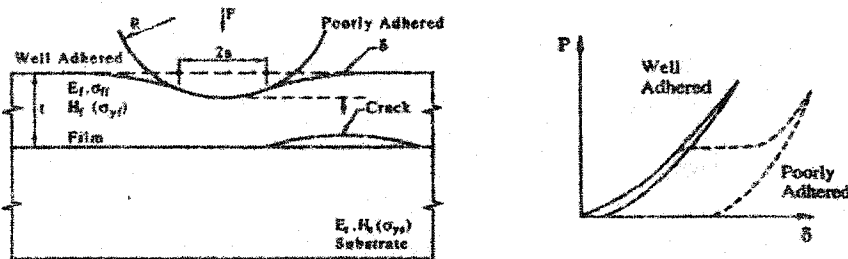
a) Ductile film on stiff hard substrate ($\sigma_{yf} \ll \sigma_{ys}$) e.g. Pt or Cu on Si



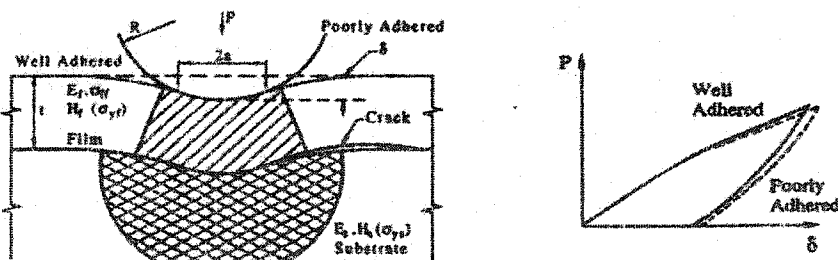
b) Hard strong thin films on a soft substrate ($\sigma_{yf} \gg \sigma_{ys}$) e.g. DLC on metals (Fe)



c) Hard brittle film on softer substrate ($\sigma_{yf} < \sigma_{ys}$) e.g. TiN on steel



d) Compliant elastic film on hard stiff substrate ($E_f \ll E_s, \sigma_{yf} / E_f \uparrow$) e.g. polymer



e) Hard ductile film on softer substrate ($\sigma_{yf} > \sigma_{ys}$) e.g. NiP on steel

Fig. 1-22 Schematic cross-sections and force-displacement curves of various film/substrate interfaces [Ref. 79].

It can be seen that various kinks occur on the force-displacement curves, which could be used to judge the initiation of interfacial cracking. However, such judgement is not easy to be made since the difference between well-bonded and poorly-bonded interfaces is not significant. Furthermore, the kinks may also come from fracture of the coatings, which makes such test less reliable.

Microindentation may also be applied on a cross-section at the interface as shown in Fig. 1-23 [81]. The critical load could be obtained from the loading curve, under which the crack length a can be determined at the interface. This method is more suitable for thick and ductile coatings, since cracking may not occur in the coating before interfacial debonding takes place during the loading process [82].

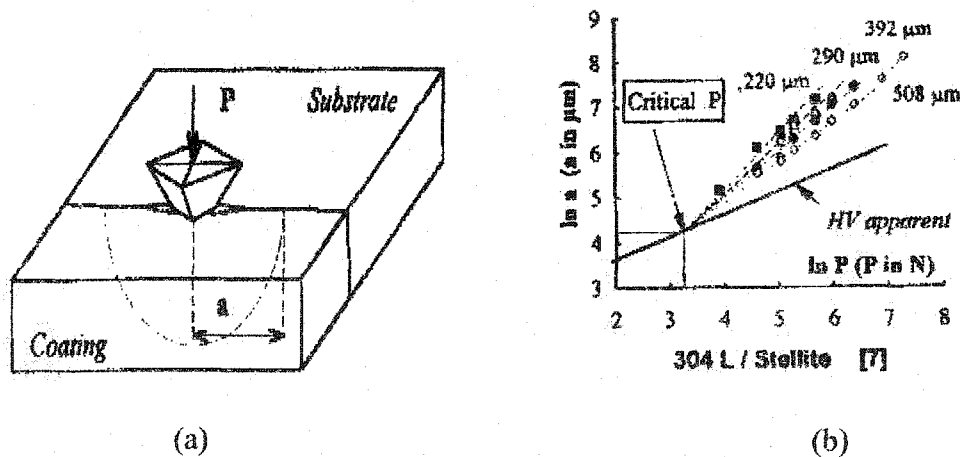


Fig. 1-23 Determination of interfacial debonding using the interfacial indentation test. (a) indentation test, and (b) a corresponding $\ln a \sim \ln P$ curve [Ref. 81].

Microindentation may also be applied on the cross-section at the substrate side near the interface [83,84] as shown in Fig. 1-24. The interfacial crack length under a certain load is a measure of the interfacial bond. Obviously, when the same load is applied on materials with different properties, the generated interfacial stresses are different. Therefore, this method cannot be used to evaluate the interfacial bond strength precisely. Moreover, it cannot predict the initiation of interfacial debonding.

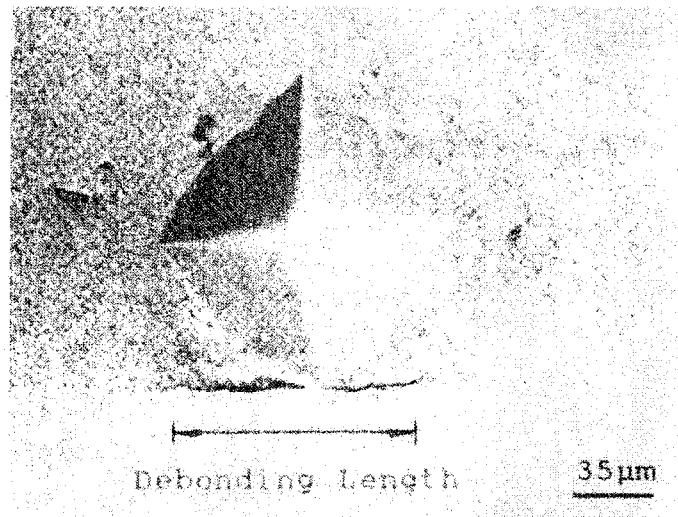


Fig. 1-24 Interfacial debonding induced by Vickers indentation [Ref. 84].

Microindentation is also used to evaluate the interfacial bond for composites, shown in Fig. 1-25 [85-88]. This is a single-fiber test by pushing a short fiber out from the matrix, using a spherical indenter. The interfacial debonding is monitored under an optical microscope during the process. The interfacial bond strength, τ_b , is calculated using the following equation [84]:

$$\tau_b = \sigma_d \left(\frac{\tau_{\max}}{\sigma_f} \right)_{FEM} \quad (2.9)$$

where σ_d is the average compressive stress applied to the fiber end at debonding. τ_{max}/σ_f is the ratio of the maximum interface shear stress to the applied stress calculated using the finite element method (FEM).

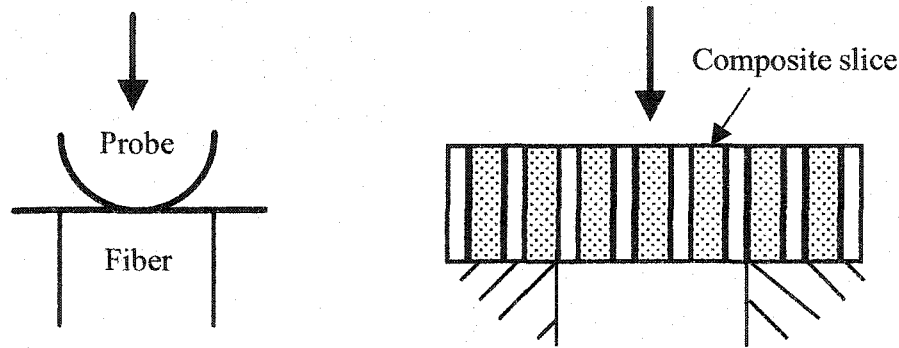


Fig. 1-25 The push-out indentation test for evaluation of interfacial bond for fiber-reinforced composites.

The microindentation test is also used for metal-matrix composites to determine their interfacial bond between the matrix and reinforcing particles as shown in Fig. 1-26 [89]. A Vickers indenter is pressed near an interface and the total debonding length (an interface crack) is measured, which is used to evaluate the interfacial bond strength.

Although it has some shortcomings, microindentation appears to be a promising technique for further development. This method has less geometrical limitation and can be used to evaluate the bond strength of various interfaces for coatings and composites. In addition, this method can be performed at the microscopic level and therefore, it could minimize the influence of flaws, pores and other defects at the interface by selecting a “defect-free”

region for testing. Such obtained results may reflect the intrinsic interfacial bond strength. However, without a revolutionary modification or improvement, it is difficult to apply microindentation to determine the interfacial bond strength quantitatively and precisely.



Fig. 1-26 Evaluation of the interfacial bonding for a NiAl-matrix composite. An interfacial crack is indicated by an arrow [Ref. 89].

1.6 Statement of problems and objective of the research

As discussed above, determination of interfacial bond strength is an important and difficult task. Although a number of experimental techniques have been developed to evaluate the interfacial bond strength for coatings and composites, their applications are rather limited [2]: (1) lack of transferability of measurement results, that is, the result obtained using one method may not be consistent with that obtained using another method; (2) lack of generality for different types of interface; and (3) unjustified hypotheses or assumptions have been used to build the methods. (4) Many techniques only provide qualitative or semi-qualitative evaluation with low reliability. Therefore, a

more general and effective technique is urgently required for the determination of interfacial bond strength for both coatings and composite materials.

The objective of this work is to develop such a general technique that can be used to quantitatively determine interfacial bond strength for different types of interfaces.

This thesis consists of six chapters. Chapter 1 presents a brief review of types of interfacial bonds and current methods used to evaluate the interfacial bond strength for coatings and composites. The main body of the thesis consists of four chapters, from Chapter 2 to Chapter 5. In Chapter 2, a novel method, so-called lateral force-sensing microindentation method, is proposed. During indentation near an interface, the critical load at the initiation of interfacial debonding, can be obtained from changes in lateral force. In conjunction with the finite element method (FEM), the interfacial bond strength can be quantitatively determined. This novel method is justified experimentally and computationally. In Chapter 3, the mechanisms responsible for interfacial debonding for different interfaces are analyzed and discussed. In Chapter 4, research on optimization of this method is presented, which includes effects of indenter shape, indenter size and indentation position on the sensitivity of the method to interfacial debonding. Chapter 5 presents application of this method in evaluating interfacial bond strengths for thermal-sprayed coatings in comparison with the traditional tensile test. In Chapter 6, general conclusions are given and some future studies are suggested.

Chapter 2

Development of a novel lateral force-sensing microindentation technique

In this chapter, a novel method, the so-called lateral force-sensing microindentation technique, is introduced to evaluate the interfacial bond strength for coatings/films and composite materials. This new method was developed based on previous studies on several indentation methods, as described in Chapter 1. It was found that the previous methods were not sufficiently sensitive to the interfacial debonding and had difficulty to quantitatively and precisely evaluate the interfacial bonds. For the lateral force-sensing indentation method, microindentation was performed near an interface with *in situ* monitoring of changes in lateral force. It was demonstrated that the lateral force (F_x) was very sensitive to interfacial debonding. The critical indentation load that corresponds to interfacial debonding can be measured and used to quantitatively determine the interfacial bond strength, in conjunction with the finite element analysis (FEM). The method was justified using experimental and computational approaches. As an example, an Al₂O₃/Al alloy interfacial bond was tested and analyzed using this new technique.

2.1. Experimental procedure

Microindentation experiment was performed using a Micro-Tribometer, made by the Center for Tribology (California, USA) as schematically illustrated in Fig.2-1. The sample was fixed on the sample holder, which can move in different directions to adjust the indentation position. The normal load, lateral force (F_x), acoustic emission and indentation displacement were recorded during indentation. An optical microscope was attached to determine the position for microindentation.

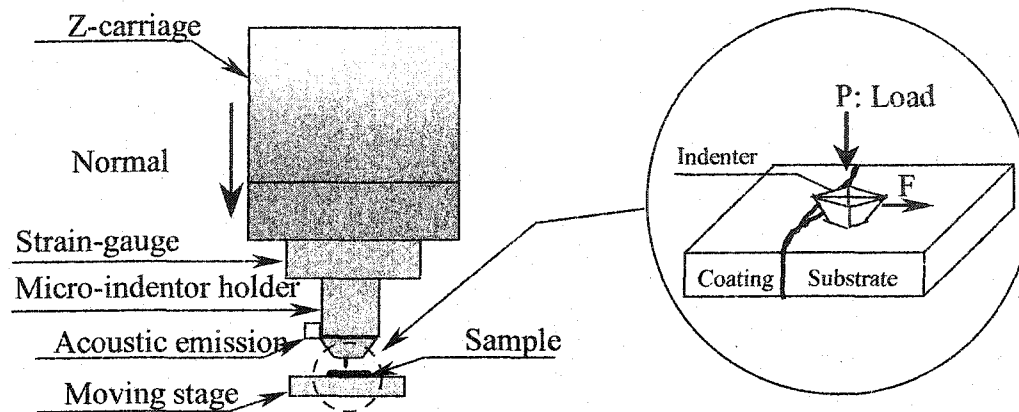


Fig. 2-1. Schematic diagram of the indentation measurement.

In this research, $\text{Al}_2\text{O}_3/\text{Al}$ alloy 6061 interface was used for a sample study. Specimens were made by adding pieces of Al_2O_3 into molten Al 6061 at 800°C , followed by furnace cooling. The specimens were cut using a diamond saw and the final dimensions of a specimen containing ceramic/metal interface were $8 \times 15 \times 50\text{mm}$. The cross-sectional surface of the specimens was polished and their final roughness was $0.05\mu\text{m}$. In order to evaluate the sensitivity of the microindentation method for different bond strengths, artificial interfaces were also made by bonding Al_2O_3 and steel 4045 using different adhesives. Al_2O_3 and steel 4045 pieces having a size of $30 \times 20 \times 15\text{mm}$ and surface roughness of $0.05\mu\text{m}$ were glued together with super glue (Loctite Corp., Quicktite), epoxy glue (Gougeon Brothers Inc., 105A) and wax (British Wax Refining Ltd), respectively; interfacial bonds of these samples were evaluated using the microindentation method.

Microindentation was performed at the cross section of an $\text{Al}_2\text{O}_3/\text{Al}$ alloy specimen near the interface at the Al alloy side. A cone-shaped tungsten carbide indenter having a tip radius of 0.2 mm and tip angle of 30° was used. For an $\text{Al}_2\text{O}_3/\text{steel}$ bond, the indentation was performed at the steel side near the interface. A normal load was applied to the indenter, which was linearly increased from zero to a maximum load of 40N at a rate of 0.22N/sec. During the test, the normal load, time and lateral force were recorded simultaneously. The sample surface after each test was examined with a SEM. Each indentation test was repeated 5 times and results presented in the thesis are average values for 5 measurements. The standard deviation was in the range of 8%.

2.2 Examination of currently existing microindentation methods

To determine the interfacial bond strength, a method should have the ability (1) to produce sufficiently large stress to break the interface; and (2) to detect the initiation of interfacial debonding with high sensitivity. Considering the currently existing methods to evaluate the interfacial bond strength, the microindentation is the only method that can be applied for both composites and coatings. The present work began with examining the currently existing indentation methods. As discussed earlier, direct application of indentation on a coating surface is an ineffective way to determine the interfacial bond strength. Therefore, in this work, the emphasis is put on the cross-section near an interface to evaluate its bond strength.

First, microindentation was applied at the Al 6061 side near an $\text{Al}_2\text{O}_3/\text{Al}$ 6061 interface. The loading and unloading curves were recorded. It was expected that the interfacial

failure could be detected by unusual changes occurring on the force-depth curve, e.g., kinks. After indentation test, the interface was examined with a SEM. Results for many such tests indicate that when indentation produced a crack at the interface as shown in Fig. 2-2, the loading and unloading curves did not always show a kink, which corresponds to interfacial debonding. Fig. 2-3 is a typical force~depth curve. This method is therefore not sensitive to the interfacial debonding as expected.

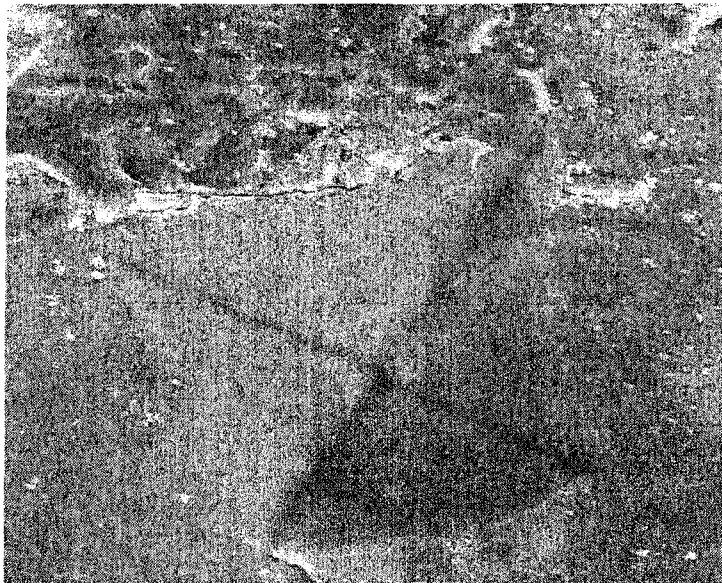


Fig. 2-2 Interfacial debonding caused by microindentation.

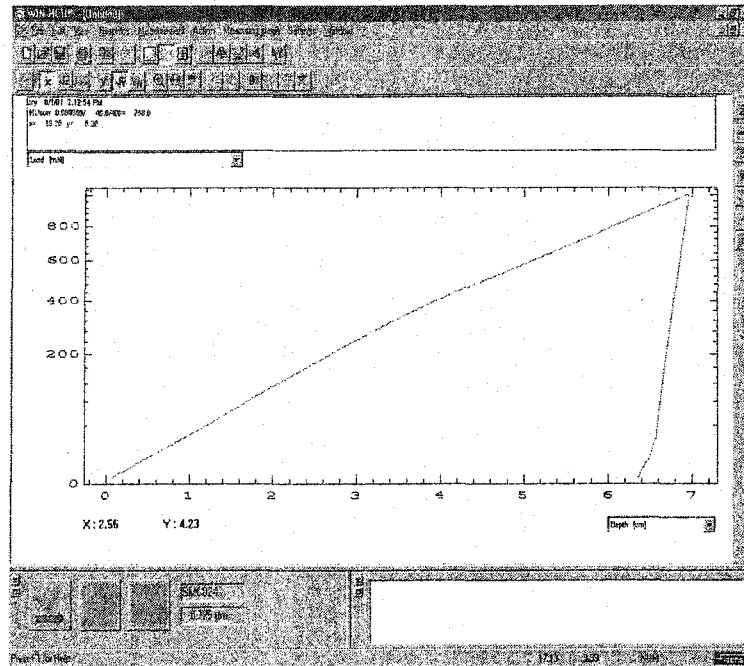


Fig. 2-3 Typical loading and unloading curves of microindentation with interfacial cracking.

Acoustic emission signals (AE) were also monitored to see if they were sensitive to the interfacial debonding. When indentation was applied at the Al 6061 side near an interface, AE was not sensitive to interfacial debonding (Fig. 2-4). However, when indentation was applied directly at the interface, AE signals became rough with many peaks (Fig. 2-5). These signals may come from interfacial cracking and brittle fracture of the hard phase, Al_2O_3 , as well. It was difficult to identify which peak corresponded to interfacial failure. In summary, acoustic emission and the force ~ depth curve are not reliable for determining the interfacial debonding.

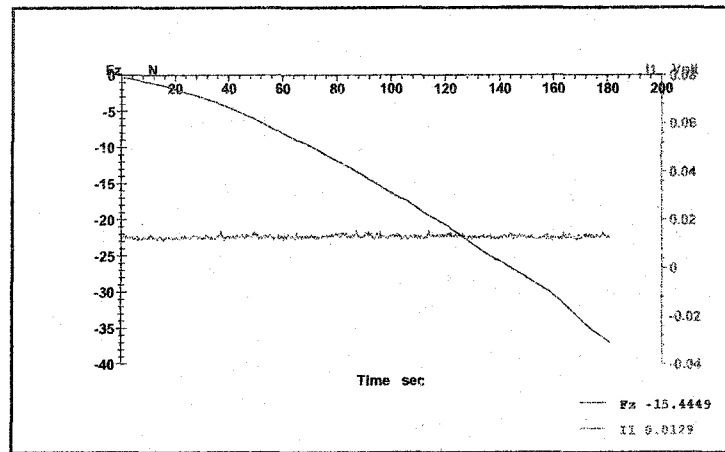
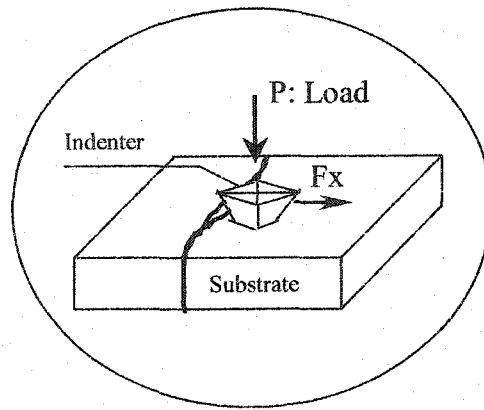


Fig.2- 4. Acoustic emission response for indentation test near an interface.

2.3 The lateral force-sensing indentation method

The failure in evaluation of interfacial debonding using the force~depth curve or acoustic emission redirected our attention to search for more suitable parameters for detecting interfacial debonding during indentation. It was interesting to notice that the lateral force

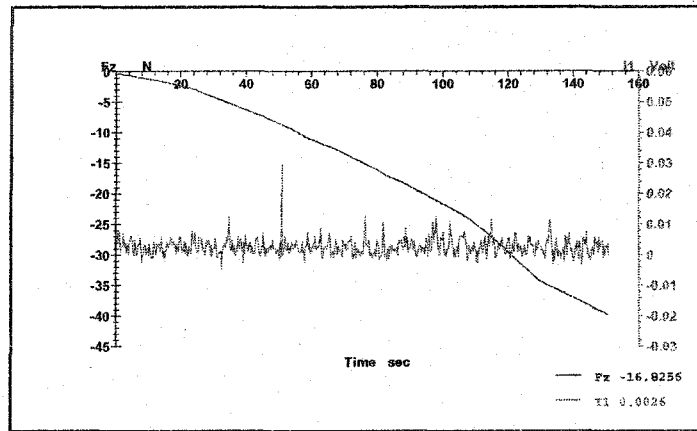
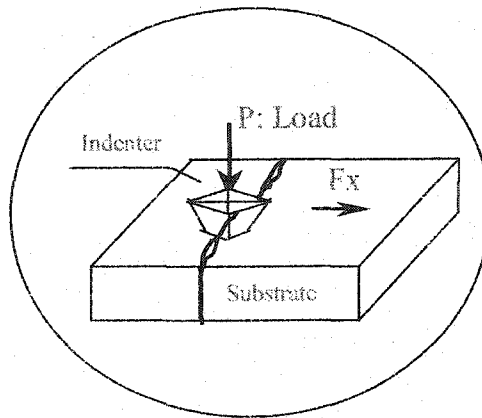


Fig. 2-5. Acoustic emission response for indentation at interface.

on the indenter showed unusual changes when interfacial debonding occurred. Typical normal load versus time curve and lateral force versus time curve for indentation on an $\text{Al}_2\text{O}_3/\text{Al}$ alloy specimen are illustrated in Fig.2-6. As shown, when the normal load was increased, the lateral force (F_x) changed correspondingly. At the beginning, F_x increased gradually and the tip was pushed away from the interface. When the normal load was about 10N, the lateral force decreased and the tip moved backward as the normal load

was continuously increased. Such a change corresponds to a change in the slope sign of the $F_x \sim t$ curve. It was noticed that each time when the slope of $F_x \sim t$ changed its sign, interface cracking was observed as shown in Fig.2-7.

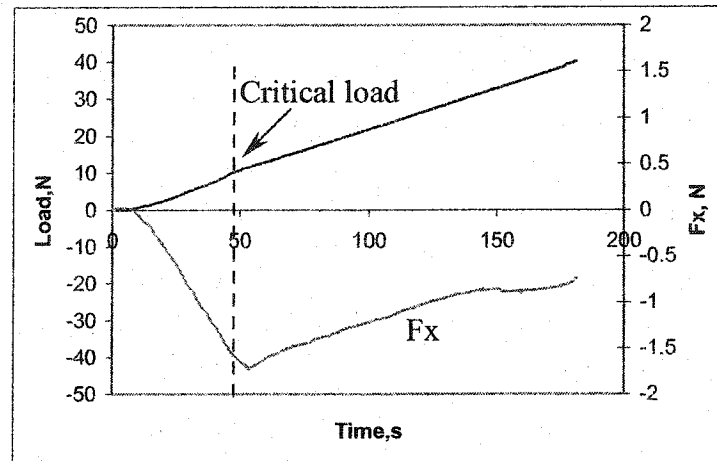


Fig. 2-6. Load-time and lateral force F_x -time curves of an Al_2O_3/Al alloy bond.

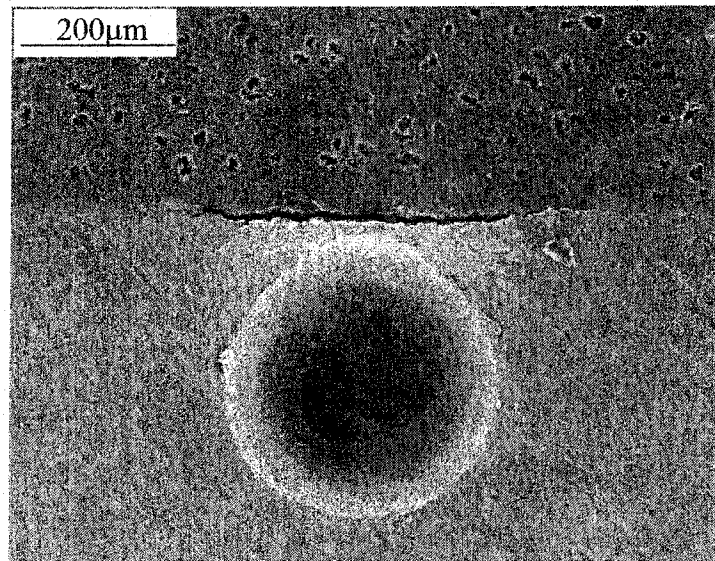


Fig. 2-7 Debonding at an Al_2O_3/Al alloy interface caused by indentation.

In order to confirm this phenomenon, similar tests were performed for $\text{Al}_2\text{O}_3/\text{Steel 4045}$ interfaces with different bond strengths. When the load was applied to a specimen with a weak bond (Fig. 2-8(a)), cracking initiated at a critical normal load (L_c) was about 5N; For a medium bond (Fig.2-8(b)), the critical normal load (L_c) was about 30N. A high-strength interface with a superglue bond was also tested. Under this condition, there was no slope-sign change on the $F_x \sim t$ curve during the entire loading process (see Fig.2-8(c)). Surface observation under SEM indicated that interfacial cracking occurred in cases (a) and (b) only after the $F_x \sim t$ curve slope-sign changed at L_c . No interfacial cracking was observed in case (c). It appears that the change in the sign of the slope of $F_x \sim t$ curve could be considered to be a critical point corresponding to interfacial cracking and the corresponding normal load may be taken as the critical load that results in interfacial debonding.

A possible mechanism responsible for the variation in lateral force during indentation is illustrated in Fig.2-9. When indentation is performed on a homogeneous bulk material, the constraints of the specimen to a conical indenter in all radial directions are the same and the lateral force is zero because of the cylindrical symmetry. However, when indentation is carried out near an interface, the constraint around the indenter is no longer symmetrical due to the difference in mechanical properties between the materials that form the interface. As a result, a lateral force would occur. When the indentation load increases, this asymmetric constraint may increase, resulting in an increase in F_x . When the indentation load is sufficiently large, interfacial debonding would occur. At this point,

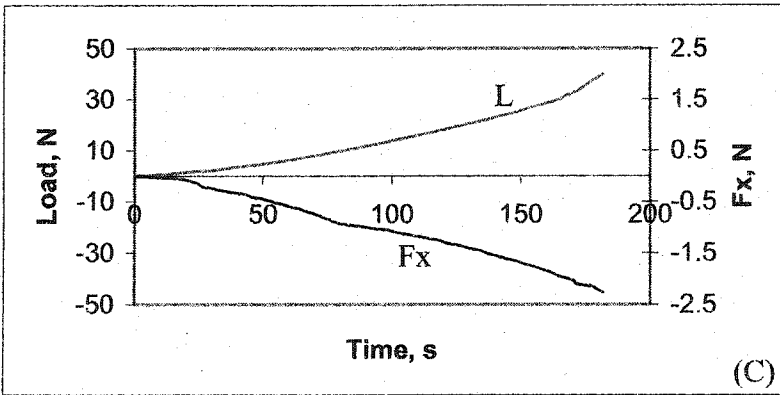
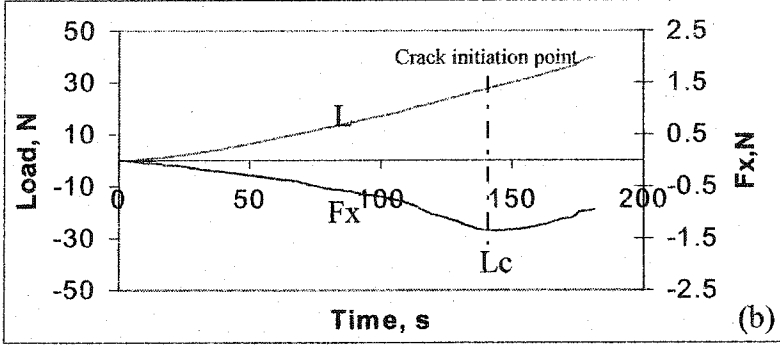
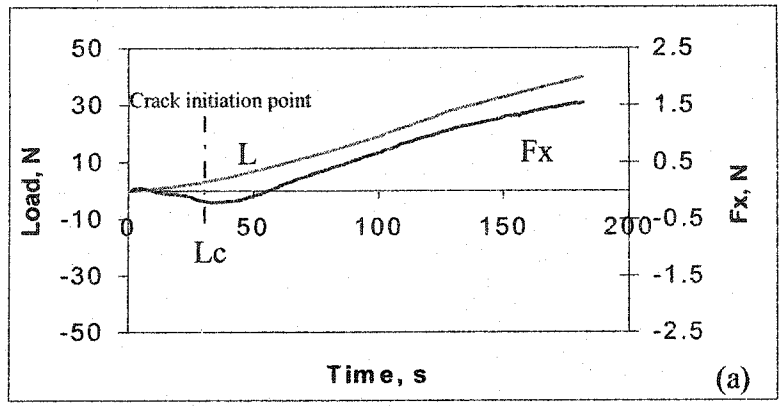


Fig. 2-8. Normal load-time and lateral force-time curve of Al_2O_3 /Steel 4045 bonds; (a) weak bond, (b) medium bond, and (c) strong bond.

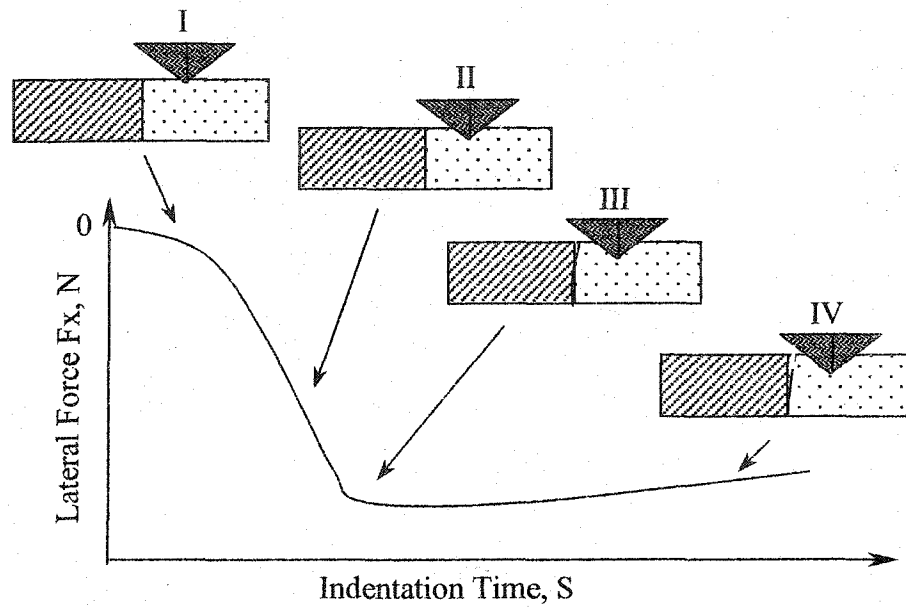


Fig. 2-9. Schematic illustration of an interfacial debonding process and corresponding changes in lateral force.

the constraint from the interface to the indenter would decrease so that the lateral force could not keep the previous trend, resulting in the change in slope sign of the $F_x \sim t$ curve as shown in Fig.2-6. Such a change may allow us to determine the initiation of interfacial debonding and corresponding indentation load. This critical load could be related to the interfacial bond strength using the finite element method (FEM). Details about the FEM analysis have been given in a later section of this chapter.

2.4 Further justification by computer modeling

In order to further justify the proposed correlation between interfacial debonding and the sign change of the slope of $F_x \sim t$ curve, an indentation process was modeled using a micro-scale dynamic model (MSDM) [90,91]. In this model, a given specimen is discretized using a discrete lattice as illustrated in Fig. 2-10. Each lattice site represents a small volume of the material. Under the influence of an indentation force, a lattice site may move, governed by Newton's law of motion to predict the trajectories of lattice sites:

$$\vec{F} = m \frac{d^2 \vec{r}}{dt^2} \quad (2.1)$$

where m is the mass of a lattice site, \vec{r} is the position of the site and t is the time. The total force \vec{F} on a site includes the interaction between the site and its adjacent sites as well as the external force from indenter if the site is at the surface.

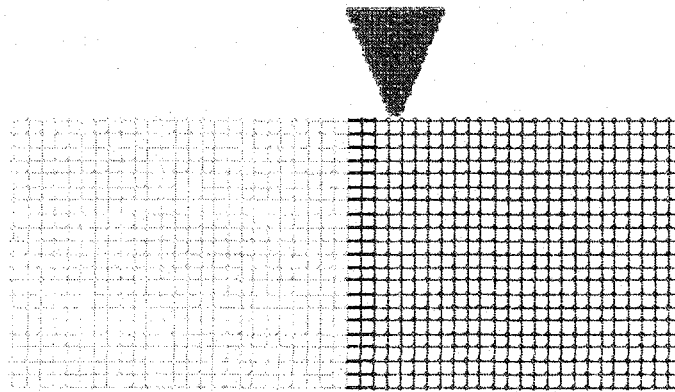


Fig. 2-10 A system, used for modeling study (MSDM), is discretized and mapped onto discrete lattices.

The simulated system material includes two parts. One is hard (ceramic) and the other is soft (metal). They are connected by an interface (Fig. 2-10). For a homogenous material, the interaction between two adjacent sites is dependent on the mechanical properties of the material, which include the elastic modulus, the yield strength, the tensile strength, the ductility and work hardening. The site-site interaction may be expressed as:

$$\vec{f} = k \cdot \Delta \vec{l} \quad (2.2)$$

where $|\Delta \vec{l}|$ is the magnitude of deformation of the bond connecting a pair of adjacent sites. It can be calculated by subtracting the stress-free bond length from the bond length after deformation under the force: $\Delta \vec{l} = \vec{l} - \vec{l}_0$. The coefficient k is equal to $E \cdot l_0$, where E is the slope of the stress-strain curve of the material. Fig. 2-11 illustrates a stress-strain curve. Within the elastic region, the curve is linear, corresponding to the elastic modulus E_e ; while in the plastic region the “modulus” varies with the strain. In the elastic region, $E = E_e = \frac{\sigma_y}{\varepsilon_y}$, where σ_y and ε_y are the yield stress and yield strain, respectively. In the plastic region, $E = E_p = \frac{(\sigma_T - \sigma_y)}{(\varepsilon_T - \varepsilon_y)}$. If the deformation Δl is within the region of elasticity, E is equal to the elastic modulus (E_e), if the deformation Δl exceeds the elastic region, E is equal to the plastic modulus E_p . When the deformation Δl is smaller than zero, two sites are under compression. In this case, we assume E is equal to the elastic modulus and no damage to the bond will result. The site-site bond will not be broken when the sites approach to each other under a compressive stress. Only when the bond is elongated and its deformation is larger than the strain at fracture, will the bond be broken.

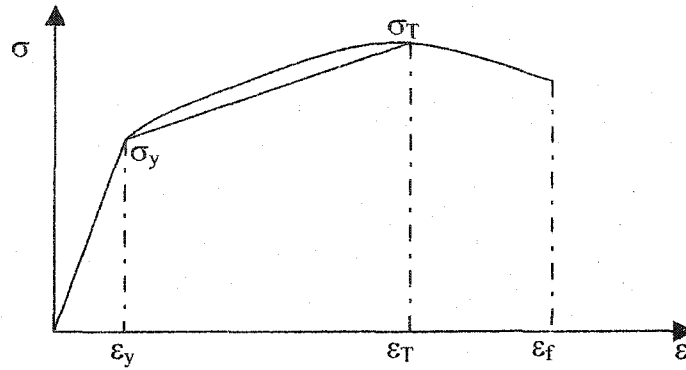


Fig. 2-11. Schematic illustration of a stress-strain curve.

The total force on a surface site, P , that is in contact with the indenter may be expressed as:

$$\vec{F}_p = \sum_q^n k \cdot \Delta \vec{l}(p, q) + \vec{f}_p \quad (2.3)$$

where, n is the number of sites q adjacent to site p , \vec{f}_p is an external force exerted by the indenter. If site P is not in contact with indenter, \vec{f}_p is equal to zero. When the total force on the site is known at time t , its velocity and position after a time interval Δt are determined by

$$\vec{V}_{t+\Delta t}(p) = \vec{V}_t(p) + \frac{1}{m} \vec{F}_t(p) \Delta t \quad (2.4)$$

$$\vec{r}_{t+\Delta t}(p) = \vec{r}_t(p) + \vec{V}_t(p) \Delta t \quad (2.5)$$

where \vec{V}_t and $\vec{V}_{t+\Delta t}$ are velocities of site P at time t and $t + \Delta t$, respectively, and $\vec{F}_t(P)$ is the total force on site P at t ; \vec{r}_t and $\vec{r}_{t+\Delta t}$ are positions of site P at t and $t + \Delta t$, respectively. In such a way, the trajectory and position of each lattice site can be predicted. When the length of a bond between two adjacent sites exceeds a critical value corresponding to the fracture strain of the material, the bond fails. Using this method, a dynamic indentation process could be simulated.

All interfacial bonds in this simulation study were assumed to be elastic and had the same fracture strain. In order to investigate the response of an interfacial bond to indentation, three interfacial bonds with different strengths were considered. A strong bond had its maximum tensile strength almost the same as that of the ceramic bond. The middle bond, whose strength was between those of the ceramic bond and the metal bond, and weak bond, whose strength was weaker than the metal bond.

Using the model, indentation near each of the interfaces was simulated. Lateral movement of the indenter, which corresponded to the lateral force, was recorded. Fig. 2-12~ 2.14 illustrate the results of the simulation.

For the weak interfacial bond, as Fig. 2-12 illustrates, the tip continuously moved toward the interface during indentation, and almost all the interfacial bonds were broken. For the strong interfacial bond, as Fig. 2-14 illustrates, the tip continuously moved away from the interface. In the case of the medium interfacial bond as shown in Fig. 2-13, the tip moved

away from the interface at first, and it later moved towards the interface when interfacial debonding occurred.

The simulation is consistent with experimental observations. Since the “computational experiment” was performed under controllable condition with given bond strength. This consistence between simulation and experiment provides support for the proposed correlation between interfacial debonding and the change in slope sign of the $F_x \sim t$ curve.

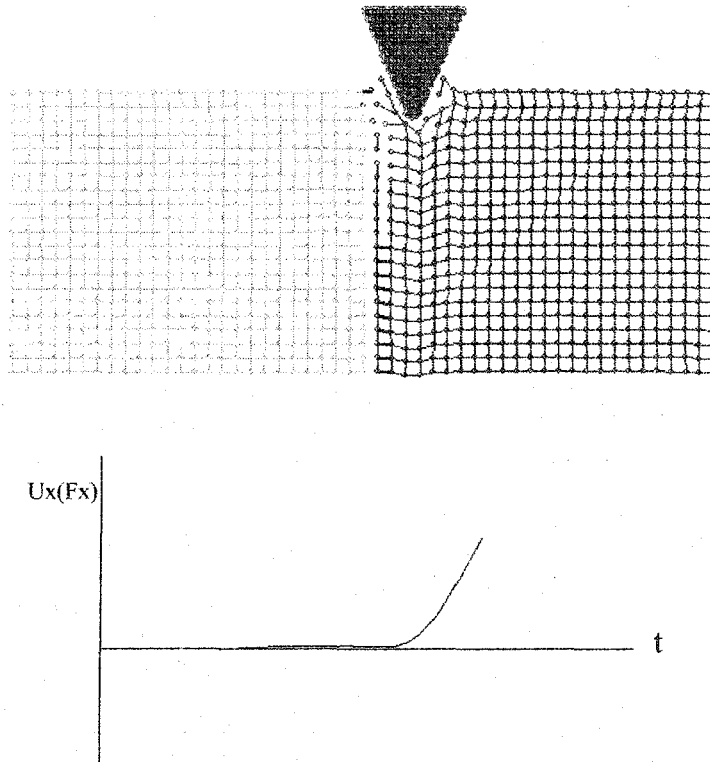


Fig. 2-12. Simulation of indentation near an interface and corresponding lateral displacement (or force) of the indenter as a function of time for a weak bond.

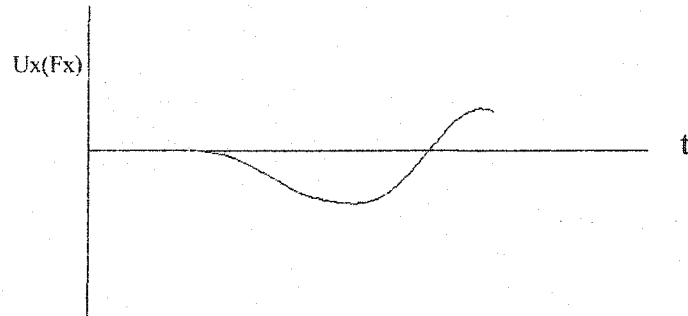
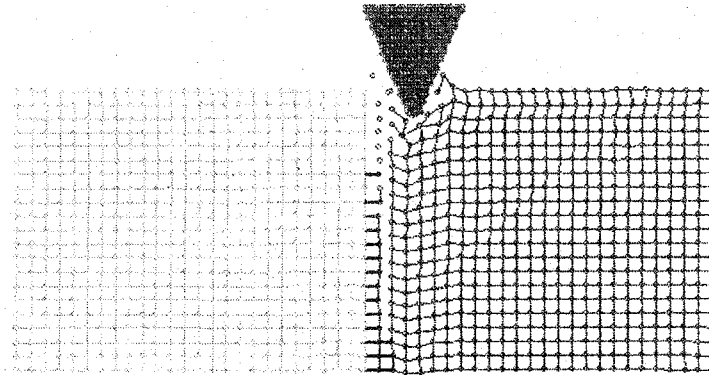
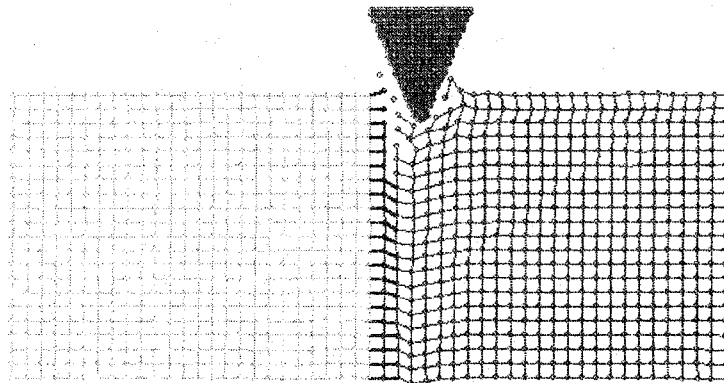


Fig. 2-13 Simulation of indentation near an interface and corresponding lateral displacement (or force) of the indenter as a function of time for a medium bond.



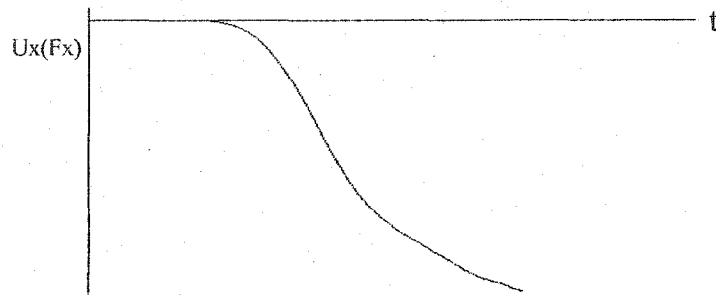


Fig. 2-14 Simulation of indentation near an interface and corresponding lateral displacement (or force) of the indenter as a function of time for a strong bond.

2.5 Interfacial stress analysis and determination of the interfacial bond strength

2.5.1 Finite element analysis

As demonstrated earlier, the critical indentation load for interfacial debonding may be determined by monitoring the change in the slope sign of the lateral force~time curve. After the critical load is determined, with known geometry and location of the indenter, it is possible to evaluate the interfacial bond strength by analyzing the stress state in the vicinity of the interface using the finite element method.

In this study, the stress distribution around an indenter was determined using the ANSYS software package (version 6.1). As an example, stress and strain around an Al_2O_3/Al 6061 interface, corresponding to the critical indentation load on a conical WC indenter, were analyzed. Since the indentation introduced plastic strain, the problem was non-linear. For simplicity, the indenter was treated as a rigid body and the surface-to-surface contact was applied.

In order to be consistent with the indentation test, all parameters used for the FEM simulation had the same values as those for the experiment, such as the geometry and location of indenter and material properties. The simulated sample had free side boundaries with its bottom fixed. The sample was big enough so that the stress/strain around the indenter was localized with negligible influence of the boundary condition. The Al_2O_3 phase was fully elastic with its Young's modulus and Poisson's ratio equal to 360GPa and 0.25, respectively. Plastic behavior of the Al alloy was modeled using multilinear isotropic hardening approach, along with the Von Mises stress yield criterion. The mechanical properties used in the finite-element model were obtained from literature [92]. The Young's modulus and Poisson's ratio of Al alloy were 70GPa and 0.3, respectively.

The region of indentation was discretized with fine mesh, which became progressively coarser at the distance from the indenter in order to reduce the computing time (Fig. 2-15). During the simulated indentation process, the indenter was pressed under a gradually increased load. The bottom boundary of the specimen was constrained in all directions. As an example, the stress components in the vicinity of an $\text{Al}_2\text{O}_3/\text{Al}$ alloy interface are illustrated in Fig. 2-16.

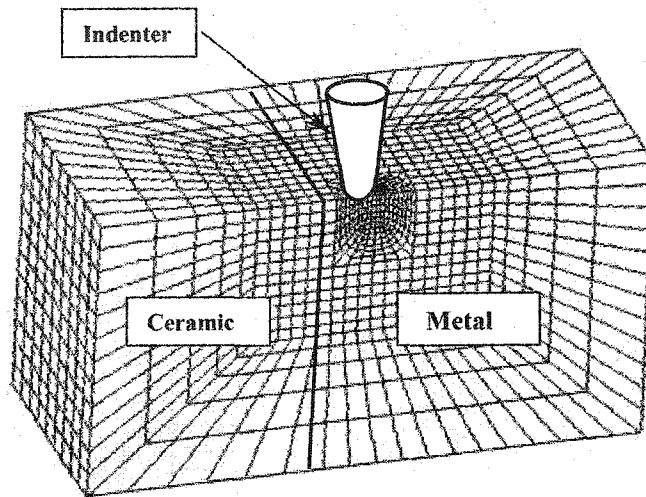


Fig. 2-15. A system for indentation modeling using FEM.

2.5.2 Interface failure criterion and interfacial bond strength

From the finite element analysis, the stress or strain distribution at interface can be determined. When indentation is performed near an interface, the stress at interface is usually multi-axial, that is, normal stress and shear stress coexist at interface, which makes the analysis of interfacial failure difficult. A criterion, therefore, needs to be chosen to determine interfacial bond strengths.

There are usually two basic approaches to evaluate the interfacial bonding. The mechanics of materials approach calculates the stress state at the interface and thus determines the interfacial bond strength with a stress value. The other approach is the strain energy release rate approach, which uses an energy value to evaluate the interfacial bond strength. Due to the fact that most testing methods use the stress value to evaluate

the interfacial bond strength, we adopt the former one so that the results can be directly compared with those from other methods.

Several models suggest that interfacial failure is caused by either the normal stress or the shear stress at the interface [93, 94]. When the interfacial normal stress or shear stress exceeds a critical value, the interfacial debonding occurs. However in general, real interfacial debonding involves the coupling of shear and normal stresses. Therefore, a general criterion for prediction of interfacial debonding should take the coupling effect into account.

In 1988, Brewer and Lagace [95] proposed a criterion, the so-called Quadratic Delamination Criterion (QDC), to determine the initiation of interfacial failure, which takes account of the coupling effect of normal and shear stresses. This criterion was proposed initially for interfacial delamination in composites and now has been widely used for various interfacial failure problems [96~98]. This criterion is adopted here to predict the onset of interfacial debonding.

$$\frac{(\sigma_{xz})^2 + (\sigma_{yz})^2}{(Z^s)^2} + \frac{(\sigma_{zz})^2}{(Z^N)^2} = \lambda = 1 \quad (2.5)$$

where σ_{xz} and σ_{yz} are interfacial shear stresses; σ_{zz} is interfacial normal stress; Z^N and Z^S are interfacial normal and shear strengths. When the left-side value of equation (2.5), which we define it as λ for convenience, is smaller than 1, there is no debonding at the interface. Therefore, Z^N and Z^S may be used to determine the interfacial bond strength.

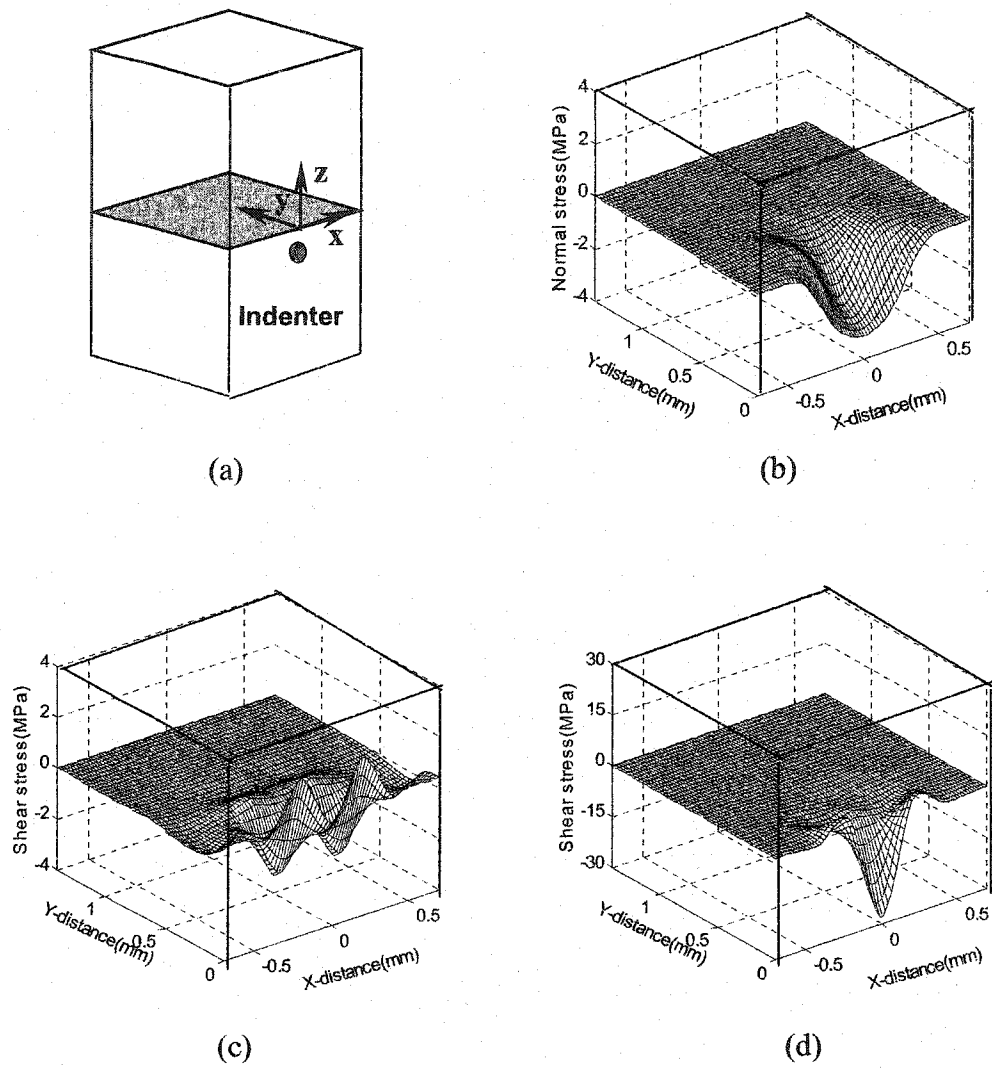


Fig.2-16. Normal and shear stress distributions at an $\text{Al}_2\text{O}_3/\text{Al}$ alloy interface under an indentation load. (a) indentation position and coordinates; (b) distribution of normal stress σ_{zz} ; (c) distribution of shear stress σ_{xz} ; and (d) distribution of shear stress σ_{yz} .

In order to determine two unknown parameters, Z^N and Z^S , which are used to evaluate the interfacial bonding strength, two indentation tests need to be performed at two different indentation locations to obtain two corresponding critical indentation loads. By substituting the data of local stress components corresponding to interfacial debonding into equation (2.5), we have two equations to determine two unknown parameters, Z^N and Z^S .

Regarding the position of debonding initiation, microscopic observation and FEM analysis show that debonding usually occurs on the sample surface at the interface. However, in order to avoid the possible situation that the crack may initiate in sub-surface at the interface, a procedure was proposed to determine both the position of crack initiation and (Z^N, Z^S) as a flow chart in Fig. 2-17 illustrates. The procedure is described as follows. We may perform two indentation tests at two different locations with different distances from the interface to obtain two critical indentation loads at interfacial debonding. For debonding analysis, we may choose any two nodes at the interface as possible debonding positions for these two indentation processes, separately, and calculate the corresponding normal and shear strengths (Z^N, Z^S). Then we may use the calculated (Z^N, Z^S) to test other points at the interface by substituting their σ_{xz} , σ_{yz} and σ_{zz} and the initially calculated (Z^N, Z^S) into left-hand side of equation (5), that is equal to λ . The λ value should be smaller than 1 if debonding does not occur at these points. Otherwise, we should choose another pair of two nodes as debonding points and repeat the above process until a pair of Z^N and Z^S , which can make λ for all other points less

the corresponding nodes are the positions where interfacial debonding initiates during these two indentation processes. As an example, (Z^N, Z^S) of an Al_2O_3/Al alloy bond was determined. The calculated tensile and shear strengths at interface are 10.6MPa and 28.5MPa, respectively.

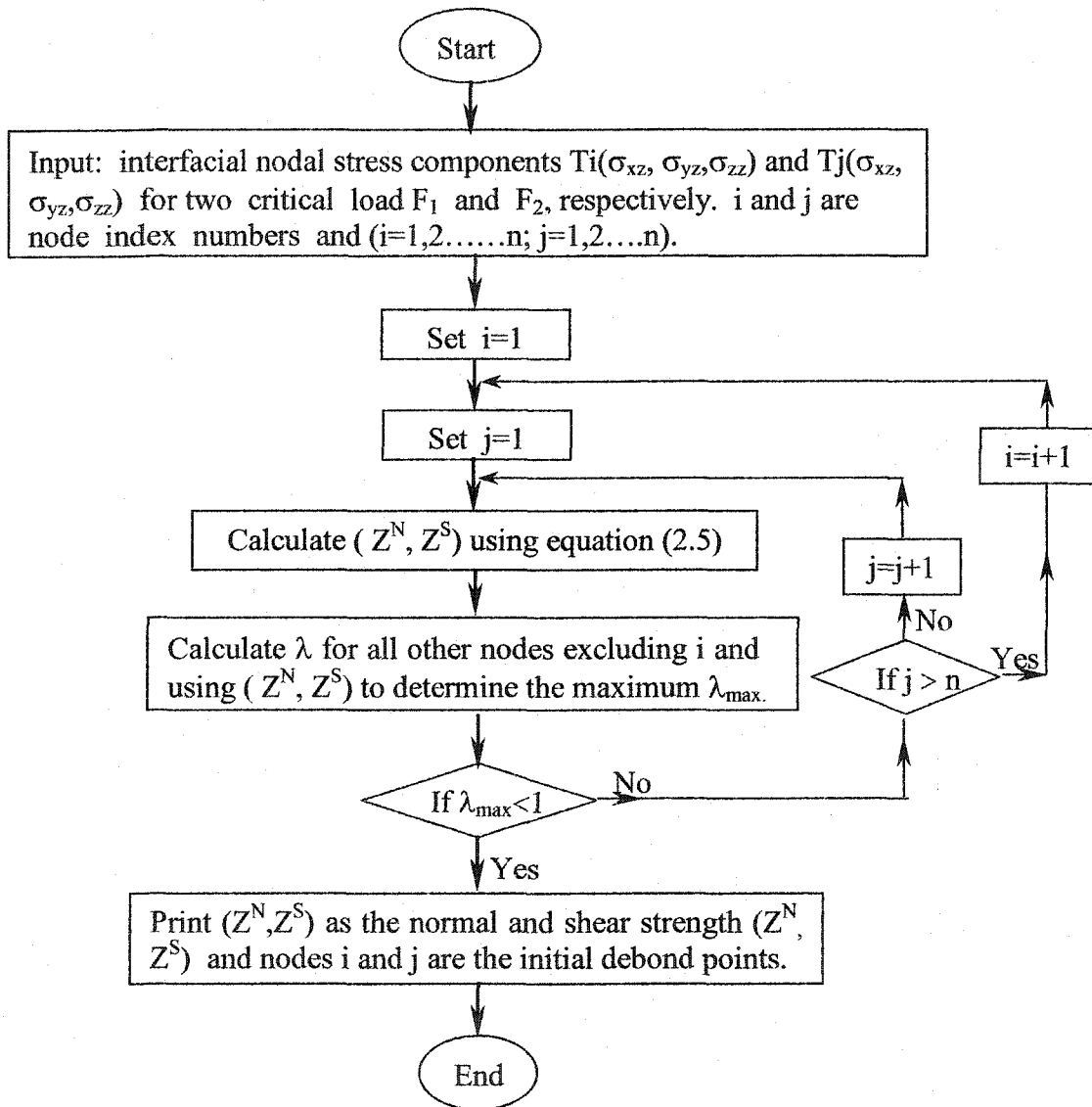


Fig. 2-17. A flow chart of the computational procedure used to determine the normal and shear strengths of an interface.

2.6 Comparison with a tension test

In order to justify the validity of the proposed method for determination of the interfacial bond strength, a tension test experiment was performed. Ten specimens with $\text{Al}_2\text{O}_3/\text{Al}$ alloy bond were made using the process described in section 3.1. The specimens had a size of $40 \times 8 \times 2 \text{ mm}$. Tensile stress was applied to the samples to determine the critical stress for debonding at the interface (Fig.2-18). The load~ displacement curve and acoustic emission signal during the tensile test were recorded as described in literature [99]. The first main AE peak was indicative of interfacial debonding.

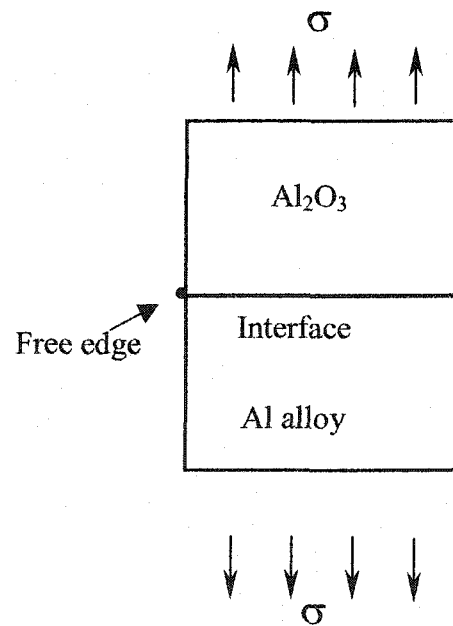


Fig. 2-18. Schematic of a tension test for determination of the bond strength of an $\text{Al}_2\text{O}_3/\text{Al}$ alloy interface.

It is generally understood that a three-dimensional stress state exists at the free edge of a sample in tension for a dissimilar material interface, where debonding should occur first [100,101]. The free-edge stress state was computed using the finite element method with fine mesh around the free edge at the interface [95,101]. By incorporation with Z^N and Z^S obtained from the indentation test, the critical uniaxial tensile stress for crack initiation was calculated, and compared to the result of the tensile test. As shown in Fig.2-19, the predicted critical tensile stress was in good agreement with the experimental value.

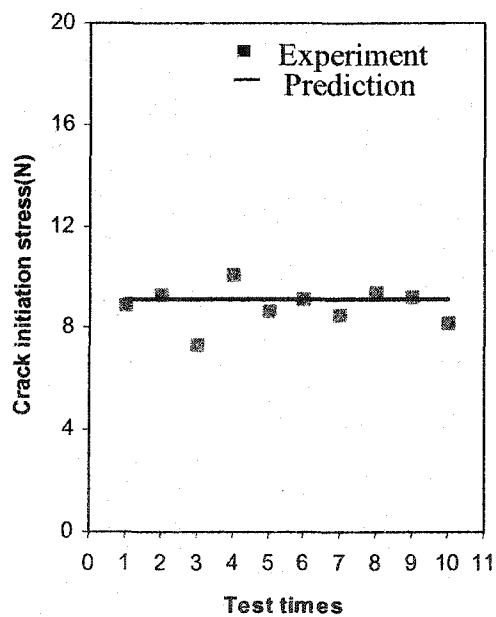


Fig.2-19. Comparison of experimental results of the tension test with a predicted bond strength obtained based on the force-sensing indentation test.

2.7 Conclusions

A lateral force-sensing indentation method is proposed to determine the interfacial bond strength for composites, thin films or coatings. The indentation is applied on the cross-section near an interface and the critical indentation load at initiation of interfacial debonding is determined by monitoring changes in sign of the slope of the lateral force-time curve. Indentation tests were performed for different interfacial bond strengths. Results of the tests demonstrated that this method was very sensitive to interfacial debonding. Computer modeling was performed to further justify the method and to investigate the mechanisms involved. The stress distribution at the interface corresponding to the critical load at debonding was analyzed using FEM and results showed that the interface was in a multiaxial stress state. In order to quantitatively determine the interfacial bond strength using the microindentation method, a computational method is proposed. This method allows the determination of the interfacial bond strength based on the critical indentation load, the Quadratic Delamination Criterion (QDC) and interfacial stress analysis using FEM. Tension tests were performed to evaluate an interfacial bond and results of the tests were compared to the bond strength determined using the lateral force-sensing indentation test. Good agreement between the results obtained respectively using the indentation method and the tension test was found.

Chapter 3

A finite element study of interfacial failure mechanism and parametric influence on the lateral force-sensing indentation method

In Chapter 2, the development of a lateral force-sensing indentation method to evaluate interfacial bond strength for composite materials and coatings was reported. When interfacial debonding occurs under a critical indentation load, the corresponding lateral force changes its direction, resulting in a change in the slope sign of the lateral force~time curve. Although previous studies have experimentally and theoretically confirmed interfacial debonding caused by microindentation, the interfacial failure under indentation condition and mechanisms involved have not been fully understood. The objective of this chapter is to obtain in-depth understanding of interfacial debonding processes under different conditions. Cu-ceramic and Al-ceramic bonds were studied, which may represent deformation and interfacial debonding of some typical engineering materials. The effects of indentation position and interfacial bond strength on the sensitivity of the lateral force response to debonding for detection of crack initiation at interface were also investigated.

Since it is difficult to conduct such research using an experimental approach, computational studies were conducted using the finite element method (FEM), an efficient tool for stress analysis and particularly suitable for studying interfacial failure processes [102~108]. There are usually two different methods to model the interface. One method treats an interface between two dissimilar materials as a distinct layer with a certain thickness and mechanical properties that are different from those of the adjacent materials, which form the interface [102~104]; while the other only takes account of the interfacial bond strength but ignores the interfacial thickness [105~108]. The later approach is preferred in the present study because properties of an interfacial layer are

not easily determined. Interfacial debonding could be evaluated using the energy release rate [109], local strain [110] or local stress [111~113]. In the present work, we have adopted the local stress approach, which is most widely used in studies on interfacial phenomena.

3.1 Construction of simulation model

3.1.1 Finite element modeling

A three-dimensional indentation process involving an elastic spherical indenter (e.g. diamond) applied to a soft elastic-plastic phase (e.g., a metal) that was bonded with a hard elastic phase (e.g., ceramic) was modeled using a finite element model. Al 6061-ceramic bond and Cu-ceramic bond were chosen for the study and material properties are listed in Table 3-1 and Fig. 3-1. Selection of Cu and Al alloy 6061 was based on the fact that the materials were typical engineering materials and are often used as matrix materials for composites. Young's modulus of the hard phase was chosen as 600 GPa, which was typical for ceramic materials. In all cases, a spherical indenter having a radius of 100 μm with its Young's modulus equal to 1000 GPa was used.

Table 3-1. Mechanical properties of materials.

Material	E(GPa)	ν	σ_y (MPa)	K(MPa)	n
Indenter	1000	0.16	—	—	—
Ceramic	600	0.2	—	—	—
Annealed Cu	110	0.34	33.3	315	0.54
Al 6061-T6	69	0.33	350	410	0.05

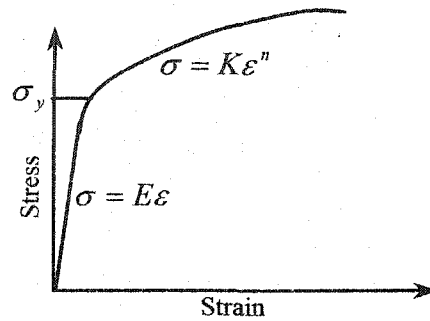
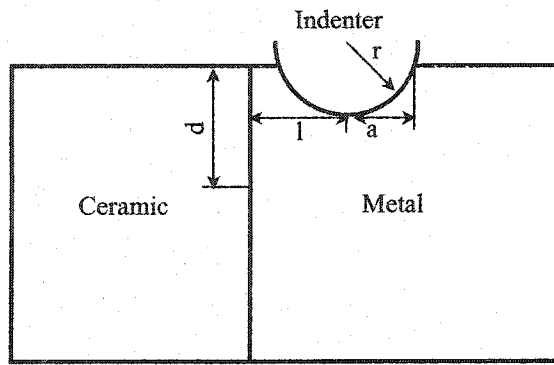
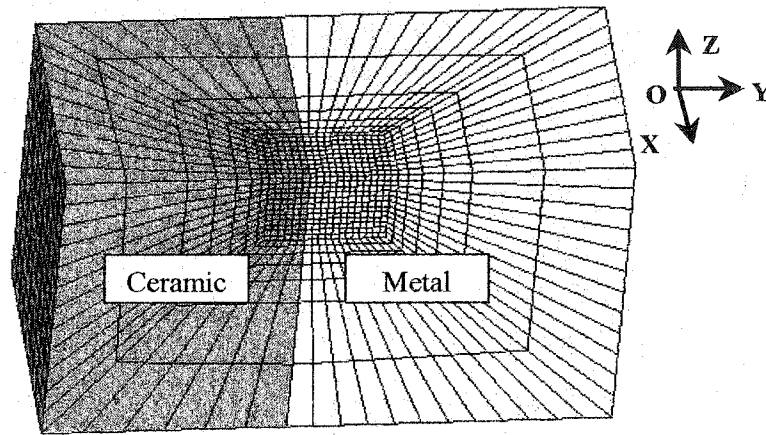


Fig. 3-1 An illustrated stress~strain curve of an elastic-plastic material.

The analysis was made using commercial finite element software ANSYS 7.0. In order to reduce the CPU time, only a half of the whole system was modeled, due to the mirror symmetry. Fig. 3-2 illustrates the system and the mesh used for the simulation. The region for indentation was discretized and mapped with fine mesh, which became progressively coarser when away from the indenter to ensure sufficiently accuracy and reduced computing time. The size of a simulated sample was sufficient large to eliminate the effect of boundary conditions on interfacial debonding. Before interfacial failure occurred, the interface was assumed to be perfectly bonded, i. e, the displacements at the interface were continuous. The interfacial constraint was satisfied by using common nodes which belong to elements on both sides. The simulated system had free side boundaries with its bottom fixed. Indentation at different locations, normalized with respect to the indenter radius, was chosen. Surface-to-surface contact between indenter and sample was employed with negligible friction.



(a)



(b)

Fig. 3-2 Illustration of (a) a system and (b) corresponding mesh for the FEM simulation.

3.1.2 Interfacial failure criterion

With an increase in the penetration depth of the indenter, cracks occurred at the interface, when the stress was sufficiently large to break the interface bond. In order to predict the onset of a crack, an interfacial failure criterion is necessary. In this study, the commonly used Quadratic Delamination Criterion (QDC) [95] was adopted to predict the initiation

of interfacial failure. This criterion has shown good agreement with experimental observations [95], and has the following form:

$$\frac{(\sigma_{xz})^2 + (\sigma_{yz})^2}{(Z^s)^2} + \frac{(\sigma_{zz})^2}{(Z^N)^2} \geq 1 \quad (3.1)$$

where σ_{xz} and σ_{yz} are interfacial shear stresses; σ_{zz} is interfacial normal stress; Z^N and Z^S are interfacial normal and shear strengths. It is assumed that when the QDC is satisfied at the interface, an interfacial crack initiates and propagates. In this case, an interfacial node is split into two nodes that respectively belong to the two sides of the interface and the crack-tip will subsequently move to the next node.

3.1.3 Interfacial crack growth

The interfacial debonding and lateral force response to indentation were simulated based on a flow chart shown in Fig. 3-3. The indentation load increased at a rate of 0.3N/min and the calculation was iterated up to 30 steps. The occurrence of interfacial cracking was checked during each iteration based on the QDC, and the total lateral force on the indenter was recorded. If no failure was determined at any interfacial node, the indentation load was then increased to the next step. Otherwise, interfacial cracking was introduced and the node at the position would be split into two nodes respectively belonging to two adjacent materials that formed the interface. The crack-tip subsequently moved to the next node and the crack thus propagated. The corresponding lateral force was also determined. The calculation was repeated in this manner until the maximum indentation load was reached.

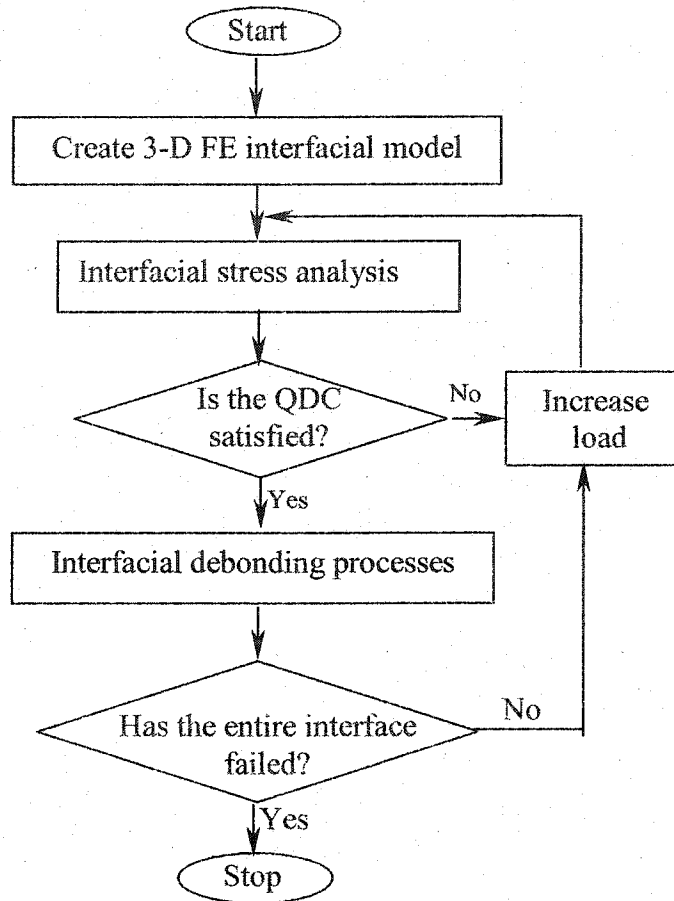


Fig. 3-3 A flow chart for modeling interfacial failure.

3.1.4 Verification of the finite element model

In order to investigate the interfacial failure mechanism, the FEM model needs to be verified. However, an accurate analytical solution of the stress distribution in the vicinity of the interface is not available, and experimental measurement also encounters some difficulties. Therefore, considering that the stress distribution for elastic material under an spherical indentation has been derived analytically [114], we used the model to calculate the indentation-stress field with an assumption that the materials that form the interface

are elastic and have the same mechanical properties as the ceramic phase. The analytical solution from the elastic model was compared to that obtained from the FEM analysis (Fig. 3-4). It can be seen that compressive stress σ_{zz} at interface had the maximum value $0.37p^*$ ($P^* = \frac{F}{\pi R^2}$, r -radius of the contact area; F -contact force) at position $d/a=0.6$ with the indentation distance $l/a=1$. The difference between the FEM result and corresponding analytical one was found to be negligible. It may thus be concluded that the finite element model is acceptable for modeling the microindentation processes under study.

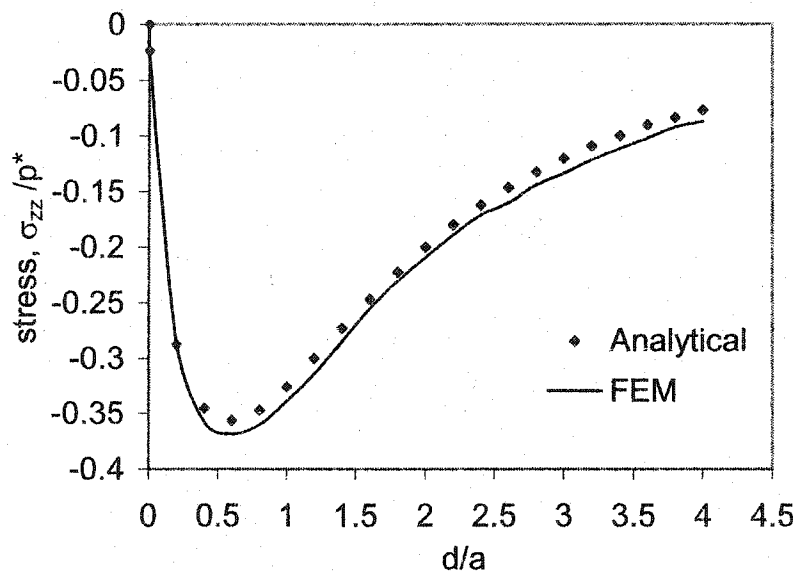


Fig. 3-4 Comparison between numerical results of the FEM model study on a perfect elastic body and corresponding analytical solution obtained based on the Hertz contact theory.

3.2 Results and discussion

3.2.1 Deformation geometry and stress distribution for homogeneous materials.

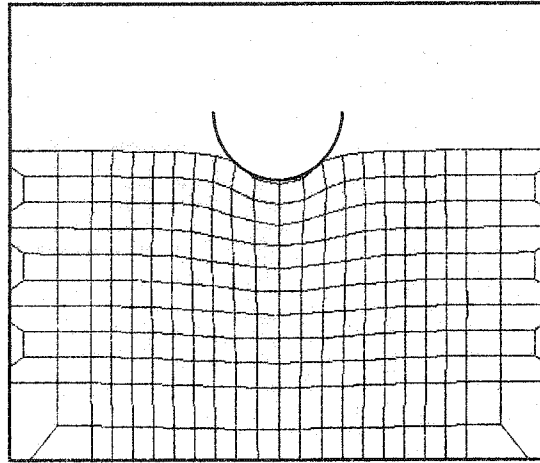
Before conducting the interfacial debonding analysis, it is instructive to look at the deformation and stress distribution caused by indentation for homogeneous materials. Fig. 3-5 shows deformations of annealed Cu and Al alloy materials under an indenter. It is noticed that sink-in occurs around the indenter for Cu material, but pile-up is produced for the Al alloy material.

When indentation is applied to a material, either pile-up or sink-in would occur, depending on its mechanical behavior [115~117]. The extent of pile-up or sink-in around a spherical indenter can be determined from the equation [116,117]:

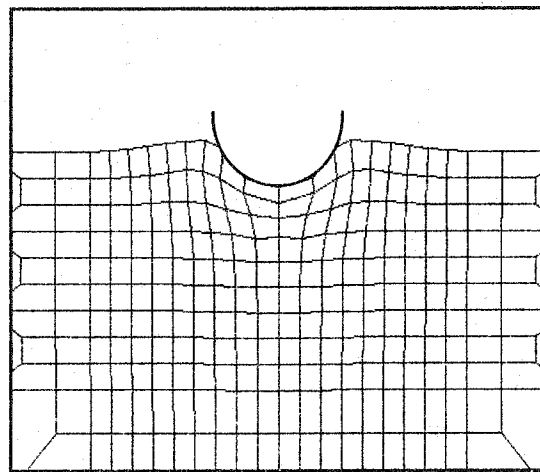
$$c^2 = \frac{5}{2} \left(\frac{2-n}{4+n} \right) \quad (3.2)$$

where n is the work-hardening exponent of the material. When c is greater than one, corresponding to a relatively ductile material, pile-up occurs; when c is smaller than one, sink-in would occur around an indenter.

The difference in deformation behavior between Al alloy and Cu depends on their work-hardening exponent n and the indentation position. The annealed Cu has its work-hardening exponent n equal to 0.54, corresponding to a c that is less than 1. Therefore, sink-in is expected to occur in Cu. The situation is different for the Al alloy, whose work-hardening exponent n is equal to 0.05 and corresponding c is 1.1. As a result, pile-up occurs in the Al alloy.



(a)

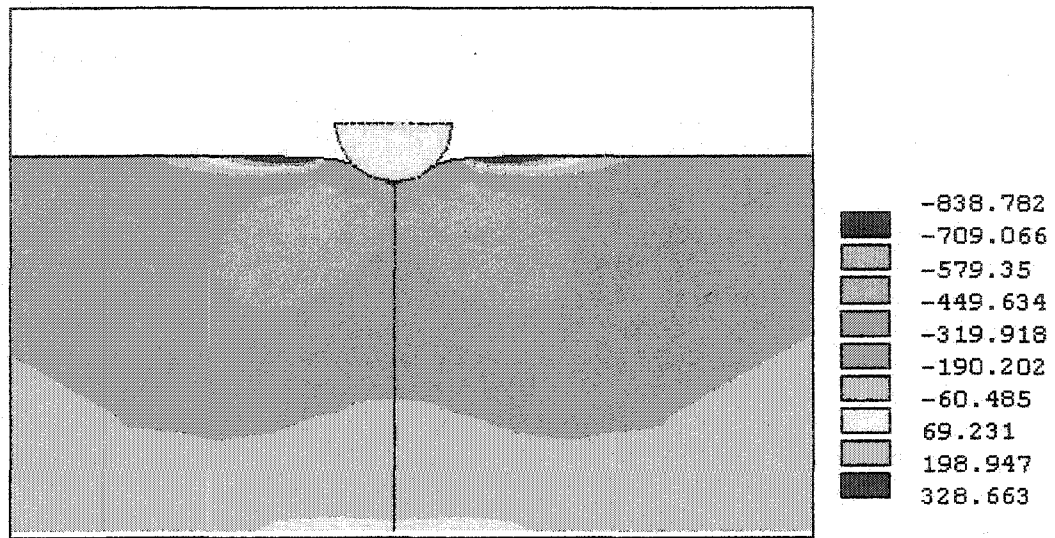


(b)

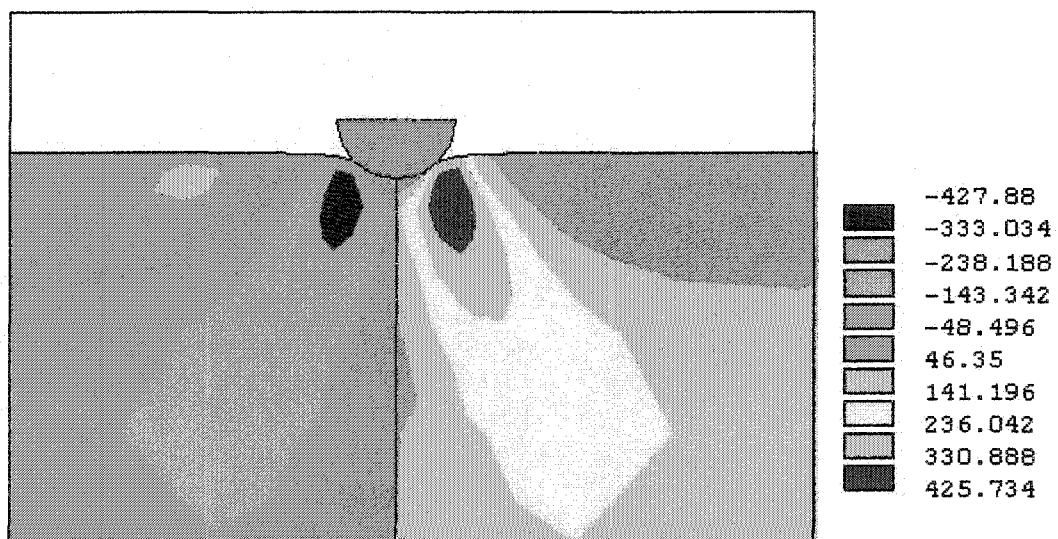
Fig. 3-5 Deformation geometries of different materials under an indenter tip: (a) Cu material, and (b) Al alloy.

The normal and shear stress distributions for the annealed Cu and Al alloy around the indenter are also different as shown in Fig. 3-6 and 3-7, respectively. For the annealed Cu

material, the maximum tensile stress occurred at the sample surface around the indenter, and the stress became compressive below the surface. However, for the Al alloy material, compressive stress existed at the sample surface and subsurface. The shear stress was also symmetric around the indenter but the maximum value was below the surface for both materials. The shear stress at the surface around the indenter had opposite values for the materials but their shear stress distributions are similar below the surface. The different stress distributions were related to different deformation behavior of the materials. Indentation produced compressive normal stress and upward shear stress at the surface for pile-up deformation, while tensile normal stress and downward shear stress result at the surface for sink-in deformation.

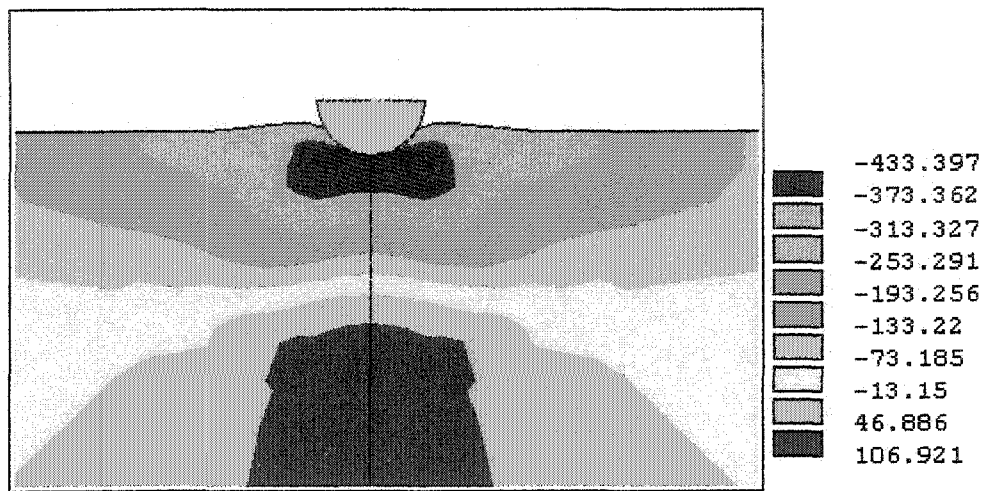


(a)

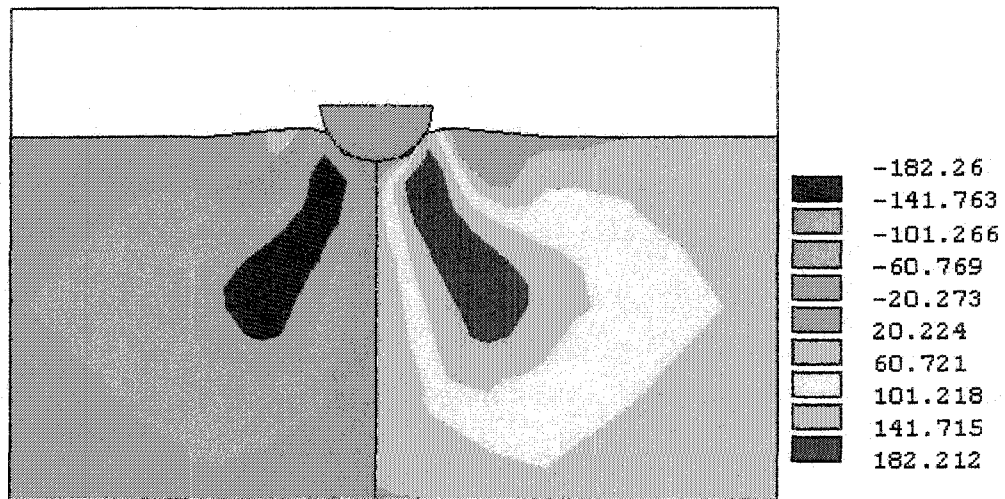


(b)

Fig. 3-6 Stress distribution caused by indentation in Cu material. (a) normal stress, and (b) shear stress.



(a)



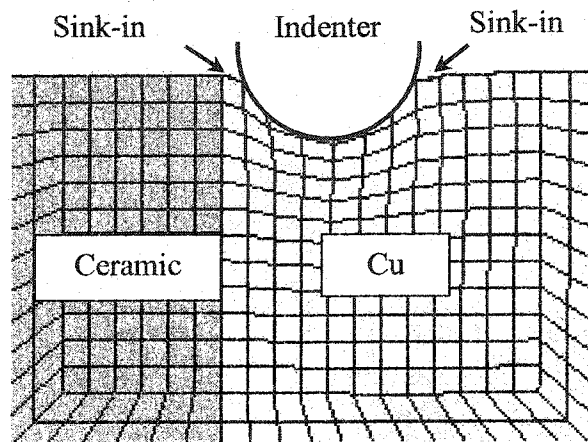
(b)

Fig. 3-7. Stress distribution caused by indentation in the Al alloy: (a) normal stress, and (b) shear stress.

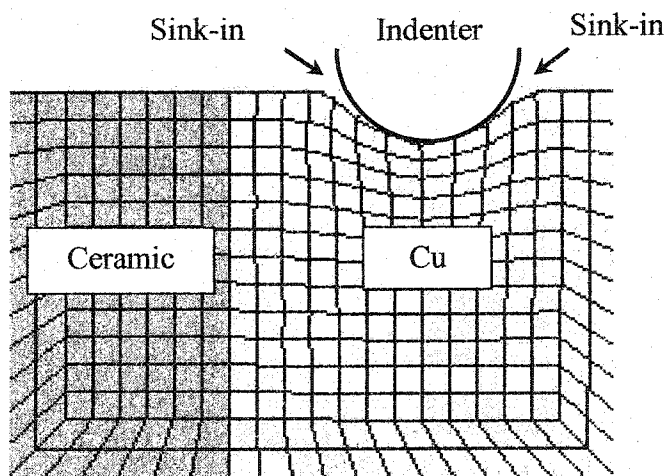
3.2.2 Deformation near an interface under indentation condition

Fig. 3-8 and 3-9 show deformations around Cu-ceramic and Al-ceramic bonds when indentation was applied at two different positions, respectively. It was observed that the two interfaces behaved differently during indentation. Sink-in was produced for Cu around the indenter at two different positions with their ratios $l/r=1.0$ and $l/r=1.8$ (Fig.3-8 (a) and (b)), respectively. However, for the Al-ceramic bond, there was no sink-in but pile-up that occurred around the indenter when indentation was applied at $d/r=1.8$ (Fig. 3-9(b)); when indentation was applied very close to the interface, sink-in occurred as shown in Fig. 3-9(a).

When indentation was applied near the interface, the ceramic phase constrained the Cu or Al phase, which resulted in asymmetric deformation at two sides of the indenter. For Cu, it did not influence the deformation trend, i.e. sink-in occurred at the both sides of the indenter for two different indentation positions; For Al alloy material, when indentation was applied at $l/r=1.8$ as shown in Fig. 3-9(b), pile-up occurred as expected. However, when indentation was applied near the interface, the constraint from the ceramic phase increased, which influenced the plastic deformation of Al alloy near the interface. Such influence led to sink-in near the interface while pile-up still occurred at the other side of the indenter as shown in Fig. 3-9(a).

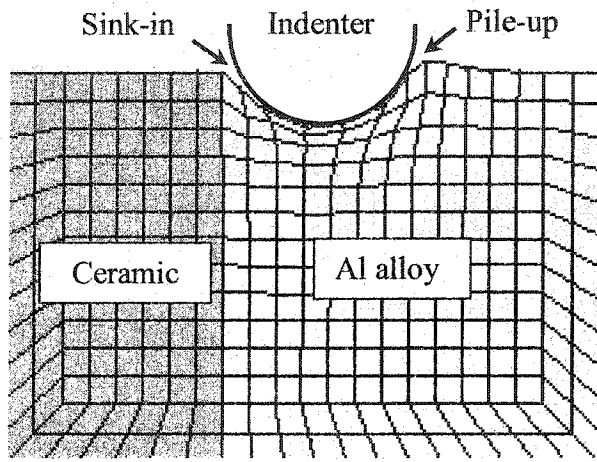


(a)

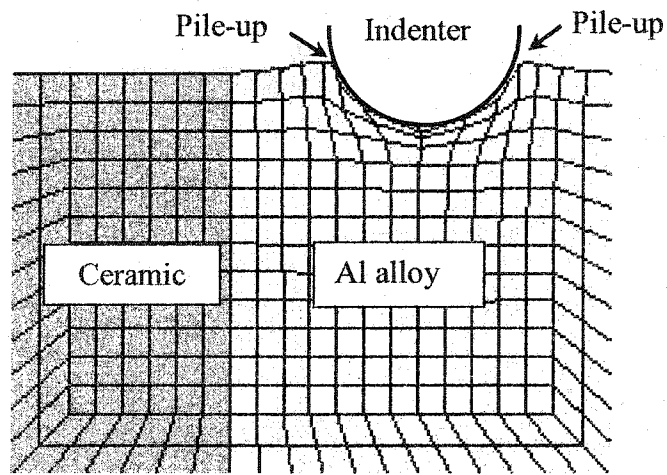


(b)

Fig. 3-8 Deformation of Cu near a Cu-Ceramic interface at different indentation positions, (a) $l/r=1.0$ and (b) $l/r= 1.8$. The indentation depth is $50\mu\text{m}$.



(a)



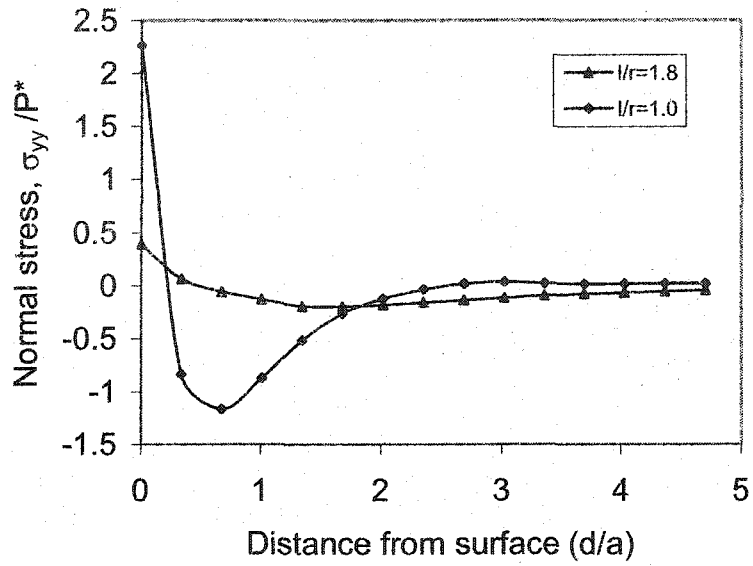
(b)

Fig. 3-9 Deformation of Al alloy near a Ceramic-Al alloy interface at different indentation positions, (a) $l/r=1.0$ and (b) $l/r=1.8$. The indentation depth is $50\mu\text{m}$.

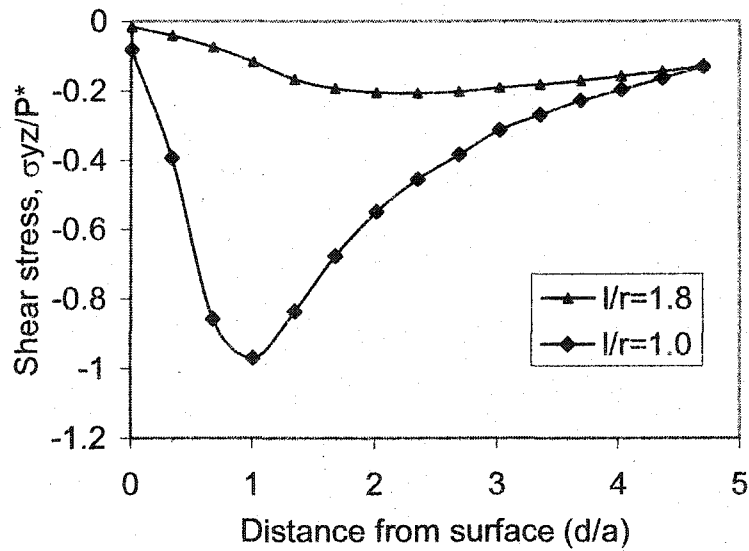
3.2.3 Stress distribution at interface

Sink-in and pile-up certainly correspond to different interfacial stress states and thus different mechanisms responsible for interfacial debonding. The distributions of normal and shear stresses at the interface along the mid-plane of the indenter for the two different bonds are shown in Fig. 3-10 and 3-11, respectively. The normal and shear stresses are normalized with respect to the normal contact pressure p^* .

It can be seen in Fig. 3-10(a) that the maximum interfacial tensile stress exists at the surface for the Cu-ceramic bond at positions of $l/r=1.0$ and $l/r=1.8$, respectively. The tensile stress decreases and changes to compressive stress with increasing distance d/a . Since a compressive normal stress does not contribute to delamination [118,119], it is not considered here for interfacial debonding. When the indentation is applied closer to the interface at position of $l/r=1.0$, larger tensile stress $\sigma_{yy}/P^*=2.26$ is produced, compared to $\sigma_{yy}/P^*=0.48$ at position of $l/r=1.8$. The shear stress has a similar trend as the tensile stress, that is, the magnitude of stress is larger at the position of $l/r=1.0$ than that at the position of $l/r=1.8$ (Fig. 3-10(b)). It is thus suggested that indentation should be applied closer to interface so that the interfacial debonding may occur more easily. It can also be seen that interfacial debonding is caused by a combination of tensile and shear stresses.



(a)



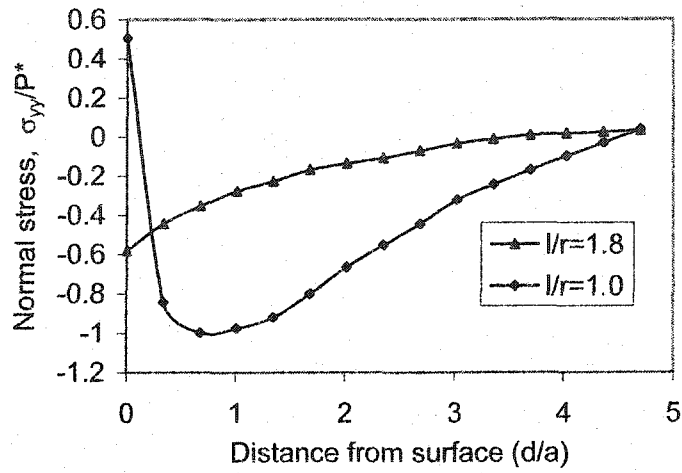
(b)

Fig. 3-10 Stress distributions at interface for Cu- Ceramic bond. Normalized (a) normal and (b) shear stresses.

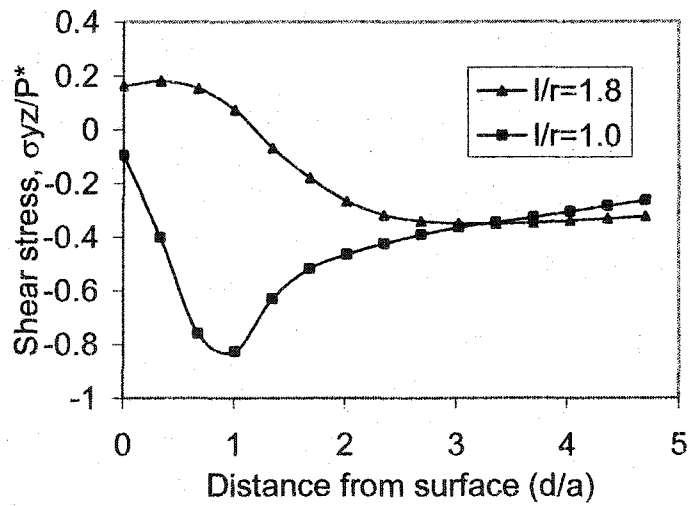
The stress distribution at the interface for the Al-ceramic bond is shown in Fig. 3-11. When the indentation is applied at a position of $l/r=1.8$, compressive stress exists along all the interface. Although the shear stress changes its sign at $d/a \approx 1.1$, it also contributes to the interfacial debonding. In this case, pile-up occurs near interface without the existence of interfacial tensile stress. The shear stress changes gradually to negative value with increasing d/a . When indentation is applied near an interface at a position of $l/r=1.0$, the distributions of normal and shear stresses are similar to those for the Cu-ceramic bond, so that interfacial debonding is caused by both tensile and shear stresses. In addition, it can be seen that the stress produced by indentation at position of $l/r=1.0$ is much larger than that at position of $l/r=1.8$. Therefore, indentation is preferred to be performed closer to interface.

Regarding the interfacial debonding position, it is determined not only by the stress, but also the interfacial bond strength (Z^N, Z^S) in equation (3.1). From the stress distribution for both the interfacial bonds under study, debonding may occur most likely at the sample surface with some probability to occur below the surface.

The stress distributions for the Cu-ceramic and Al-ceramic bonds correspond to different interfacial deformation modes as discussed earlier. It is understandable that "sink-in" corresponds to a maximum tensile stress at surface, but the normal stress at interface becomes negative because the indenter pushes material away when it moves deeper. Consequently, the shear stress magnitude increases with the indentation depth and reaches a maximum value as shown in Figs. 3-10 and 3-11. However, when the material



(a)



(b)

Fig. 3-11 Stress distributions at interface for Al alloy-Ceramic bond. (a) Normalized normal stresses (b) Normalized shear stresses.

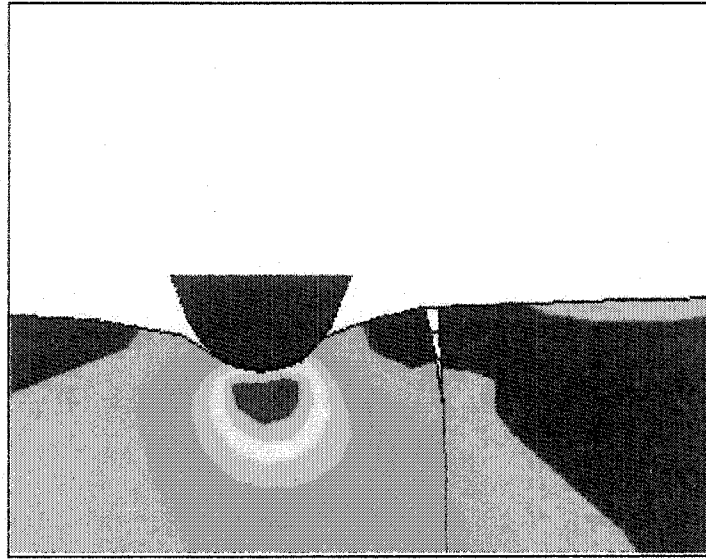
pile-up occurs, compressive stress exists at the sample surface, and the shear stress changes its direction with its magnitude reaching a maximum value beneath the surface. In the former case, interfacial debonding is caused by a combination of tensile and shear stresses; while in the latter case, the shear stress at the interface plays the major role in inducing interfacial debonding.

3.2.4 Interfacial debonding

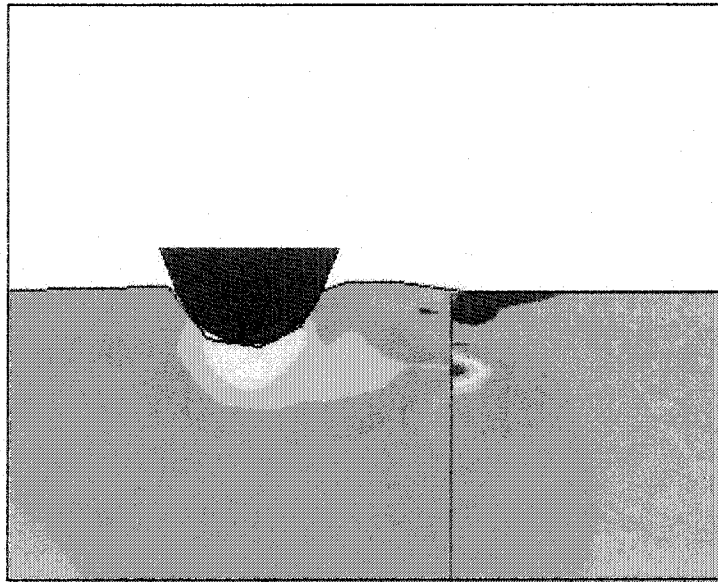
In order to evaluate the interfacial bond strength, the microindentation method should have the capability to (1) generate sufficiently large interfacial stress to cause interfacial debonding, and (2) to detect the interfacial debonding with high sensitivity. In the present studies, the influence of indentation load on the interfacial stress distribution, the interfacial debonding mechanism and the sensitivity of the microindentation technique were investigated. The sensitivity could be evaluated by the degree of change in the slope of the lateral force~time curve when interfacial debonding occurred.

3.2.4.1 Interfacial debonding mechanism

Fig. 3-12 shows different interfacial debonding mechanisms for ceramic/Cu and ceramic/Al bonds, respectively. When sink-in occurs in the material, there existed a crack opening at the interface, which is caused by the coupling of tensile and shear stresses. However, when pile-up occurs, the interfacial debonding is caused by the shear stress at the interface. It is also noticed that the stress concentration exists at the crack tip, which facilitates the crack propagation.



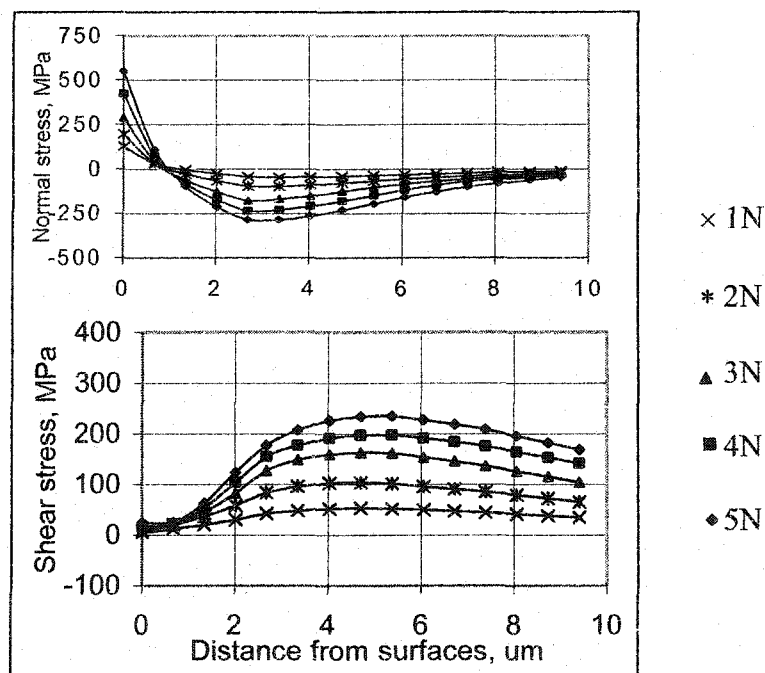
(a)



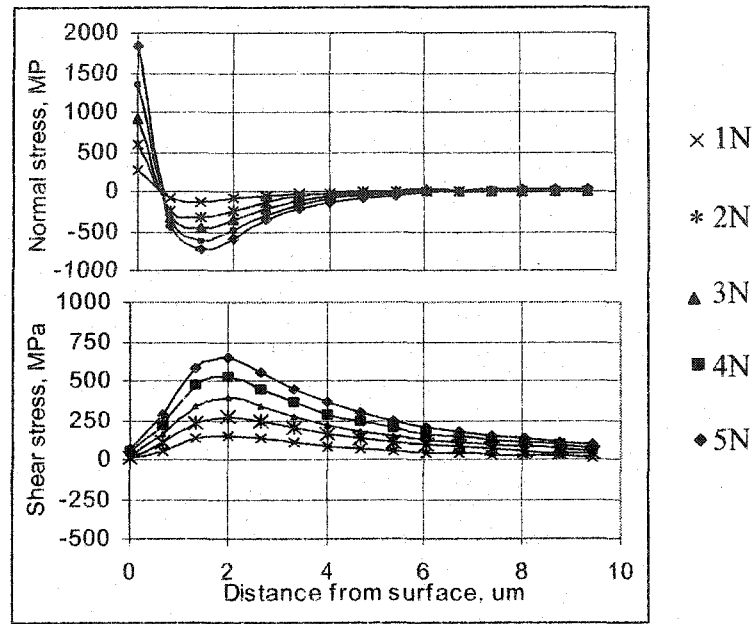
(b)

Fig. 3-12 Interfacial debonding processes. (a) ceramic/Cu bond, and (b) ceramic/ Al bond.

In order to examine the capability of indentation to cause interfacial debonding, the stress distribution at interface for different indentation loads was investigated. As an example, the ceramic/Cu bond at two different indentation positions of $l/r=1.0$ and $l/r=1.8$, respectively, was analyzed. As shown in Fig. 3-13, with the increase in the load, both the normal and shear stresses increase for two different indentation positions. Therefore, we can conclude that when the applied load reaches a certain value that produces a sufficiently large stress at interface, interfacial debonding occurs even though the failure mechanisms may differ.



(a)



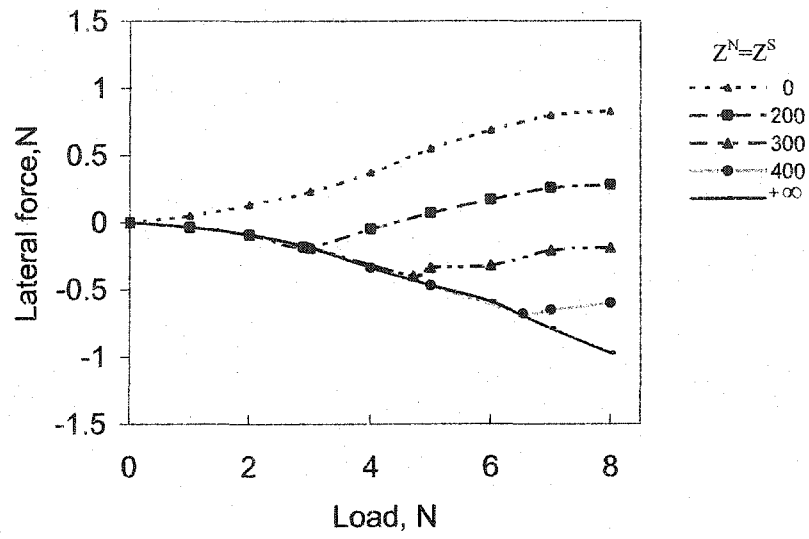
(b)

Fig. 3-13 Stress distribution along the interface for ceramic/Cu bond. (a) $l/r=1.8$, and (b) $l/r=1.0$, $r=2\mu\text{m}$,

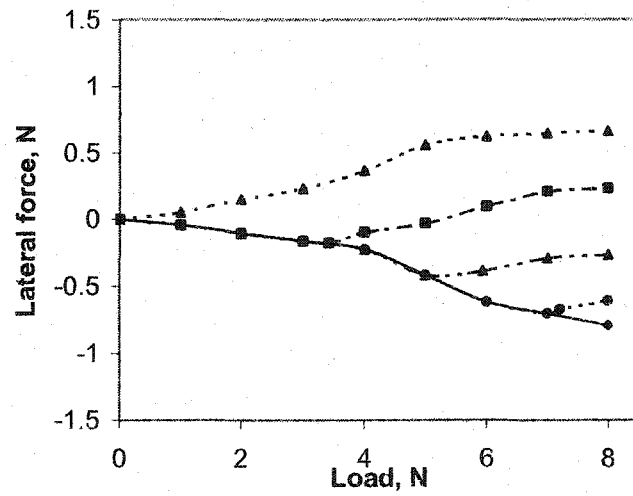
3.2.4.2 The sensitivity of lateral force response to interfacial debonding

Cu-ceramic and Al alloy-ceramic interfaces were investigated. The former is accompanied with “sink-in” and the later with “pile-up” when subjected to indentation. Different bond strengths were considered, ranging from no bonding to strong bonding. For a case study, we assumed $Z^N = Z^S$, i.e. the interfacial tensile strength was equal to the interfacial shear strength.

Fig. 3-14 illustrates the responses of lateral force to indentation for the Cu-ceramic bond and Al alloy-ceramic bond, respectively. For a strong bond, the lateral force keeps going down. That happens because the constraint of the interface to indenter is stronger than



(a)



(b)

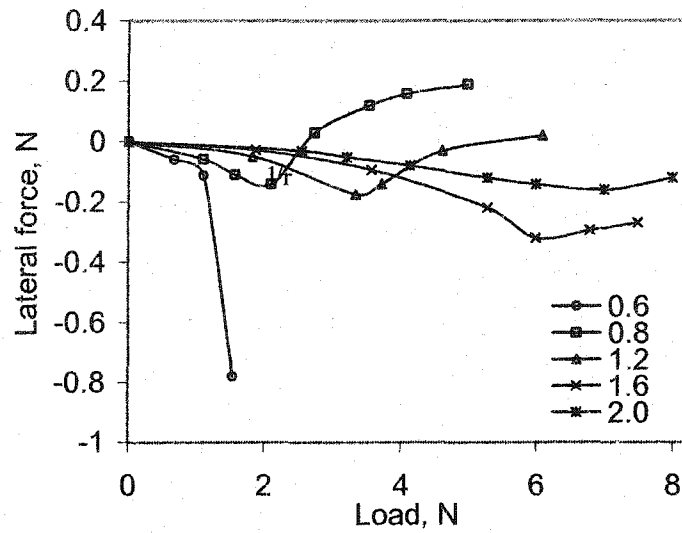
Fig. 3-14 Effects of interface bond strength on the lateral force response to indentation.

(a) Cu-ceramic bond. (b) Al alloy-ceramic bond. $l/r=1.0$.

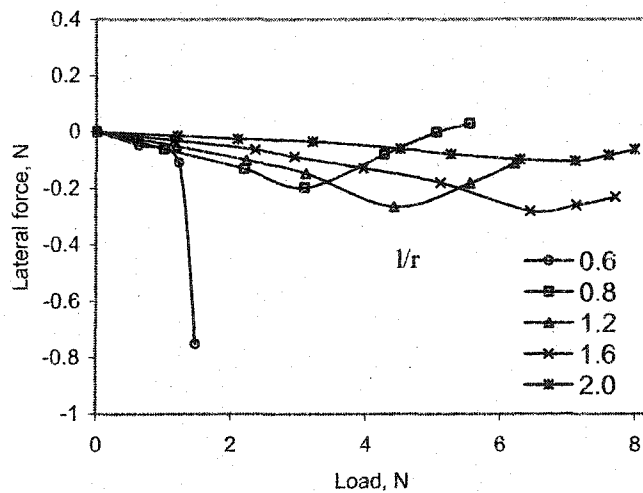
that at the other side of the indenter, so that the indenter keeps moving away from the interface. Such trend changes when the interfacial bond becomes weaker. In this case, a change in the slope sign of the lateral force~time curve occurs, corresponding to interfacial debonding. When the bond strength is zero, the lateral force keeps moving up, i.e. the indenter keeps moving towards the interface due to zero shear constraint from the interface. It is worth noting that the lateral force responses to indentation for both Cu-ceramic and Al alloy-ceramic interfaces are similar (Fig. 3-14(a) and (b)). This means that using the lateral force response to detect interfacial debonding is effective no matter whether debonding is caused by shear stress or the combination of tensile and shear stresses; the former plays the main role with the pile-up phenomenon while the latter with the “sink-in” phenomenon.

The sensitivity of the lateral force response to indentation is certainly influenced by the indentation location. Fig. 3-15 shows the lateral force response when indentation is performed at different positions, from $l/r=0.6$ to $l/r=2.0$ for both the Cu-ceramic and Al alloy-ceramic interfaces with an interfacial bond strength of $Z^N=Z^S=200\text{MPa}$. As shown, with an increase in the indentation distance from the interface, the magnitude of the lateral force at interfacial debonding becomes larger. This means that a larger indentation load is required for debonding. However, the corresponding change in the slope of the lateral force~time curve becomes smaller, that is, the lateral force response becomes less sensitive when indentation location is far away from the interface. Therefore, indentation should be performed to the interface as close as possible to the interface as long as the

indenter does not touch the interface. If the indenter touches the interface, the lateral force would move down dramatically, pushing the indenter away from the interface as illustrated in Fig. 3-15 for the case of $l/r=0.6$.



(a)



(b)

Fig. 3-15 Effects of indentation position on the lateral force response to indentation. (a) Cu-ceramic bond, and (b) Al alloy-ceramic bond. $Z^N=Z^S=200\text{MPa}$.

3.3 Conclusions

Interfacial debonding processes involving “sink-in” and “pile-up” phenomena were investigated using the finite element method. The interfacial stress associated with “sink-in” is quite different from that with “pile-up”, corresponding to two typical failure mechanisms. The FEM studies have led to the following conclusions:

- (1) For the Cu-ceramic bond, interfacial debonding is most likely caused by a combination of tensile and shear stresses when indentation is applied. In this case, material sink-in occurs around the indenter.
- (2) For the Al-ceramic bond, pile-up occurs around the indenter when indentation is applied far away from interface. Interfacial debonding is caused mainly by interfacial shear stress. However, when indentation is applied close to the interface, sink-in may occur around the indenter at the side near the interface and pile-up occurs at the other side. In this case, the interfacial debonding may result from a combination of tensile and shear stresses.
- (3) Lateral force responses of the Cu-ceramic and Al alloy-ceramic bonds to interfacial debonding have similar sensitivities. Or in other words, the lateral force-sensing microindentation method may have similar sensitivities to interfacial debonding for both the processes accompanied with “sink-in” and “pile-up” phenomena.

(4) Indentation is preferred to be performed close to an interface (without touching the interface), which can produce larger stress at interface and also a sharper change in the slope sign of the lateral force~time curve.

Chapter 4

Optimization of the indentation condition for determination of interfacial bond strength: A FEM study

In Chapters 2 and 3, the lateral force-sensing indentation method to evaluate the interfacial bond strength was introduced, and the interfacial failure mechanism as well as the sensitivity of lateral force response to interfacial debonding was also discussed. Logically, it is desirable to maximize the interfacial stress to facilitate interfacial debonding especially for very strong bonds. Material mechanical properties and indentation parameters have strong influences on the stress distribution at the interface. In order to provide guidelines for efficient application of this method, it is necessary to investigate different indentation conditions and identify optimum experimental parameters to maximize the interfacial stress. Furthermore, a larger interfacial stress introduced by indentation could make the slope of the lateral force-time curve change more sharply, thus increasing the sensitivity and accuracy of this technique.

The objectives of the research reported in this chapter are to investigate effects of the different parameters, including material properties, indenter geometry and indentation position, on interfacial debonding and to identify the optimum indentation condition. It is difficult to conduct such studies experimentally, as they require numerous tests for different interfaces and experimental parameters. Numerical simulation, however, could be an effective approach for such studies. In this work, the finite element method was adopted for interfacial stress analysis. We chose three interfaces, Al-ceramic, steel-ceramic and tool steel-ceramic, to represent typical interfaces: soft-hard, medium-hard and hard-hard bonds. The effects of indentation condition including indenter geometry and indentation position on indentation debonding were investigated. Particular efforts

were made to investigate the effects of material properties on the interfacial stress at the free edge caused by the mismatch in mechanical behavior between two bonded materials.

4.1. Statement of the problem and the FEM model

4.1.1 Factors that affect the interfacial stress

The interfacial stress distribution is affected by many factors. It is known that in general the maximum stress has high probability to exist at the free edge of an interface. A general form of the stress field near the free edge of an interface in ceramic-to-metal joint has been derived [120,121]:

$$\sigma_{ij}^{\text{int}} = \sigma \left(\frac{l}{H}\right)^{\omega} k_{ij} \quad (4.1)$$

where σ_{ij}^{int} is an interfacial stress component, l and H are dimensional parameters (see Fig.4-2 and 4-3), and k_{ij} is a constant depending on material properties. σ is the applied stress. The term $\left(\frac{l}{H}\right)^{\omega}$ is the singular part of the equation and ω is a singular exponent.

According to equation (4.1), if ω is negative, the term $\left(\frac{l}{H}\right)^{\omega}$ approaches infinity as l approaches zero and, therefore, a singular stress distribution would exist at the free edge of the interface. In this case, the interfacial stress σ_{ij} could be dominated by this factor at the free edge and cause interfacial debonding easily. The singular exponent ω is determined by the mismatch in mechanical properties between the two bonded materials. Therefore, it is necessary to explore the relationship between ω and material properties and thus determine the influence of material properties on interfacial stress.

When indentation is applied near an interface, the stress distribution around the indenter is complicated and it is difficult to determine the influence of material properties on interfacial stress directly by the singular exponent ω according to equation (4.1). Therefore, in this study a tensile test model was built, in which σ can be considered as a constant, to investigate the singularity and the corresponding interfacial stress. A commonly used method, nonlinear regression analysis [122] was adopted to derive the singular exponent ω for different interfacial bonds.

The factor σ in equation (4.1) is a measure of the applied stress, which is affected by the indenter geometry and indentation position as well as interfacial properties. An associated indentation model was proposed to investigate the influence of indentation parameters on interfacial debonding.

4.1.2 FEM model

The stress distributions at three different interfaces were analyzed using the finite element method. A two-dimensional model was developed to investigate the influence of indentation parameters on interfacial debonding. Although the 2-D model cannot completely represent a 3-D case, it more or less helps to gain some insight into the interfacial debonding under different indentation conditions [123]. The ceramics and metals under this study were assumed to possess linearly elastic and bilinear elastic-plastic properties (Fig. 4-1), respectively, and their mechanical properties are given in Table 4-1.

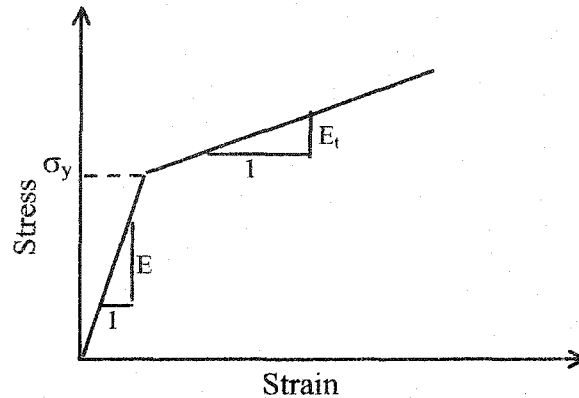


Fig. 4-1 The bilinear elastic-plastic behavior of materials used in the FEM analysis.

Table 4-1. Material properties

Materials	Young's Modulus E (GPa)	Poisson's ratio ν	Yield stress σ_y (MPa)	Tangential Modulus E_t (GPa)
Aluminum	69	0.30	280	1.5
Carbon steel	200	0.28	370	10
Tool steel	210	0.28	1800	50
Ceramic	400	0.25	---	---

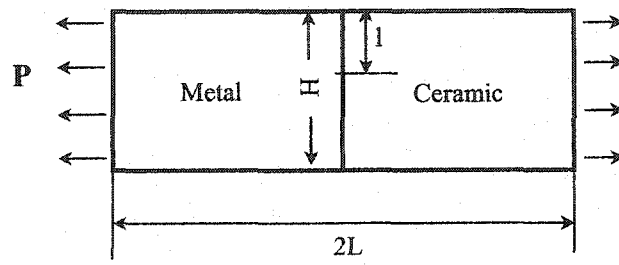
The modeling work involved two tasks: one was to investigate the influence of the mechanical properties of materials on the interface stress at the free edge by means of three different interfaces subjected to tension as shown in Fig. 4-2(a). The applied stress at two ends of the sample having an interface (Fig. 4-2) produced uniform stress near the interface and, thus, the stress σ in equation (4.1) is the same for three different interfaces, i.e. Al-ceramic, steel-ceramic and tool steel-ceramic interfaces. The influence of the applied stress could thus be excluded. Therefore, this model could be used to investigate the influence of the material properties, which is related to the effect of the

singular exponent ω on interfacial stress. The second task was to investigate interfacial debonding caused by indentation, as shown in Fig. 4-3(a). Three indenter shapes, circular, 90-degree and 136-degree between two opposite faces, with tip radius of $2\mu\text{m}$ were chosen for modeling and comparison. The indentation was applied at metal side at different distances from the interface (Fig.4-3). The loading conditions for both the tension and indentation cases were given in Table. 4-2.

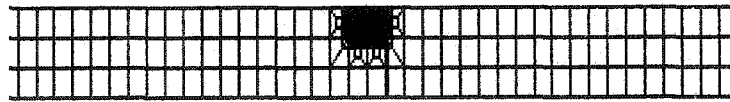
Table 4-2 Load and geometry parameters used for interfacial stress analysis.

Indentation test	Dimensions of the system (Fig.4-3)		
	Width	H	0.12mm
	Length	2L	0.24mm
	Tip radius	r_0	$2\mu\text{m}$
	Tip angle	θ	circular, 90-degree, 136-degree
	Distance from interface	d/r	1.2~15
	Load	P	6N
Tension	Dimension of the system (Fig.4-2)		
	Width	H	3mm
	Length	2L	40mm
	Applied tensile load	P	5N

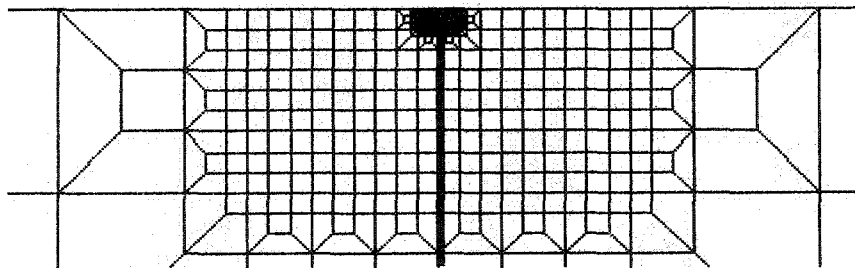
r-- is the radius of the contact area under a specific applied load.



(a)

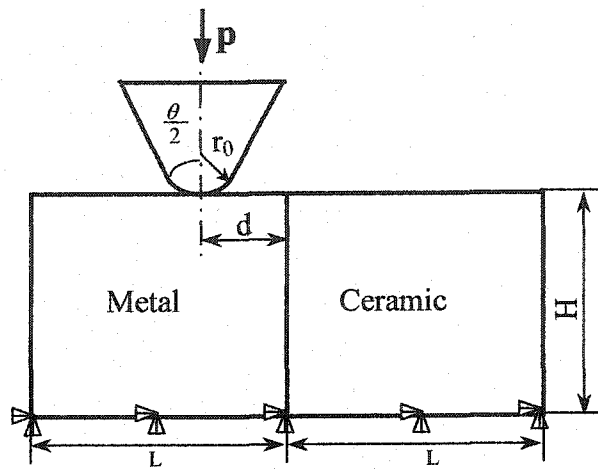


(b)

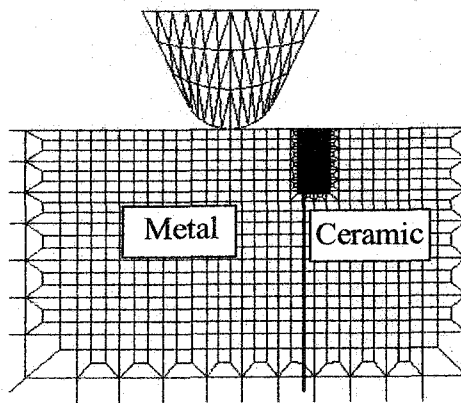


(c)

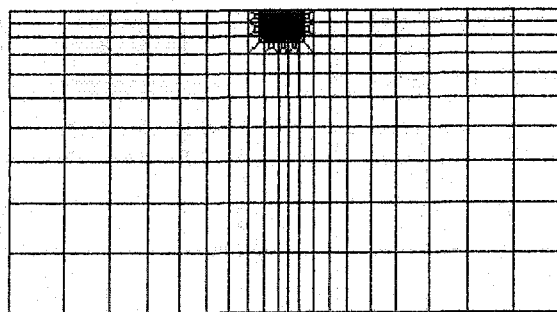
Fig.4-2 Tensile test: (a) geometry and boundary condition, (b) mesh of the system for FEM analysis, (c) a closer view of the mesh at the free edge.



(a)



(b)



(c)

Fig. 4-3 Indentation test: (a) geometry and boundary condition; (b) mesh of indentation model and (c) a closer view of the mesh at the interface.

In the modeling study, we treated the indenter tip as a rigid body. A perfect bond was assumed at the interface between the two materials, i.e. displacements across the interface were continuous:

$$\begin{aligned}\mu^1(x, y) &= \mu^2(x, y) \\ \nu^1(x, y) &= \nu^2(x, y)\end{aligned}\tag{4.2}$$

where the superscripts 1 and 2 present two different materials, respectively. μ and ν are the displacement components that are respectively vertical and parallel to the interface. These interface constraints were satisfied by using common nodes which belong to elements at both sides of the interface. The finite element mesh consisting of 4-node quadrilateral elements was used for stress analysis. Finer mesh was set at the interface, which became progressively coarser with an increase in the distance from the interface, as shown in Fig. 4-2(b) and Fig. 4-3(b), to ensure sufficient accuracy for the stress analysis.

4.2 Results and Discussion

4.2.1 Influences of material properties on the interfacial singularity

In order to investigate the influence of material properties (Table 4-1) on interfacial debonding, the interfacial stresses in the vicinity of the free edges of the three different interfaces subjected to remote uniform tensile stress were calculated and the results are shown in Fig. 4-4. σ is the applied tensile stress and σ^{int} is the interfacial tensile stress near the free edge. Fig. 4-4 indicates that the interfacial stress far from the free edge is close to the applied stress σ for all the three interfaces. However, σ^{int} approaches infinity

when l/H is close to zero, showing a singularity at the free edge. The Al-ceramic bond has the largest increase in stress at the free edge, while the tool steel-ceramic bond has little change at the free edge. A non-linear regression analysis was conducted, in conjunction with Equation (4.1), to investigate the relationship between interfacial stresses σ^{int} and the singular exponent ω , which was dependent on material properties. The results obtained by best-fitting the calculated stress with Equation (4.1) for three different interfaces are as follows:

$$\begin{aligned}
 \text{Ceramic-Al:} & \quad \omega = -0.188 \\
 \text{Ceramic-steel:} & \quad \omega = -0.11 \\
 \text{Ceramic-tool steel:} & \quad \omega = -0.014
 \end{aligned}
 \tag{4.3}$$

In the regression analysis, the correlation coefficient is above 0.95.

It was demonstrated that the Al-Ceramic bond showed large singularity ($\omega = -0.188$) existing at the free edge of the interface due to the large mismatch in mechanical behavior between two dissimilar materials. This means that the term $(\frac{l}{H})^{-0.188}$ becomes very large when l approaches zero. Therefore, the interfacial stress σ_{ij}^{int} is mainly determined by this singular term and very high stress exists at the free edge to initiate interfacial debonding. The strong singularity and resultant stress concentration at the free edge facilitate the interfacial debonding, especially for very strong bonds. For the steel-ceramic bond, its singularity at the free edge is $\omega = -0.11$. Therefore, the stress concentration at the free edge of the steel-ceramic interface is smaller than that of the ceramic-Al bond. For the tool steel-ceramic bond, its $\omega = -0.014$ is very small so that the corresponding singularity

could be ignored and thus the interfacial debonding would be caused basically by the applied load. Therefore, the soft-hard and medium-hard interfaces have stronger singularity at the free edge, which is beneficial to the interfacial debonding, compared to the hard-hard interface.

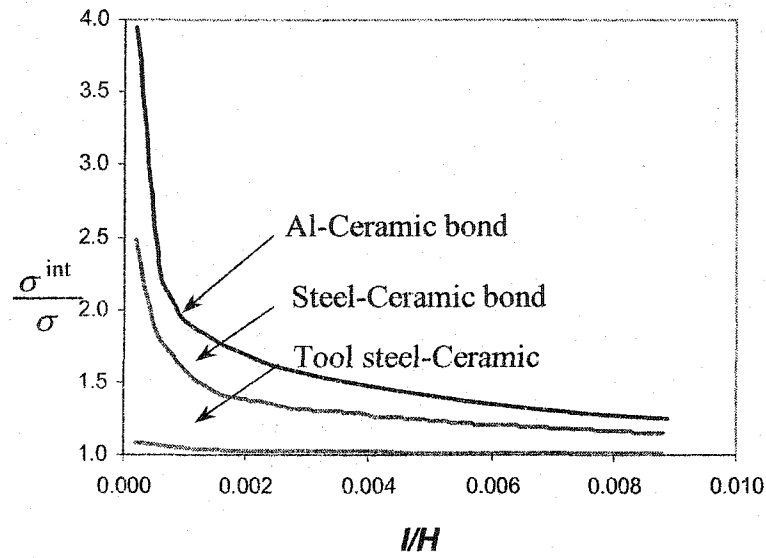


Fig. 4-4 Interfacial stresses with respect to l/H for different interfacial bonds under applied tensile stress.

Because of the singularity, it is difficult to calculate stress at the interfacial free edge. A method has been proposed to calculate the average stress within a small distance from the free edge of an interface [119,120,124] as follows:

$$\sigma_{ij}^{int}(l) = \frac{1}{l^*/H} \int_0^{l^*/H} \sigma_{ij}^{int}(l) d(l/H) \quad (4.4)$$

where l^* is a distance from the free edge along an interface. The stresses $\sigma_{ij}^{int}(l)$ is an average interfacial stress at free edge over a relative length of $l^*/H=0.001$ [119].

4.2.2 Influences of indentation parameters on interfacial debonding

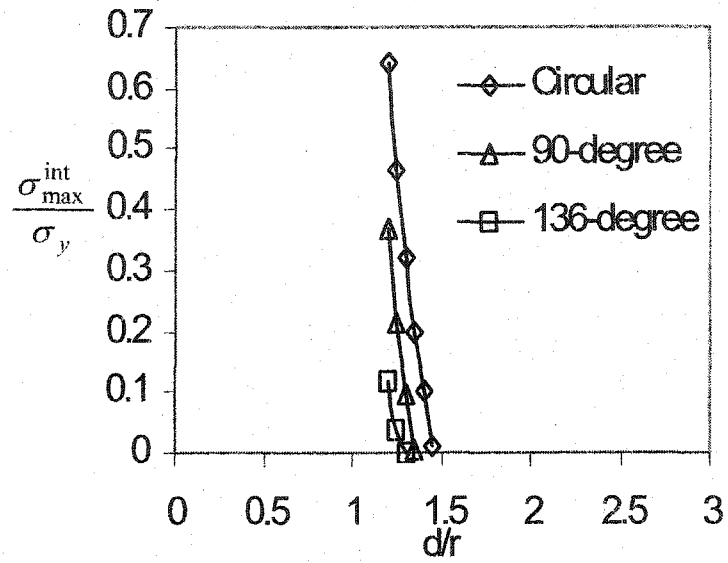
As mentioned earlier, it is always desirable to maximize the stress at the interface to facilitate interfacial debonding. In addition to the influence of material properties on interfacial singularity and thus the interfacial stress, the indenter geometry and indentation position also affect the interfacial stress. To optimize the indentation condition, the maximum normal stress $\sigma_{\max}^{\text{int}}$ and shear stress τ_{\max}^{int} produced at the interface with respect to different indentation positions and indenter geometries for three different interfaces are shown in Fig. 4-5 ~ 4-7 for comparison. d/r is a ratio used to represent the indentation position, where r is the radius of the contact area between indenter and sample under an applied load of 6N. $\sigma_{\max}^{\text{int}}$ and τ_{\max}^{int} are normalized with respect to the yield stress.

According to the FEM analysis, as indentation is applied near an interface, the normal stress can be either tensile or compressive, depending on the indentation position and material properties. It has been suggested that interfacial compressive normal stress does not contribute to delamination [125,126]. Therefore, only tensile and shear stresses at interface were considered here to cause interfacial debonding.

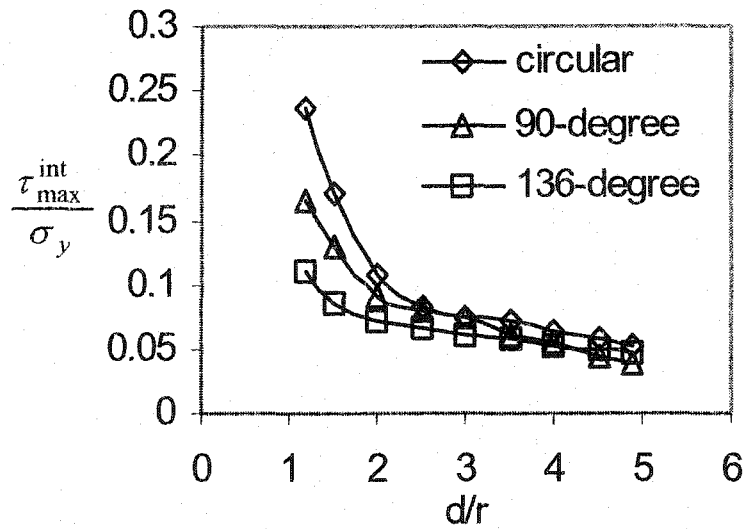
According to the Quadratic Delamination Criterion, interfacial debonding is caused by the coupling of normal and shear stresses. Interfacial debonding is, therefore, judged by the combined effect of tensile stress and shear stress at interface. As shown in Fig. 4-5 ~ 4-7, in which the compressive stress with the negative sign is not given, when the

indentation position is closer to an interface, both $\sigma_{\max}^{\text{int}}$ and τ_{\max}^{int} increase for all the three typical interfaces. Thus, for an interface with larger tensile or shear strength, indentation near the interface is preferred, which may cause onset of interfacial debonding easily.

Regarding the influence of indenter geometry on interfacial stress, for an Al-ceramic bond, it was demonstrated that the circular indenter produced the largest $\sigma_{\max}^{\text{int}}$ and τ_{\max}^{int} at the interface. The 90-degree indenter resulted in smaller $\sigma_{\max}^{\text{int}}$ and τ_{\max}^{int} , while the 136-degree indenter produced the smallest stresses as shown in Fig. 4-5. When indentation is applied, the material around the indenter can be sink-in or pile-up, depending on material properties and indentation situation [115]. The sink-in produces a tensile stress around the indenter, while the pile-up produces the compressive stress around the indenter. Since a soft material may “sink-in” when the indentation is very close to the interface and “pile-up” when indentation position is away from the interface, the tensile stress only existed when d/r is small. Therefore, the distance between the interface and indenter should be within a limited range in order to have tensile interfacial stress, e.g., $(d/r)=1\sim 1.5$ for the circular indenter, $1\sim 1.32$ for the 90-degree indenter and $1\sim 1.3$ for the 136-degree indenter, respectively, as indicated by the FEM analysis.



(a)



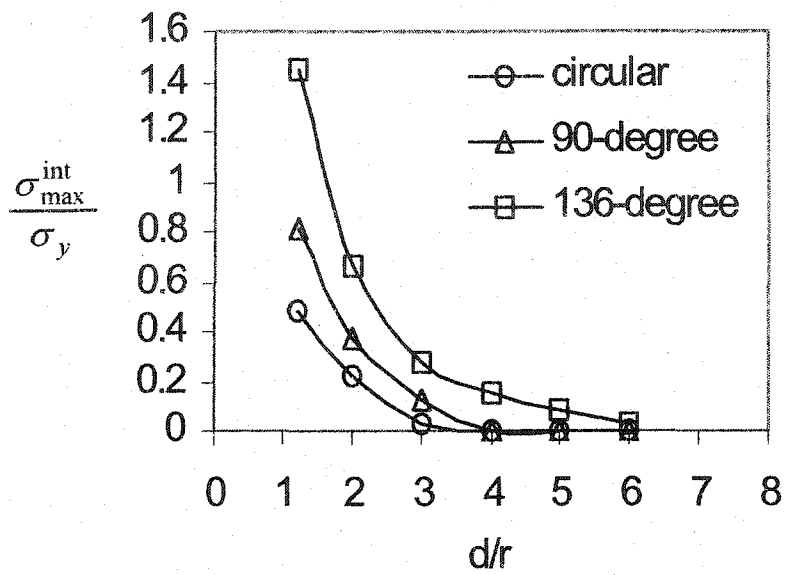
(b)

Fig. 4-5 The influence of indenter geometry and indentation position on the maximum (a) tensile stress and (b) shear stress for the Al-Ceramic bond.

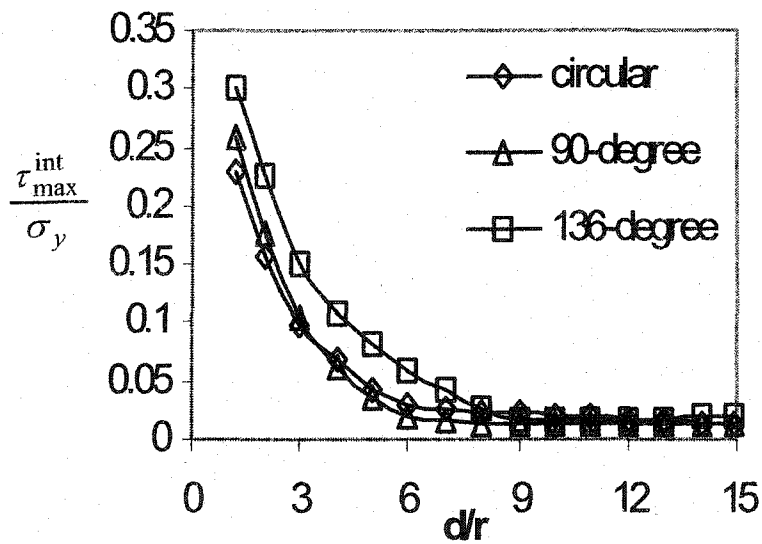
For the steel-ceramic bond, the situation changed. As demonstrated, the 136-degree indenter caused the largest $\sigma_{\max}^{\text{int}}$ and τ_{\max}^{int} , while the circular indenter had the smallest $\sigma_{\max}^{\text{int}}$ and τ_{\max}^{int} , as shown in Fig. 4-6. For the same reason, as discussed earlier, the tensile stress only existed when indentation was performed close to the interface. However, the distance between the interface and indenter, within which tensile stress existed, was much larger than that for the Al-ceramic bond. The preferred ratio (d/r) was 1~6.3 for 136-degree indenter, 1~4.5 for 90-degree indenter and 1~3.7 for the circular indenter.

For the tool steel-ceramic bond, the FEM analysis demonstrated that the three indenters produced almost the same $\sigma_{\max}^{\text{int}}$ and τ_{\max}^{int} (Fig. 4-8). This happened because the tool steel was very hard and resultant deformation was small. The indentation contact area was limited to a very small area. Different from the Al-ceramic bond and steel-ceramic bond, no pile-up but sink-in occurred in the tool steel. As a result, only tensile stresses existed in the entire indentation region.

From the above analysis, guidelines for lateral-force sensing indentation method to evaluate interfacial bond strength, which has difficulty to be performed experimentally, could be established based on FEM analysis. In order to achieve the maximum interfacial stress, indentation closer to the interface is preferred for all the three different interfaces. Regarding the effect of indenter shape on the interfacial stress, the circular indenter could produce the largest stress at interface for the soft-hard interface, while the 136-degree indenter would be the best for the medium-hard interface. However, the indentation geometry had little influence on the hard-hard interface.

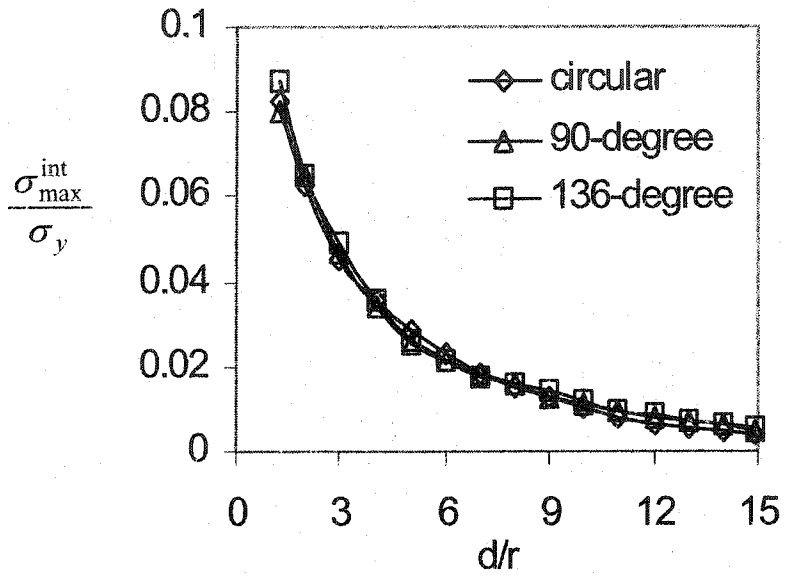


(a)

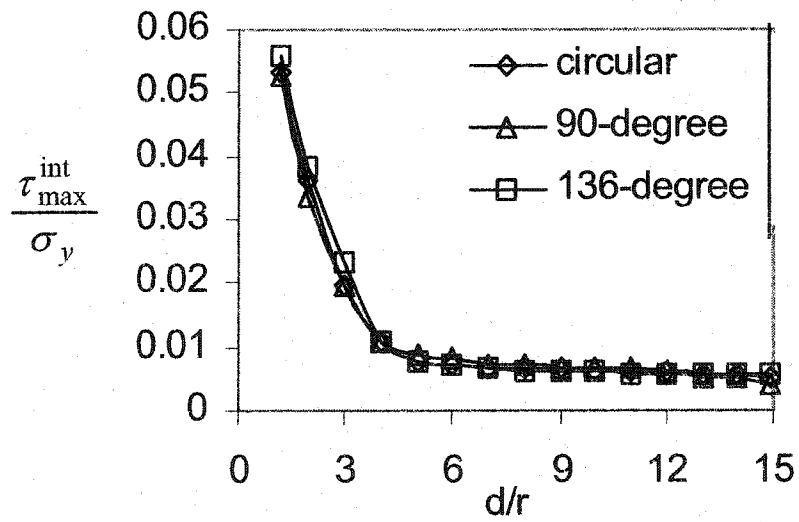


(b)

Fig. 4-6 The influence of indenter geometry and indentation position on the maximum (a) tensile stress and (b) shear stress for the steel-ceramic bond .



(a)



(b)

Fig. 4-7 The influences of indenter geometry and indentation position on the maximum (a) tensile stress and (b) shear stress for the tool steel-ceramic bond.

4.4. Conclusions

The influences of material properties and indentation parameters on interfacial stress were investigated using FEM, with the aim of establishing guidelines for effective application of a newly developed lateral force-sensing indentation method in evaluation of interfacial bond strength for coatings/films and composites. The following conclusions have been drawn:

- (1) At the free edge of interface, singularity existed for Al-ceramic and steel-ceramic bonds, which facilitated an interfacial debonding. There was no obvious singularity for the tool steel-ceramic bond.
- (2) Interfacial debonding resulted from interfacial tensile stress or shear stress or a combination of both. When the indentation distance from interface decreases, the maximum tensile and shear stresses increase. It is preferred to perform indentation test near the interface as close as possible.
- (3) Circular indenter may produce the largest interfacial tensile and shear stresses for soft-hard bonds; while the 136-degree indenter could produce the largest interfacial stresses for medium-hard bonds. For hard-hard bonds such as the tool steel-ceramic bond, the indenter geometry has no significant influence on the interfacial tensile and shear stresses.

Chapter 5

Application of the lateral force-sensing microindentation method for evaluation of the bond strength of thermal-sprayed coatings – A case study

In previous chapters, a novel lateral force-sensing microindentation method was introduced to evaluate interfacial bond strength for coatings/films and composites. The indentation test is performed on the sample cross section near an interface. By monitoring changes in lateral force during indentation, the critical indentation force corresponding to the interfacial debonding can be determined. The interfacial bond strength is then determined based on the critical indentation force and interfacial stress analysis using the finite element method. The mechanisms of interfacial debonding and lateral force response have been analyzed and the optimization of indentation condition have also been proposed. In this work, this novel method was applied to determine the interfacial bond strength of coatings, including a commercial thermal-sprayed $\text{Al}_2\text{O}_3/\text{TiO}_2$ coating (Mecto 130) and a nanostructured $\text{Al}_2\text{O}_3/\text{TiO}_2$ coating on mild carbon steel substrate. The main objective of this case study is to evaluate the efficiency of this method for interfacial characterization. The obtained results were compared to results of a pull-off test. It was demonstrated that the lateral force-sensing indentation method was effective for determination of interfacial bond strength.

5.1 Experimental Procedure

5.1.1. Preparation of coated samples

Two different $\text{Al}_2\text{O}_3/\text{TiO}_2$ composite coatings were produced on a carbon steel substrate: one was a commercial Metco 130 coating and the other was a nanostructured coating. Both of them had the same composition, consisting of 87wt% Al_2O_3 and 13% TiO_2 . The commercial Metco 130 coating was formed using a routine thermal spray process [127].

The nanostructured coating was processed in a different way. Nanosized Al₂O₃ and TiO₂ powders having mean particle diameters of 50 and 70 nm, respectively, were used to make the nanostructured coating. These powders were mixed with a fixed ratio to have the composition of the nanostructured coating the same as that of the Metco coating. The slurry containing this powder mixture was then sprayed and dried to form micrometer-sized granules (20-100µm). The obtained granules were subsequently heat treated to burn out the binder, an important component of the slurry.

The thermal-sprayed coatings were made using a Metco 9MB plasma gun. The spray condition was given in Table 5-1.

Table 5-1 Summary of plasma spray parameters [Ref. 128]

Parameters	Range
Current (A)	400-600
Voltage (V)	60-75
Primary Ar gas Pressure (psi)	100
Secondary H ₂ gas pressure (psi)	55
Primary Ar gas flow rate (SCFH)	120-200
Powder carrier gas flow rate (SCFH)	40-80
Powder feed rate (lb/h)	0.2-6.0
Gun moving speed (mm/s)	500
Spray distance (inches)	3.5-4.5

The coatings (thickness:100 μm) were sprayed onto steel substrate plates, which were 3 mm thick. The coated steel was then sectioned to make rectangular samples. The cross-section of the samples were polished and the final surface roughness was about 0.05 μm .

5.1.2. Microindentation test

The microindentation experiments were performed using a Micro-Tribometer, made by the Center for Tribology (California, USA). A cone-shaped tungsten carbide indenter having a tip radius of 0.2 mm and tip angle of 30° was used. The indentation test was performed on the sample cross-section at steel side at a distance of 30~80 μm away from the interface, as shown in Fig. 5-1. During indentation, the load was increased linearly from zero to 30 N at a speed of 0.013 N/s, During the test, the normal load, lateral force and time were recorded. The indentation position was determined using an optical microscope. The critical load corresponding to interfacial debonding was determined by averaging at least five measurements.

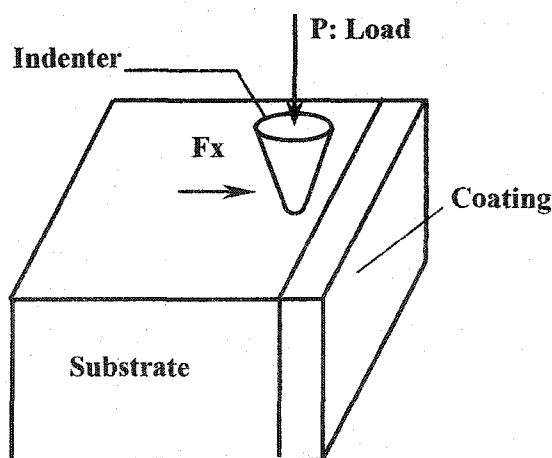


Fig. 5-1 Schematic illustration of the indentation test.

5.2. Results and discussion

5.2.1. Microstructures of the coatings

Typical microstructures of the commercial coating Metco 130 and the nanostructured $\text{Al}_2\text{O}_3/\text{TiO}_2$ are shown in Fig.5-2. The commercial coating shows a splat morphology, i.e. lamellae structure as illustrated in Fig.5-2(a). Such splat morphology is typically for thermal-sprayed coatings. In contrast, the nano-coating is composed of two distinct microstructural features. One is the fully melted (FM) splat structure similar to that found in the Metco 130 coating, and the other is a partially melted structure that has white particles embedded in a splat melted structure, as marked in Fig. 5-2(b). The partially melted (PM) structure has a typical liquid-phase sintered microstructure. TEM diffraction patterns indicate that the fully melted splat structure is mainly composed of $\gamma\text{-Al}_2\text{O}_3/\text{TiO}_2$, whereas the partially melted region consists of submicrometer-sized $\alpha\text{-Al}_2\text{O}_3/\text{TiO}_2$ particles (200nm to 3 μm) embedded in a $\gamma\text{-Al}_2\text{O}_3/\text{TiO}_2$ matrix [129].

Fig. 5-3. shows a representative SEM image of an interface between a fully-melted (FM) region and the steel substrate in the commercial coating Metco 130. Microcracks are observed at the interface, which are widely distributed in this commercial coating. In the case of the nanostructured coating, there are two types of interfaces: one between the FM region and the steel substrate, and the second between the PM region and the steel substrate. Fig. 5-4 shows representative SEM images of these two types of interface observed in the nanostructured coating. The interface between the FM region and the steel substrate contains many microcracks in the nanostructured coatings, similar to those observed in the Metco 130 coating (Fig 5-4 (a)). In contrast, the interface between the

PM region and the steel substrate is found to be highly bonded, as Fig. 5-4(b) illustrates. A schematic illustration of microstructures of these two coatings is shown in Fig. 5-5.

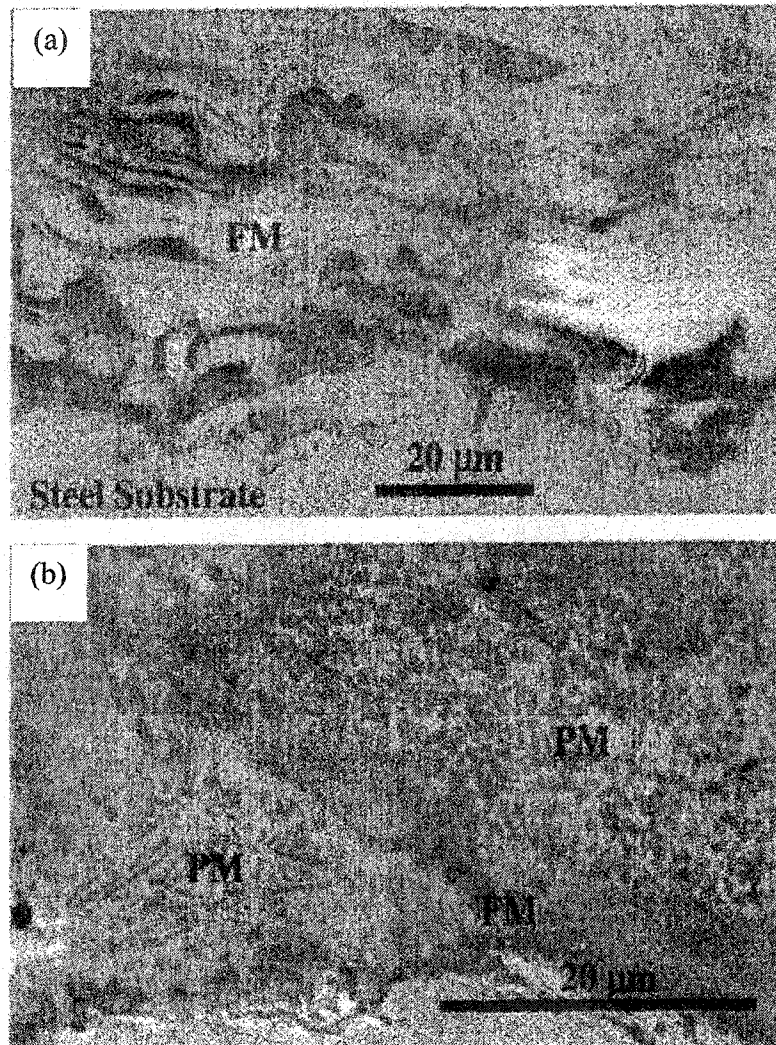


Fig.5-2 Cross-sectional SEM image of ceramic/metal interfacial regions in $\text{Al}_2\text{O}_3/\text{TiO}_2$ coatings on steel substrate: (a) Commercial coating Mecto 130, and (b) nonstructured coating. FM and PM represent fully-melted and partially-melted regions, respectively.

[Ref. 130]

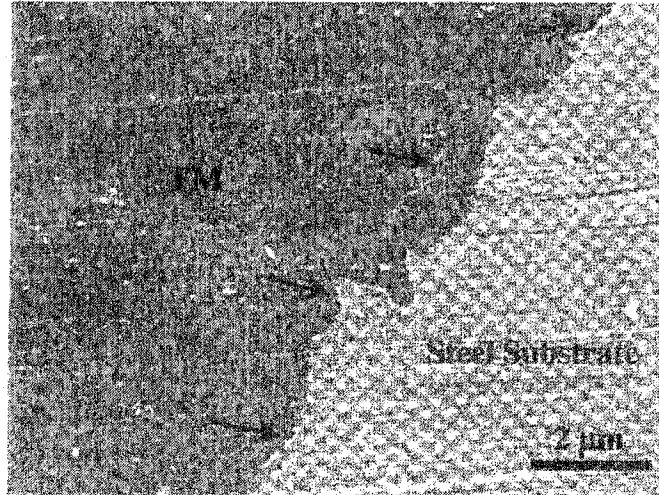
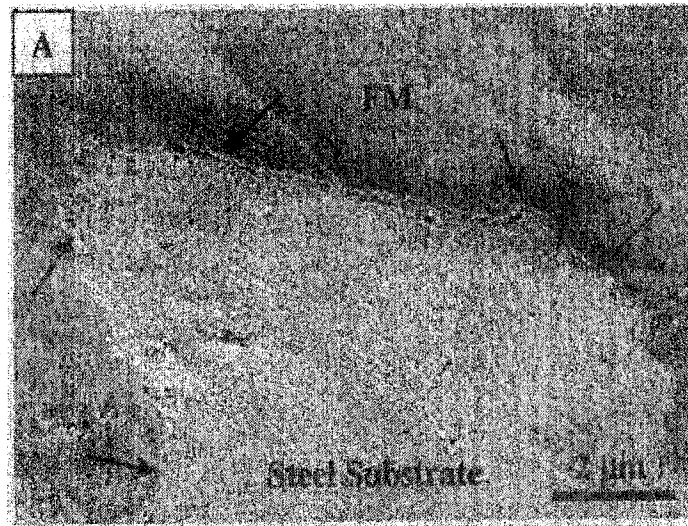
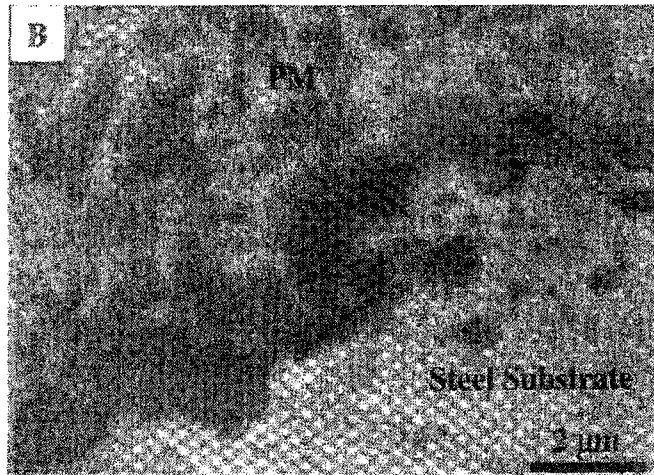


Fig. 5-3 A SEM image of the interface between a fully-melted (FM) region and the steel substrate in the commercial coating Metco 130. Cracks exist at the interface indicated by arrows [Ref 130].

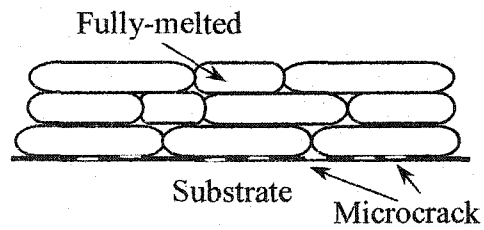


(a)

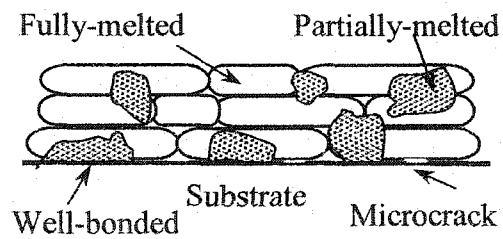


(b)

Fig. 5-4 SEM images of two interfaces in the nanostructured coating: (A) FM/steel interface and (B) PM/steel. Cracks exist at the FM/steel interface (indicated by arrows) but no cracks observed at the PM/steel interface [Ref. 130].



(a)



(b)

Fig. 5-5 Schematic illustration of coating's microstructures. (a) Metco130, and (b) nanocoating.

5.2.2. Determination of the interfacial bond strength

Interfacial bond strength of these two coatings were evaluated using the lateral force-sensing indentation technique. Typical normal load (L) ~ time curve and lateral force F_x ~ time curve are illustrated in Fig. 5-6. As shown, when the normal load was increased, the lateral force changed correspondingly. At the beginning of indentation, the absolute value of F_x increased gradually until the normal load reached a certain value, and then the absolute value of the lateral force decreased. Such a change corresponded to a change in slope sign of the F_x - t curve, indicating the occurrence of interfacial debonding as discussed earlier. A resultant interfacial crack is shown in Fig. 5-7.

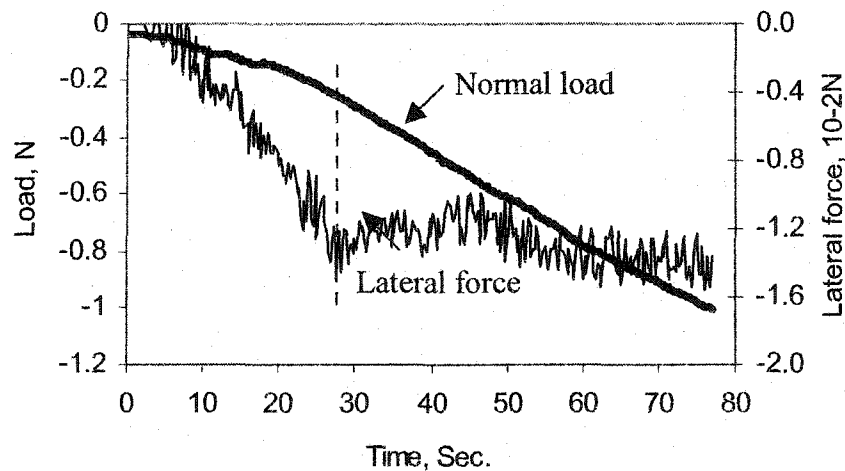


Fig. 5-6 Typical changes in the normal load and lateral force change vs. time for the nanostructured coating at distance of 40 μm from interface.

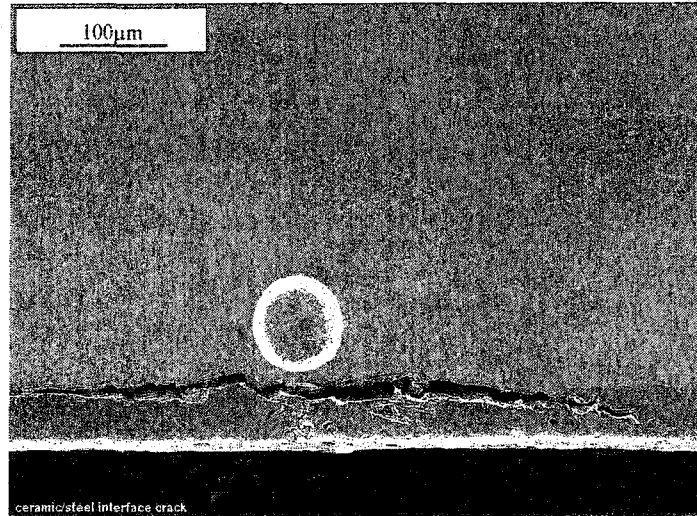


Fig. 5-7 Cracking at interface caused by indentation.

As mentioned earlier, the reason responsible for the occurrence of lateral force is the asymmetric constraint on the indenter. When the stress at interface was larger than the interfacial bond strength, debonding initiated at the interface. As a result, the asymmetric constraint changed and this resulted in a change in the sign of the lateral force curve slope. The corresponding normal load was the critical load (F_c) for interfacial debonding.

The critical loads corresponding to the interfacial debonding at different indentation positions for both Metco 130 and nanostructured coatings are shown in Fig. 5-8. One may see that when indentation was applied near the interface, a smaller critical load was required to cause interfacial debonding. Compared to the Metco 130 coating, the nano-coating needed a higher critical load to cause interfacial debonding at the similar indentation position. This means that the nano-coating had higher interfacial bond strength.

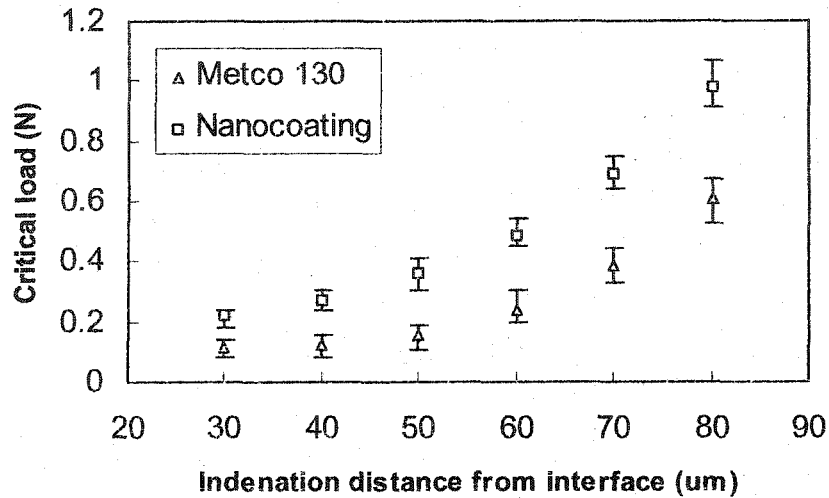


Fig. 5-8 The critical loads vs. indentation distance from interface for the coatings.

In order to determine the local interfacial stress distribution for calculating interfacial bond strength, a finite element model was employed with the measured critical load (F_c) as an input. The FEM analysis was made using ANSYS (version 7.0) software. All parameters used for the FEM analysis had the same values as those for the indentation experiment, such as the geometry and location of indenter and material properties.

The sample substrate was modeled using isotropic 8-node solid elements with elastic-plastic properties, while the ceramic coating was fully elastic. The mesh near indenter and interface was refined to adequately reflect the stress gradient with sufficient accuracy. The indenter was assumed to be a non-deformable body. Mechanical properties of the substrate and coatings are given in Table 5-2. The bottom boundary of a specimen was constrained in all directions. Load was applied on the indenter until the critical load was reached. Using this model, the stress distribution at the interface was calculated.

Table 5-2 Mechanical characteristics of involved materials

Materials	Young's Modulus	Poisson's ratio	Yield stress	Tangential Modulus
	E (GPa)	ν	σ_y (MPa)	Et (Gpa)
Carbon steel	200	0.25	540	10
Metco 130 coating	168.8	0.23	---	---
Nano-coating	158.2	0.23	---	---

Interfacial debonding generally occurs at the free edge of the interface, where the singularity could exist, as demonstrated in literature [131~133] and discussed in Chapter 4. This may make the calculated stress at a particular point in the vicinity of the free edge meaningless. Thus, an average stress approach was adopted here. The average of stress component σ_{ij} is defined as [134,135]:

$$\overline{\sigma_{ij}} = \frac{1}{x_{ave}} \int_0^{x_{ave}} \sigma_{ij} dx \quad (5.1)$$

where x_{ave} is a characteristic length along the interface, starting at the free edge, over which the integration is calculated. x_{ave} is treated here as a unknown parameter.

In order to determine the interfacial bond strength, a Quadratic Delamination Criterion [95] was adopted. This criterion takes account of both normal and shear stresses at the interface. The interfacial failure criterion between a coating and a substrate is given as

$$\left(\frac{\overline{\sigma_{xy}}}{Z}\right)^2 + \left(\frac{\overline{\sigma_{yx}}}{S}\right)^2 = 1 \quad (5.2)$$

where Z and S are the normal and shear interfacial bond strengths, respectively. $\overline{\sigma_{xy}}$ and $\overline{\sigma_{yx}}$ are respectively the average normal and shear stresses over the average length x_{ave} .

This criterion was used for the present calculation, the three unknowns, Z , S and x_{ave} need to be determined.

In order to determine Z , S and x_{ave} , at least three indentation tests are needed. In this work, we performed more than three tests at different positions for a particular coating to find corresponding three critical loads at interfacial debond. The following trial-and-error procedure was used to determine Z , S and x_{ave} [95]. For each given trial set (Z , S , x_{ave}), the predicted critical load could be obtained by finite element analysis. When Equation (5.2) is satisfied, the corresponding applied load is considered as the critical load, $Lc(i)$ ($i=1,2,\dots,n$), where i represents each indentation position. The predicted critical load ($Lc(i)$) is then compared to experimentally determined critical load ($Le(i)$) using a ratio $Q(i) = \frac{Lc(i)}{Le(i)}$. The coefficient of variation, CV , is defined as [136]

$$CV = \frac{\sqrt{\frac{1}{n-1} \sum (Q(i) - \bar{Q})^2}}{\bar{Q}} \quad (5.3)$$

where \bar{Q} is the mean value of $Q(i)$. The best-fit set (Z , S , x_{ave}) could be determined by giving a mean value $\bar{Q} = 1$ while maintaining the minimum CV . Using this approach, we

determined interfacial bond strengths for both the coatings, which are tabulated in Table 5-3.

Table 5-3. Interfacial bond strength determined using the lateral-force indentation method.

Material	Interfacial tensile strength (MPa)	Interfacial shear strength (MPa)	Xave. (mm)	Coefficient of variation (CV)
Metco 130 coating	26.2	11.23	0.121	5.66%
Nano-coating	44.01	29.45	0.120	3.94%

5.3 Comparison between results obtained using two different methods

The result of the lateral force measurement (Table 5-2) indicates that the nanostructured coating has higher tensile and shear interfacial bond strengths, 44.01 MPa and 29.45 MPa, than the commercial Metco 130 coating whose corresponding strengths are 26.2 MPa and 11.23MPa, respectively. The bond strength of the coatings was also measured using a modified ASTM direct-pull test [137], in which a coated sample was glued to another bulk material and tensile stress was applied to cause interfacial debonding. The maximum stress at interfacial debonding is the bond strength. The result of the pull-off test are given in Table 5-4 [137]. The results obtained using the pull-off test and the lateral-force indentation method are consistent. It is worth noting that the microindentation method yielded slightly higher values than those from the pull-off test. As a matter of fact, due to the difference in mechanical properties between the coating and the substrate, normal stress and shear stress coexist at the interface even under a

uniaxial tension load. Therefore, it is not accurate or adequate to quantitatively evaluate interfacial failure using a pure tension test. Since the multi-axial stress state at interface has been taken into account, the lateral force microindentation should provide more accurate information that is closer to reality.

Table 5-4. Pull-off test results [Ref.137]

Material	Interfacial ensile strength (MPa)	Coefficient of variation (CV)
Metco 130	16.65	5.17%
Nanocoating	39.30	3.95%

Another reason for higher interfacial bond determined using the microindentation method is that some defects such as voids or microcracks could be introduced to the interface during coating fabrication, sample cutting and preparation. These defects could act as the stress raisers, which facilitate interfacial delamination. Since the pull-off test only provides information on the overall performance of an interface, the stress concentration could result in interfacial failure under a smaller load than expected. For microindentation test, indentation is performed in local area and therefore it may reflect intrinsic interfacial bond strength, which should be higher than the average bond strength.

It was demonstrated that the nanostructured coating had a higher interfacial bond than the Metco 130 coating. The commercial Metco 130 coating was a typical plasma-sprayed

coating. Microcracks were observed at its interface [130]. In the case of the nanostructured coating, there existed two different interfacial zones, one was similar to that observed in the Metco 130 coating with microcracks, the other was a partially melted zone as illustrated in Fig. 5-2, which is believed to be highly adherent to the substrate[130]. However, investigation of the mechanism responsible for higher interfacial bond of the nanostructured coating is beyond the scope of the present study.

From the above discussion, one may draw a conclusion that the lateral force-sensing microindentation technique can provide information on the local interfacial bond strength, including both normal and shear strength components. This technique is therefore not only useful to evaluate of interfacial bond strength but also suitable for fundamental investigation of microstructural effects on interfacial strength. Since the indentation can be carried out on micro- and nano- levels, this technique would be effective for characterization and evaluation of a wide range of interfaces, including those in composites, coatings and thin films.

5.4 Conclusions

A newly developed lateral force-sensing microindentation technique was applied to evaluate interfacial bond strengths of regular and nanostructured $\text{Al}_2\text{O}_3/\text{TiO}_2$ coatings. The results of the test were compared to those obtained from a pull-off test. It was demonstrated that the results of these two types of test were consistent. However, the interfacial bond strengths determined using the microindentation technique were higher than those from the pull-off test. Such difference could be attributed to the fact that what

the microindentation test determined was closer to the intrinsic interfacial bond strength while the pull-off test only gave the average interfacial bond strength that was affected by interfacial defects such as microcracks. Furthermore, the later did not take account of possible effect of singularity of free edge where the influence of shear stress may exist, which could negatively affect the accuracy of the test. This study has also demonstrated that the lateral force-sensing microindentation technique is effective and feasible not only for evaluation of interfacial bond strength but also suitable for fundamental investigation of effects of interfacial defects on the interfacial strength for a variety of interfaces in composites, coatings and thin films.

Chapter 6 Summary and Future work

6.1 Summary of the research results

A new method was developed to evaluate the interfacial bond strength for coatings/films and composites, using a lateral force-sensing indentation approach. It has been demonstrated experimentally and theoretically that the lateral force is very sensitive to interfacial debonding. The mechanism responsible for the interfacial debonding caused by indentation was investigated using the finite element method. Effects of indentation parameters, including indenter geometry, indentation location and material properties, on interfacial stress distribution were investigated. Based on the FEM studies, the optimum indentation condition for evaluating the interfacial bond strength was identified. Finally, this method was applied to evaluate the interfacial bond strength of thermal sprayed $\text{Al}_2\text{O}_3/\text{TiO}_2$ coatings. From the above-mentioned studies, the following conclusions are drawn:

(1) It has been demonstrated that the lateral force on indenter is very sensitive to interfacial debonding when indentation is performed near the interface. When debonding occurs, the sign of the slope of the lateral force changes due to the loss of the asymmetrical constraint. The critical load for the initiation of interfacial debonding can be determined by monitoring changes in the sign of the slope of the lateral force~time curve. The stress distribution at the interface corresponding to this critical load can be calculated through FEM analysis. The interfacial stress is generally multiaxial, based on which the interfacial bond strength (Z^N , Z^S) can be determined using a so-called Quadratic Delamination Criterion (QDC).

(2) Finite element studies were conducted to investigate debonding of Cu-ceramic and Al-ceramic interfaces, two representative examples. For the Cu-ceramic bond, material sink-in occurred around the indenter. In this case, interfacial debonding was caused by a combination of tensile and shear stresses. For the Al-ceramic bond, pile-up occurred around the indenter and interfacial debonding was caused mainly by interfacial shear stress. However, when indentation was applied close to the interface, sink-in occurred around the indenter at the side near the interface. In this case, the interfacial debonding resulted from a combination of tensile and shear stresses.

(3) The effects of indentation parameters on lateral force response were investigated for the ceramic/Cu and ceramic/Al bonds, which corresponded to two different interfacial debonding mechanisms. The results indicated that the lateral force-sensing response to interfacial debonding had similar sensitivities for both the processes accompanied with “sink-in” and “pile-up”. The research further demonstrated that indentation was preferred to be performed close to an interface (without touching the interface), which could produce larger stress at interface and also larger change in the slope sign of the lateral force-time curve.

(4) Effects of indentation parameters, including indenter geometry, indentation location and material properties, on interfacial stress distribution were investigated. A finite element model-based optimization was achieved for three typical interfaces (Al-ceramic, steel-ceramic and tool steel-ceramic), which represented soft-hard, medium-hard and hard-hard interfaces, respectively. The results of the study demonstrated that a strong

singularity existed at the free edge of the Al-ceramic interface, while a weak singularity existed at the steel-ceramic interface. However, the free edge singularity was negligible for the tool steel-ceramic bond. The singularity could result in stress concentration and thus facilitate interfacial debonding. It was demonstrated that an indenter with circular geometry resulted in the largest interfacial stress for soft-hard bond, while an indenter with an angle of 136-degree between two opposite faces introduced the largest interfacial stress for medium-hard bond. For a hard-hard bond, the shape of tip did not significantly influence the interfacial stress.

(5) This method was applied to evaluate interfacial bond strengths of regular and nanostructured $\text{Al}_2\text{O}_3/\text{TiO}_2$ coatings, made by the thermal spray technique. The results of the test were compared to those obtained from a pull-off test. The interfacial bond strengths determined using the microindentation technique were higher than those from the pull off test. One reason was that what the microindentation test determined was closer to the intrinsic interfacial bond strength while the pull-off test only gave the average interfacial bond strength that was largely affected by interfacial defects such as microcracks. Furthermore, the pull-off test did not take account of possible effect of singularity at free edge where the influence of shear stress could exist, which negatively affected the accuracy of the test.

6.2 Possible future studies

The experimental and theoretical studies have demonstrated that the lateral force-sensing indentation is an effective method for evaluation of the interfacial bond strength. For

more efficient and wider application of this technique, follow-up studies would be necessary on the following two subjects.

(1) Theoretically, the lateral force-sensing technique is applicable to both coatings and composite materials. The present work has demonstrate successful application of this technique in evaluation of the interfacial bond strength of thermal-sprayed coatings. However, evaluation of interfacial bond strength for composites has not yet been carried out. Although the experimental test needed is the same as that for coatings, the calculation of interfacial stress may need a different finite element model for the composite. Since their interfaces may not be flat, for example, the interface in a particle-reinforced composite is curved, the interfacial stress analysis is therefore influenced by the particle shape and size as well as its position. Under these circumstances, the finite element model needs to be modified.

(2) Interfacial adherence is strongly affected by interfacial defects, impurity segregation and precipitates. Since the indentation can be performed on a small area under optical microscope or under atomic force microscope, this technique is therefore effective for determination of intrinsic interfacial bond. This allows us to investigate effects of interfacial imperfections and other factors such as precipitates and composition changes on the interfacial bond. Such studies are of importance to interfacial engineering, which is crucial to application of various coatings and multiphase materials.

Publications

H. Zhang and D.Y. Li, Application of a novel lateral force-sensing indentation method for evaluation of the bond strength of thermal sprayed coatings, **Surface and Coatings Technology**, accepted, 2004.

H. Zhang, Q. Chen and D.Y. Li, Development of a novel lateral force-sensing indentation technique for determination of interfacial bonding strength, **Acta Mater.**, 52 (2004), 2037-2046.

H. Zhang and D.Y. Li, Determination of interfacial bonding strength using bending test with *in situ* monitoring acoustic emission, **Surface and coating Technology**, 155(2002)190.

H. Zhang and D.Y. Li, Effects of sputtering condition on tribological properties of tungsten coatings, **Wear**, 255(2003) 924-932.

X. Y. Wang, H. Zhang, and D. Y. Li, Characterization of lubricated worn surfaces using a nano/micro-indenter, **Mater. Sci. & Eng. A**, 371(2004)222-228.

References

1. R.Peddada, K.Sengupta, I.M. Robertson and H.K. Birnbaum, Structure and chemistry for the Ti/sapphire interface, Proceedings of an international workshop, Metal-Ceramic interfaces, California, USA, 16-18 Uan, p1989.
2. K.B.Guy and D.M. Jacobson, Joining to ceramic in electrical and electronic applications: constraints and criteria, Designing interfaces for technological applications: ceramic-ceramic, ceramic-metal ceramic, Edited by S.D. Peteves, 1989, Elsevier applied science, London and New York, p33.
3. M.N. Kallas, D.A. Koss, H.T. Hahn and J. R. Hellmann, Interfacial stress state present in a "thin-slice" fibre push-out test, Journal of Materials Science, 27(1992)3821-3828.
4. L. T. Drzal, M.J. Rich, P.F. Lloyd, Adhesion of graphite fibers to epoxy matrices. Part I. The role of fiber surface treatment. J. Adhesion, 16(1983)1-30.
5. D. Hull, An introduction to composite materials, Cambridge University Press, 1981.p36.
6. J.K.Kim and Y.W.Mai, Engineered interfaces in fiber-reinforced composites, Elsevier Science Ltd, 1998, p6.
7. R. Naslain, Fiber-matrix interphase and interfaces in ceramic matrix composites processes by CVI. Composite interfaces, 1(1993)253-286.
8. A.G. Evans and J. W. Hutchinson, The thermomechanical integrity of thin films and multilayers, Acta metall. Mater. 43(1995)2507-2530.

9. U. Gaur and B. Miller, Microbond method for determination for the shear strength of a fiber/resin interface: evaluation for experimental parameters. *Composites Sci. Technol.* 34 (1990)35-51.
10. J.S. Kim, Y.C. Shin, K.T. Lee, W.T. Kang, T.H. Kim, K.Y. Lee, Y.J. Park, J.W. Park, Prevention of adhesion failure of a W/TiN/Ti(Co) layer on SiO₂ thin film, *Thin Solid Film*, 352 (1999)128-132.
11. S.A. Meguid, X.D. Wang, Wave scattering from cracks and imperfectly bonded inhomogeneities in advanced materials, *Mechanics of Materials*, 31(1999)187-195.
12. ASTM D5179, Standard test method for measuring adhesion of organic coatings to plastic substrates by direct tensile testing. 1998.
13. T. Lux, Adhesion of copper on polyimide deposited by arc-enhanced deposition, *Surface and coatings technology*, 133-134(2000)425-429.
14. T.C. Chang, M.H. Hon, M.C. Wang, Intermetallic compounds formation and interfacial adhesion strength of Sn-9Zn-0.5 Ag solder alloy hot-dipped on Cu substrate. *Journal of Alloys and Compounds*, 352(2003)168-174.
15. S. Suzuki, Y. Hayashi, K. Suzuki, E. Ando, Measurement of the adhesion strength of metal oxide and metal nitride thin films sputtered onto glass by the direct pull-off method, *Journal of Adhesion Science and Technology*, 11(1997)1137-1147
16. D.W. Butler, C.T.H. Stoddart and P.R. Stuart, Some factors affecting the adhesion of thin metal films, *Aspects of Adhesion*, Vol. 6 pp.53-63, D.J. Alner, Editor, CRC Press, Cleveland, Ohio, 1971.

17. D.w. Butler, A simple film adhesion comparator, J. Phys. Sci. Instrum. 8(1970)979-980.
18. C. T.H. Stoddart, D.R. Clarke and C.J.Robbie, Thin film adhesion: Effect of glow discharge on substrate, J. Adhesion 2(1970)270-278.
19. Z. Liu, R.F. Gibson, G.M. Newaz, The use of a modified mixed mode bending test for characterization of mixed-mode fracture behavior of adhesively bonded metal joints, Journal of Adhesion, 78(2002)223-244.
20. K.L.Mittal, Adhesion measurement of thin films, Electrocomponent Science and Technology, 3(1976) 21-42.
21. H. Ollendorf, D. Schneider, T. Schwarz, G. Kirchhoff, A. Mucha, Surface coatings and technology, 84(1996) 458.
22. K.Matsuura, K. Ohsasa, N.Sueoka, and M.Kudoh, Nickel monoaluminide coating on ultralow-carbon steel b reactive sintering, Metallurgical and materials transactions A, 30A(1999)1605-1612.
23. M. Xie and K. Vistasp M, Peel test for characterization of polymer composite/concrete interface, Journal of Composite Materials. 32 (1998)1894-1913.
24. S.J. Pomfret, K.P.Plucknett, V.Normand, W.J.Frith, I.T.Norton, Interfacial adhesion of biopolymer gels measured using peel test, Mat. Res. Soc. Symp. 622(2000) ff7.3.1-ff7.3.6.

25. J.W. Choi and T.S. Oh, Peel strength and peel angle measured by the T-peel test on Cr/BPDA-PDA interfaces, *Journal of Adhesion Science and Technology*, 15(2001)139-152.
26. Y.Y. Lin, C.Y. Hui, Y.C. Wang, Modeling the failure of an adhesive layer in a peel test, *Journal of Polymer Science, Part B: Polymer physics*, 40 (2002) 2277-2291
27. F.D. Hallworth, Bond testing of silver-plated engine bearings, *Automotive and Aviation Ind.* 95(2) (1946) 30.
28. J.W. Beams, Production and use of high centrifugal fields, *Science* 120(1954)619-625.
29. H. Alter and W. Soller, Ultracentrifugal measurement of the adhesion of epoxy polymer, *Ind. Eng. Chem.* 50(1958)922-927.
30. J.R. Huntsberger, Ultracentrifugal measurement of adhesion: some limitations, *Official Digest* 33(1961)635.
31. Correlation between mechanical properties of material and damage by the vibratory cavitation test, *JSME Int. J. Ser. 1*, 32(1989)558-566.
32. H. Ollendorf and D.Schneider, A comparative study of adhesion test methods for hard coatings, *Surface and Coatings Technology*, 113(1999)86-102.
33. F. Deuerler, M. Pohl, C. Hessian, Micro- and nanostructured diamond films under wear charging in cavitation test, *Surface and Coatings Technology*, 174-175(2003) 732-737

34. F. Deuerler, O. Lemmer, M. Frankm, M. Pohl, C.Hessing, Diamond films for wear prection of hardmetal tools, International Journal of Refractory Metals and Hard Materials, 20 (2002) 115-120.
35. M.L.Williams, The continuum interpretation for fracture and adhesion, J. Appl. Polymer Sci. 13(1969)29.
36. D.S. Campbell, Mechanical properties of thin films, Handbook of Thin Film Technology, L.I. Maissel and R. Glang, Editors, Chapter 12, McGraw Hill Book Company, N.Y., 1970.
37. P.J. Burnett, D.S. Rickerby, The scratch adhesion test: an elastic-plastic indentation analysis, Thin Solid Film, 157(1998)233-254,
38. P. Richard, J. Thomas, D. Landolt and G. Gremaud, Combination of scratch-test and acoustic microscopy imaging for the study of coating adhesion, Surface and Coatings Technology, 91(1997)83-90.
39. V. Juhani and U. Maekelae, Applications of the scratch test method for coating adhesion assessment, Wear, 115(1987)215-221.
40. J. Smolik, K.Zdunek, B. Larisch, Investigation of adhesion between component layers of a multi-layer coating $TiC/Ti(C_{sub x}, N_{sub 1 sub minus sub x})/TiN$ by the scratch-test method, Vacuum, 55(1999) 45-50.
41. J.Meneve, H.Ronkainen, etc., Scratch adhesion testing of coated surfaces- Challenges and new directions, Adhesion measurement of films and coatings, Vol. 2, pp 79-106, K.L. Mittal, Ed, 2001.

42. D.W. Butler, C.T.H. Stoddart and P.R. Stuart, Some factors affecting the adhesion of thin metal films, *Aspects of Adhesion*, Vol. 6 pp.53-63, D.J. Alner, Editor, CRC Press, Cleveland, Ohio, 1971.
43. R.D. Adams and J.A. Harris, Critical assessment of the block impact test for measuring the impact strength of adhesive bonds, *International Journal of Adhesion and Adhesives*, 16(1996)61-71.
44. D. Boehme and F. Bueltmann, *Technological Destructive Testing-Methods for the Determination of Bond Strength of Welded Hardsurfaces*, Pub. by Welding Inst, Abington, Engl, p 133-150.
45. Y. P. Wu, M. O. Alam, Y. C. Chan, B. Y. Wu, Impact properties of flip chip interconnection using anisotropically conductive film on the glass and flexible substrate, *Proceedings Electronic Components and Technology Conference*, 03CH3743, 8, 2003, p 544-548.
46. D.K. Shin and J.L. Lee, Fracture parameters of interfacial crack of bimaterial under the impact loading, *International Journal of Solids and Structures*, 38(2001) 5303-5322.
47. V.Gupta and A.S.Argon, Measurement of interface strength by laser-pulse-induced spallation, *Materials Science and Engineering*, A126(1990)105-117.
48. M. Zhou, Y.K. Zhang and L. Cai, Adhesion measurement of thin films by a modified laser spallation technique: Theoretical analysis and experimental investigation, *Applied Physics A, Materials Science and Processing*, 74 (2002) 475-480.

49. M. Boustie, E. Auroux and J.P. Romain, Application of the laser spallation technique to the measurement of the adhesion strength of tungsten carbide coatings on superalloy substrates, *EPJ Applied Physics*, 12(2000)47-53.
50. V. Gupta, V. Kireev, S.N. Basu, H. Wu, In-situ intrinsic interface strength measurement at elevated temperatures and its relationship to interfacial structure, *Interface Science*, 11(2003)359-368.
51. ASTM D 2344, Test method for apparent interlaminar shear strength of parallel fiber composites by short-beam method, 1989.
52. W.C. Cui and M.R. Wisnom, Contact finite element analysis of three- and four-point short beam bending of unidirectional composites, *Composites Sci. Technol.* 45(1992) 323-334.
53. C.E. Browning, F.>. Abrahams and J.M. Whitney, A four-point shear test for graphite/epoxy composites, *Composite Materials: Quality Assurance and Processing*, ASTM STP 797, ASTM, Philadelphia, PA. 1983, pp54-74.
54. F. Abali, A. Pora, K. Shivakumar, Modified short beam shear test for measurement of interlaminar shear strength of composites, *Journal of Composite Materials*, 37(2003) 453-464.
55. S.J.Bull, Can the scratch adhesion test ever be quantitative?, *Adhesion measurement of films & coatings*, Vol.2, 2001, 107
56. N. Iosipescu, New accurate procedure for single shear testing of metals. *J. Metal* 2(1967)537-566.
57. S. Lee and M. Munro, Evaluation of testing techniques for the Iosipescu shear test for advanced composite materials, *J. Composite Mater.* 21(1990)419-440.

58. D.F. Adams and D.E. Walrath, Iosipescu shear properties of SMC composite materials, *Composite Materials: Testing and Design*, ASTM STP787, ASTM, Philadelphia, PA. pp. 19-33.
59. M. Kumosa, G. Odegard, D. Armentrout, L. Kumosa, K. Searles, J.K. Sutter, Comparison of the plus or minus 45 degree tensile and iosipescu shear tests for woven fabric composite materials, *Journal of Composites Technology and Research*, 24(2002) p3.
60. ASTM D3518, Practice for in-plane shear strength of reinforced plastics.
61. D.F. Sims, In-plane shear stress-strain response of unidirectional composite materials, *J. Composite Mater.* 7(1973)124-128.
62. C.C.Chiao, R.L. Moore and T.T. Chiao, Measurement of shear properties of fiber composites, *Composites*, 8(1977)161-169.
63. D.F. Sims, In-plane shear stress-strain response of unidirectional composite materials, *J. Composite Mater.* 7(1973) 124-128.
64. R.D.Mooney, F.J. McGarry, Resin-glass bond study, 14th Annual Tech. Conf. Reinforced Plast. Composites Inst. SPI, 1965, Paper 12E.
65. L.J. Broutman, Measurement of the fiber-polymer matrix interfacial strength, *Interfaces in composites*, ASTM STP 452. ASTM. Philadelphia, PA, 1969, PP.27-41.
66. P.J.H. Franco and L.T. Drzal, Comparison of methods for the measurement of fiber/matrix adhesion in composites, *Composites*, 23(1992)2-27.

67. J. Singletary, H. Davis, M.K. Ramasubramanian, M. Toney, Transverse compression of PPTA fibers. Part I. Single fiber transverse compression testing, *Journal of Materials, Science*, 35(2000) 573-581.
68. L.J. Broutman, Measurement of the fiber-polymer matrix interfacial strength, *Interfaces in composites*, ASTM STP 452, 1969.
69. J.M. Yang, S.M. Jeng and C.J. Yang, Fracture mechanisms of fiber reinforced titanium alloy matrix composites. Part I. Interfacial behavior, *Mater.Sci.Eng. A138*(1991)155-167.
70. I. Roman and R. Aharonov, Mechanical interrogation of interfaces in monofilament model composites of continuous SiC fiber-aluminum matrix, *Acta Metall, Mater*, 40(1992) 477-485.
71. A. Kelly and W.R. Tyson, Tensile properties of fiber-reinforced metals: Copper/tungsten and copper/molybdenum. *J. Mech. Phys. Solids*, 13(1965)329-350.
72. A. Manor and R.B. Clough, In-situ determination fo fiber strength and segment length in composites by means of acoustic emission, *composites Sci. Technol.* 45(1992) 73-81.
73. A. Kelly and W.R. Tyson, Tensile properties of fiber-reinforced metals: copper/tungsten and copper/molybdenum, *J. Mech. Phys. Solids* 13, 329-350.
74. M.Barsoum and I.C. Tung, Effect of oxidation on single fiber interfacial shear stresses in a SiC-borosilicate glass system. *J.Am. Ceram. Soc.* 74(1991)2693-2696.

75. E.P. Butler, E.R.Fuller and H.M. Chan, Interface properties for ceramic composites from a single-fiber pull-out test. *Mat. Res. Soc. Symp. Proc.*, 170(1990),MRS. Pittsburgh, PA. pp.17-24.
76. C.W. Griffin, S.Y. Limaye and D.W. Richerson, Evaluatio of interfacial properties in borosilicate SiC composites using pull-out tests, *Ceram. Eng. Sci. Proc.* 9(1988)671-678.
77. A.N. Gent and S.Y. Kaang, Pull-out and push-out tests for rubber-to-metal adhesion, *Rubber Chem. Technol.* 62(1989)757-766.
78. B. Miller, U. Gaur and D.E. Hirt, Measurement of mechanical aspects of the microdebond pull-out technique for obtaining fiber/resin interfacial shear strength, *Composites Sci. Technol.* 42(1991)207-219.
79. M.V.Swain and J. Menčik, Mechanical property characterization of thin films using spherical tipped indenters, *Thin solid films*, 253(1994)204-211.
80. Y. Xie and H.M. Hawthorne, Measuring the adhesion of sol-gel derived coatings to a ductile substrate by an indentation-based method, *Surface and Coatings Technology*, 172(2003)42-50.
81. D.Chicot, P.Démarécanx, J.Lesage, Apparent interface toughness of substrate and coating couples form indentation test, *Thin solid film*, 283(1996)151-157.
82. P.H. Demarecaus, D. Chicot, J. Lesage, Interface indentation test for the determination of adhesive properties of thermal sprayed coatings, *Journal of materials Science Letters*, 15(1996) 1377-1380.

83. M.Z.Yi, B.Y. Huang, Y.Dai J.W.He and H.J. Zhou, Mechanical analysis and numerical calculation of bonding strength measurement by interfacial indentation method, *Trans. Nonferrous Met. Soc. China* 8(1998)263-268.
84. W.J. Fan, R.SA. Varin and Z. Wronske, Roll-bonding of a laminate aluminum alloy/Ni₃Al-type alloy composite, *Z. Metallkd.* 85(1994)7.
85. J.F.Mandell, J.H.Chen and F.J.McGarry, A microdebonding test for in situ assessment of fiber/matrix bond strength in composite materials, *Int. J. Adhesion Adhesives.* 1(1980) 40-44.
86. D.H.Gande, J.F.Mandell and K.C.C.Hong, Fiber-matrix bond strength studies of glass and metal matrix composites, *J. Mater. Sci.* 23(1988)311-328.
87. E.J.H. Chen and R.B. Croman, Microdebonding investigation on the effects of thermal residual stress on the bond strength of a graphite/polyimide composites, *Composites Sci. Technol.* 48(1993)173-179.
88. M. Desaegeer and I. Verpoest, On the use of the microindentation test technique to measure the interfacial shear strength of fiber reinforced polymer composites, *Composites Sci. Technol.* 48(1993)215-226.
89. J. Bystrzycki, J.Paszula, R.trebindski, R.A. Varin, The microstructure and interface behavior of Ni/NiAl composites produced by the explosive compaction of powders, *Journal of Materials Science*, 29(1994) 6221-6226.
90. D.Y.Li, K.Elalem, M.J.Anderson and S. Chiovelli, A microscale dynamical model for wear simulation, *Wear*, 225(1999) 380-386.
91. Q. Chen, Computer simulation of solid-particle erosion and related phenomena using a micro-scale dynamic model, M.Sc. Thesis, 2003, University of Alberta.

92. D.J. Strange, A.K. Varshneya, Finite element simulation of microindentation on aluminum, *Journal of Materials Science* 36(2001) 9143-1949.
93. Abdul-Baqi, E. Van der Giessen, Indentation-induced interface delamination of a strong film on a ductile substrate, *Thin Solid Films* 381(2001) 143-154.
94. C.H. Hsueh. Interfacial debonding and fiber pull-out stresses of fiber-reinforced composites, *Materials Science and Engineering A123*, 1-11 (1990).
95. J.C. Brewer, P.A. Lagace, Quadratic stress criterion for initiation of delamination, *J. Comp. Mater.*, 22(1988)538-548.
96. I.Skrna-Jakl and F.G. Rammerstorfer, Numerical investigations of free edge effects in integrally stiffened layered composite panels, 25(1993) 129-137.
97. M. T. Fenske and A. J. Vizzini, The inclusion of in-plane stresses in delamination criteria, *Journal of composite materials*. 35(2001) 1325-1341.
98. L.Paul A, B.Narendra V, Efficient use of film adhesive interlayers to suppress delamination, *ASTM Special Technical Publication*, n 1120, Published by ASTM, Philadelphia, PA, USA. P.384-396.
99. X.Long, G.J. Cai, L.E. Svensson, Investigation of fracture and determination of fracture toughness of modified 9Cr-1Mo steel weld metals using AE technique. *Materials Science and Engineering*, A270(1999)260-266.
100. A.R.Akisanya, Interfacial cracking from the free-edge of a be-material strip, *Int. J. Solids Structures* 34(1997)1645-1665.
101. D.Munz and Y.Y.Yang, Stresses near the free edge of the interface in ceramic-to-metal joints. *Journal of the European ceramic Society*, 13(1994)453-460.

102. D.D. Robertson and S.Mall, Fiber-matrix interface effects upon transverse behavior in metal-matrix composites, *Journal of composites technology and Research*, 14(1992)3-11.
103. S.K.Mital, P.L.N. Murthy and C.cC. Chamis, Interfacial microfracture in high temperature metal matrix composites, *Journal of composite materials*, 27(1993)1678-1694.
104. M.N. Kallas, D.A.Koss, H.T.Hahn and J.R.Hellmann, Interfacial stress state present in a "thin-slice" fiber push-out test, *Journal of materials science*, 27(1992)5821~5826.
105. A.C. Fisher-Cripps, B.R.Lawn, A.Pajares, L. Wei, Stress analysis of elastic-plastic contact damage in ceramic coatings on metal substrates, *J.AM.Ceram.Soc.*, 79(1996)2619-2625.
106. V.T.Bechel and N.R. Sottos, The effect of residual stresses and sample preparation on progressive debonding during the fiber push-out test, *Composites science and technology* 58(1998)1741-1751.
107. P.Montmitonnet, M.L. Edlinger, E.Felder, Finite element analysis of elastoplastic indentation; Part II-application to hard coatings.
108. S.Mukherjee, C.R.Ananth and N.Chandra, Effects of residual stress on the interfacial fracture behavior of metal-matrix composites, *Composite science and technology*, 57(1997)1501-1521.
109. I.S. Jakl and F.G. Rammerstorfer, Numerical investigations of free edge effects in integrally stiffened layered composite panels, *Composite structures*, 25(1993)129-137.

- 110.A.Abdul-Baqi, E.V.Giessen, Indentation – induced interface delamination of a strong film on a ductile substrate, *Thin solid films*, 381(2001)143-154.
- 111.S.Sen, B.Aksakal and A.Ozel, A finite-element analysis of the indentation of an elastic-work hardening layered half-space by an elastic sphere, *Int.J.Mech.Sce.* 40(1998)1281-1293.
- 112.C.R.Ananth and N.Chandra, Elevated temperature interfacial behavior of MMCs: a computational study, *Composites, part A*27A(1996)805-811.
- 113.D.B.Gundel, S.G. Warriar and D.B.Miracle, The transverse tensile behavior of SiC-fiber/Ti-6Al-4V composites. 2. Stress distribution and interface failure, *Composites science and technology* 59(1999)1087-1096.
- 114.A.Sackfield, D.A. Hills, Some useful results in the classical Hertz contact problem, *J. Strain Anal. Eng. Des.* 18(1983)101-105.
- 115.J.H.Ahn and D. Kwon, Derivation fo plastic stress-strain relationship from ball indentations: examination of strain definition and pileup effect, *J.Mater.Res.,* 16(2001)3170-3178.
- 116.T.Y.Tsui, Indentation plastic displacement field: Part II. The case of hard films on soft substrates, *J.Mater.Res.* 14(1999)2204-2209.
- 117.Y. Huang, Z. Xue, H.Gao, W.D.Nix and Z.C.Xia, A study of microindentation hardness tests by mechanism-based strain gradient plasticity, *J. Mater.Res.,* 15(2000)1786-1796.
- 118.M. T. Fenske and A.J.Vizzini, The inclusion of in-plane stresses in delamination criteria, *Journal of composite materials*, 35(2001)1325-1341.

- 119.J.M.Whitney and C.E.Browning, Finite element analysis of interlaminar shear in fibrous composites *Journal of composite materials* 5(1971)273-276.
- 120.D.Munz and Y.Y.Yang, Stresses near the free edge of the interface in ceramic-to-metal joints, *Journal of the European ceramic society*, 13(1994) 453-460.
- 121.M.A.Sckuhr, A.Brueckner-Foit, D.Munz and Y.Y. Yang, Stress singularities at a joint formed by dissimilar elastic-plastic materials under mechanical loading, *International journal of fracture*, 77(1996)263-279.
- 122.R.R. Tillner, Nonlinear regression analysis for estimating low-temperature vapor pressures and enthalpies of vaporization applied to refrigerants, *International journal of Thermophysics*. 17 (1996)1365-1385.
- 123.H.F.Wang, X. Yang and H. Bangert, Two-dimensional finite element method simulation of Vickers indentation of hardness measurements on TiN-coated steel, *Thin Solid films*, 214(1992)68-73.
- 124.Z. Q. Qian and A.R.Akisanya, An investigation of the stress singularity near the free edge of scarf joints, *European journal of mechanics, A/Solids*, 18(1999)443-463.
- 125.M. T. Fenske and A.J.Vizzini, The inclusion of in-plane stresses in delamination criteria, *Journal of composite materials*, 35(2001)1325-1341.
- 126.J.M.Whitney and C.E.Browning, Finite element analysis of interlaminar shear in fibrous composites *Journal of composite materials* 5(1971)273-276.
- 127.Product Bulletins, issued by Metco.

- 128.L.L Shaw, D. Goberman, R. Ren, M. Gell, S. Jiang, Y. Wang, T. D. Xiao. P. R. Strutt, The dependency for microstructure and properties of nanostructured coatings on plasma spray conditions, *Surface and Technology* 130(2000) 1-8
- 129.H. Luo, D. Goberman, L. Shaw, M. Gell, Indentation fracture behavior of plasma-sprayed nanostructured $\text{Al}_2\text{O}_3 - 13\% \text{TiO}_2$ coatings, *Materials Science and Engineering A346*(2003)237-245.
- 130.P.Bansal, N.P.Padture, A.Vasiliev, Improved interfacial mechanical properties of Al_2O_3 -13wt% TiO_2 plasma-sprayed coatings derived from nanocrystalline powders, *Acta Materialia*, 51(2003)2959-2970.
- 131.D.Munz and Y.Y.Yang, Stresses near the free edge of the interface in ceramic-to-metal joints, *Journal for the European Ceramic Society*, 13(1994)453-460.
- 132.M.A.Sckuhr, A.Brueckner-foit, D.Munz and Y.Y.Yang, Stress singularities at a joint formed by dissimilar elastic-plastic materials under mechanical loading, *International Journal of Fracture* 77(1996)263-279.
- 133.A.R.Akisanya, Interfacial cracking from the free-edge of a long bi-material strip, *Int. J. Solids Structures*, 34(1997)1645-1665.
- 134.R.Y. Kim and S.R.Soni, Experimental and analytical studies on the onset of delamination in laminated composites, *Journal of Composite Materials*, 18(1984)70-80.
- 135.S.Yi, L.X.Shen, J.K.Kim and C.Y.Yue, A failure criterion for debonding between encapsulants and leadframes in plastic IC packages, *J.Adhesion Sci. Technol.*, 14(2000)93-105.

136. J.H. Gong and Y.Li, Relationship between the estimated Weibull modulus and the coefficient of variation of the measured strength for ceramics, *Journal of the American Ceramic Society*, 82(1999)449-452.
137. E.H. Jordan, M. Gell, Y.H. Sohn, D. Goberman, L. Shaw, S. Jiang, M. Wang, T.D. Xiao, Y. Wang, P. Strutt, Fabrication and evaluation of plasma sprayed nanostructured alumina-titana coatings with superior properties, *Materials Science and engineering A301*(2001)80-89.